UNIVERSITY OF CALIFORNIA
RIVERSIDE

Rapid and Ultrasensitive Detection of Extracellular Vesicle Using Enzyme-Mimicking Nanomaterials

A Dissertation submitted in partial satisfaction
of the requirements for the degree of

Doctor of Philosophy

in

Environmental Toxicology

by

Qiaoshi Jiang

December 2022

Dissertation Committee:
Dr. Wenwan Zhong, Chairperson
Dr. Joseph Genereux
Dr. Ying-Hsuan Lin

The Dissertation of Qiaoshi Jiang is approved:

Committee Chairperson

University of California, Riverside

Acknowledgements

It would not have been possible to complete this work without the help and support of those around me. To my advisor Dr. Wenwan Zhong, I express my deepest gratitude for your support throughout my graduate studies. Thank you for your guidance, patience, encouragement, knowledge, and your invaluable advice given throughout my scientific career. My guidance committee member Dr. Joseph Genereux and Dr. Ying-Hsuan Lin, for the guidance, advice, and valuable suggestions that helped shape this work.

I would also like to extend my gratitude to my collaborator Dr. Pingyun Feng, Yuchen Xiao and Anh. N. Hong for sharing knowledge, synthesizing material and for providing valuable feedback. Thank you to Zhong research group members and friends that I made during my time in the Ph.D. program.

Lastly, I am grateful for the support, encouragement, and understanding of my family. I could not have achieved this work without their spiritual and emotional support. I would like to thank the support from Dissertation Year Award of Environmental Toxicology Program and NSF I-Corps award from Office of Technology Partnerships, University of California, Riverside.

ABSTRACT OF THE DISSERTATION

Rapid and Ultrasensitive Detection of Extracellular Vesicle for Liquid Biopsies

by

Qiaoshi Jiang

Doctor of Philosophy, Graduate Program in Environmental Toxicology
University of California, Riverside, December 2022
Dr. Wenwan Zhong, Chairperson

Extracellular vesicles (EVs) are cell-derived membranous vesicles in nearly all biological fluids, including blood and urine. EVs carry a great number of cargos such as proteins, nucleic acids, and lipids. EVs from the parent cells could transfer their cargos to the recipient cells, serving as an important route for cell-cell communication. In particular, small EVs generated from the endolysosomal pathway (~50-200 nm) have attracted interest as a suitable biomarker for cancer diagnostics and treatment monitoring, because they carry valuable biological information, and have molecular components reflecting the physiological status of their cells of origin. However, due to their small size, high heterogeneity, and low abundance, analysis of cancer cell-derived EVs is challenging, and the current EV analysis techniques are suffered from the limited detection range and/or the requirement of labor-intensive extraction steps. This thesis focuses on developing different methods which are rapid, simple, and sensitive to overcome some of these challenges.

This research describes the development of three types of enzyme-mimicking nanomaterials to enable rapid and sensitive EV detection. Chapter II is about the design and employment of the CuS-enclosed microgels that exhibited the capability to catalyze

the decomposition of peroxide for chemiluminescence production. The microgels can be applied for rapid EV isolation and sensitive quantification. The work described in Chapter III centered on the bimetallic metal organic framework (MOF) of Fe/Co-MIL-88(NH_2) that showed high peroxidase-like activity and can work together with glucose oxidase (GOx) in the cascade enzymatic reactions to oxidize the peroxidase substrate with the input of glucose. An assay that applied the cascade reaction catalyzed by both the peroxidase-mimicking Fe/Co-MIL-88(NH_2) and the GOx for sensitive and visible EV detection was thus developed. In Chapter IV, the bimetallic MOF was further improved by substituting the ligand used in MOF construction to enhance material stability and accommodate chemiluminescence as the signaling method. The limit of detection for EV analysis was much reduced, with the dynamic range much expanded, compared to the previous design. All three methods reported in this dissertation offer great low limits of detection between 10 ~ 10^4 EV particles/mL. These limits are all lower those of ELISA and NTA (10^6 ~ 10^8 particles/mL), which are the gold standards for EV detection. The reported methods are also rapid, with the enzyme-mimicking nanomaterials assisting with EV extraction to eliminate the needs for extra sample processing prior to detection. The enzyme-mimicking sensing materials developed in my dissertation work are inexpensive to fabricate and simple to use, suitable for serving as the signal amplification tools in a point-of-care diagnostic device deployable in the field and operated by minimally-trained personnel.

Contents

List of Scheme

List of Figures

List of Tables

Chapter I. Introduction

1.1 Significance of Extracellular Vesicles to Disease Detection

Extracellular vesicles (EVs) are membrane-enclosed vesicles with sizes ranging from 50 to 200 nm; can be secreted by most cell types;[1, 2] and are found to be present in various body fluids such as blood, bile and serum.[3] They carry miscellaneous molecular cargos including proteins, metabolites, and nucleic acids inherited from the parent cells;[2] and can transfer them to recipient cells, serving as a new route for cell-to-cell communication.[3] (Figure1.1) It is also believed that, EVs can impact pathological developments associated with immune responses, viral pathogenicity, cancer progression, and cardiovascular or central nervous system–related diseases.[4-7] Besides, cells under pathological conditions could produce a large number of EVs loaded with unique cargoes reflecting disease development.[8, 9] Both their close association with disease development and easy accessibility in the circulation systems support the high potential of EVs as diagnostic and therapeutic markers. However, the abundance of the tumor-specific EVs in bio-fluids is very low, and their signals are buried within a large number of heterogeneous EVs from diverse sources, imposing great challenges to EV detection.

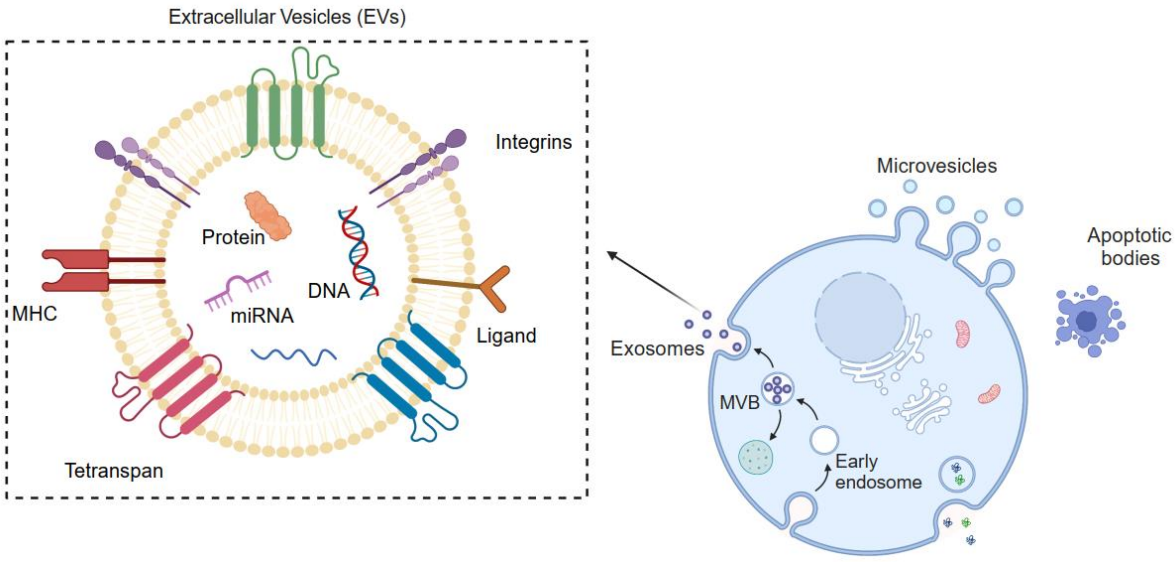

Figure 1.1 *Schematic of the different mechanisms for EV biogenesis. Inset: Schematic of the general molecular composition of an EV, created using BioRender.com.*

1.2 Current methods for EV analysis

Current many methods have been applied for EV analysis.(Figure 1.2) Nanoparticle-tracking analysis (NTA) is common method for EV analysis which measures the size distribution and particle concentration of clean EV samples.[10] Enzyme-linked immunosorbent assays (ELISAs) ,Western blots (WB) and flow cytometry (FCM) are the gold standards for detection of EVs through specific protein recognition.[11, 12] Quantitative PCR and next generation sequencing are applied for EVs nucleic acid analysis.[13, 14] But NTA , ELISA, WB, and qPCR all require EV purification and enrichment prior to detection, adding complexity to the detection assay.[15, 16] In addition, without prior EV isolation, ELISA and WB could not differentiate the free and EV-bound proteins, making protein concentration detected not truly representative to that of the EVs.[9] Conventional

isolation methods like ultracentrifugation consume large amounts of samples and yield low recovery.

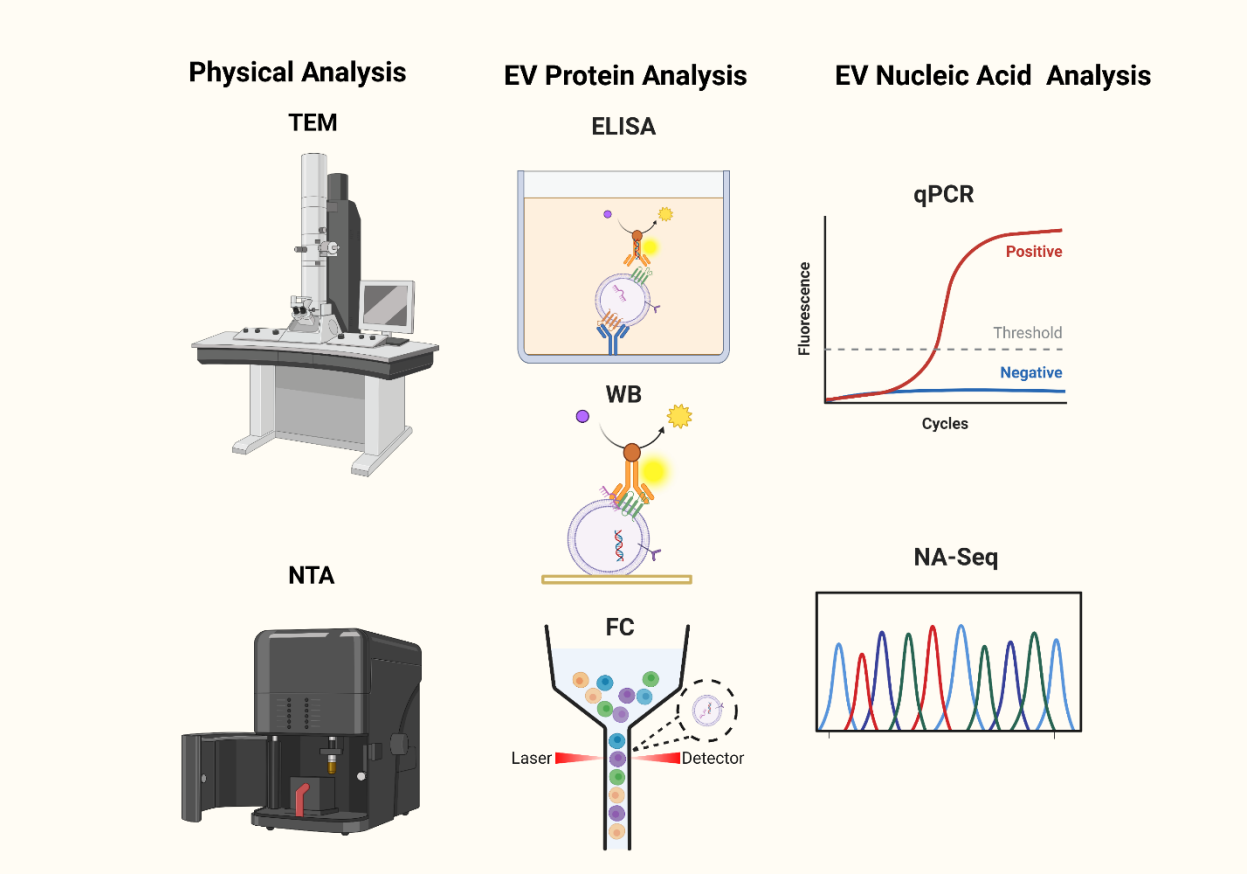

Figure 1.2 *Current methods for EV detection. Created using BioRender.com.*

Recently, some advanced approaches and devices have been developed for EVs detection. For example, Jongmin et al. recently developed A 96-well assay (termed HiMEX) that integrates the enrichment of EVs by antibody-coated magnetic beads and the electrochemical detection.[17] (Figure 1.3) A unique feature of HiMEX is the integration EVs isolation and detection into a single platform. This platform offers many practical

advantages including specific separation of EV without the need for extensive filtration or centrifugation and achieving a high detection sensitivity.

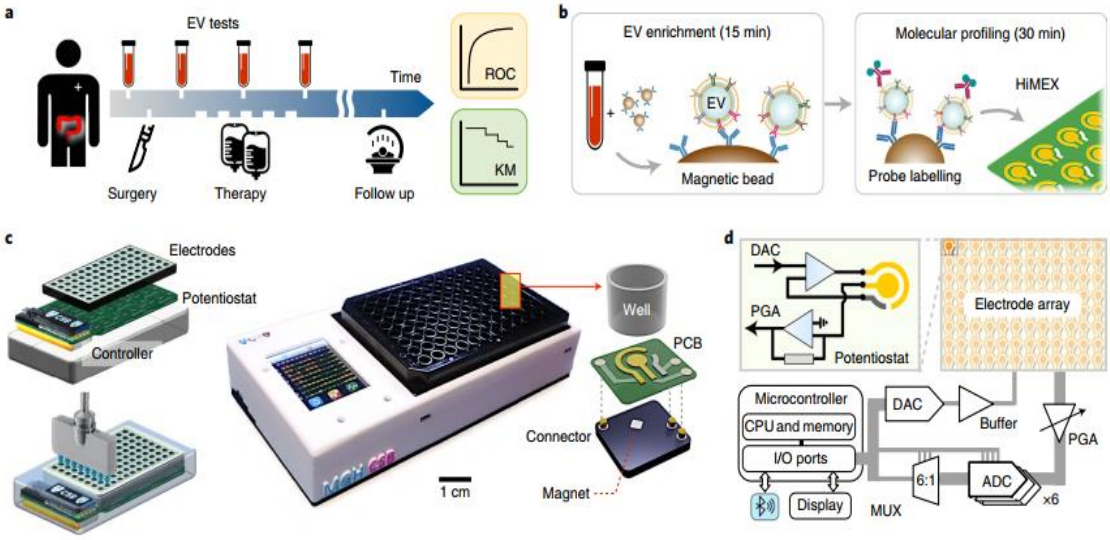

Figure 1.3 *HiMEX approach for clinical EV analyses. from ref.17 Copyright (2021) Nature Biomedical Engineering*

Other approaches have also been developed for EVs detection, such as DNA nanodevices,[10] electrochemistry,[18] microfluidics,[19] and surface enhanced Raman scattering.[20] State-of-the-art sensors built on microfluidic and nanofluidic devices have been developed to detect EVs down to 100 particles/mL.[21-27] These advancements have greatly enhanced researchers' capability to analyze EVs and identify the ones specifically related to pathological development. Still, simple but sensitive techniques for rapid EV detection are in demand to speed up the discovery and clinical applications of the EV-based disease markers.

1.3 Enzyme-Mimicking Nanomaterials

Various kinds of nanomaterials have been found show the enzyme mimicking activities, such as iron oxide, gold nanoparticles, nickel nanoparticles.[28](Figure1.4)

Enzyme-Mimicking Nanomaterials have the advantages of high catalytic activity, good stability, high tunability and, low cost.[29] Due to those advantages, enzyme-mimicking nanomaterials have been applied for biosensing, anti-bacteria and, cancer therapy purposes.[28, 30-32]

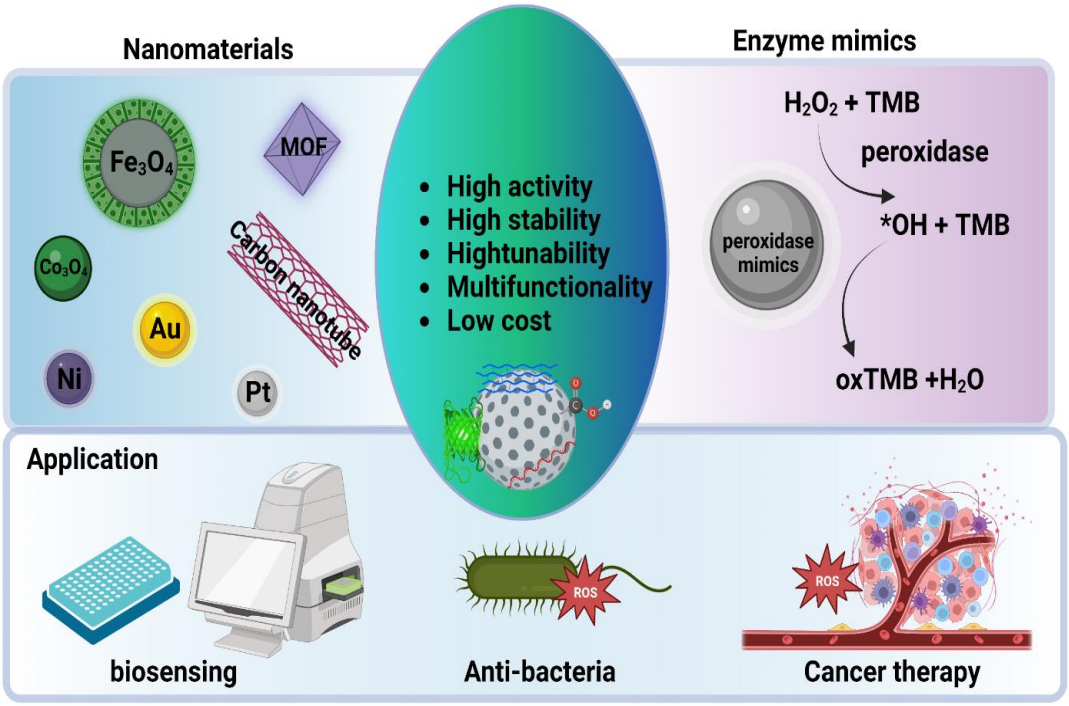

Figure 1.4 *Enzyme mimicking nanomaterial and their application. Created using BioRender.com.*

Enzyme-mimicking nanomaterials have been applied for immunoassays which greatly improved the sensitivity of the assays due to the superior enzyme mimicking activities. Zheng Xi et al applied peroxidase mimic−nickel−platinum nanoparticles as labeling tag for sandwich type Elisa detection of carcinoembryonic antigen.[33] (Figure 1.5 a) The sensitivity of nickel−platinum nanoparticles-based Elisa was 342-fold better than conventional HRP-based Elisa by 342-fold. Rui Chen et al developed Fe_3O_4@MOF@Pt and integrated it with

the dual-antibody sandwich lateral flow immunoassay (LFIA) platform. The platform can achieve an ultrasensitive immunochromatographic assay of procalcitonin with a sensitivity of 0.5 pg/mL, which is approximately 2280-fold higher than that of conventional AuNP-based LFIA and superior to previously published immunoassays.[34] (Figure 1.5 b)

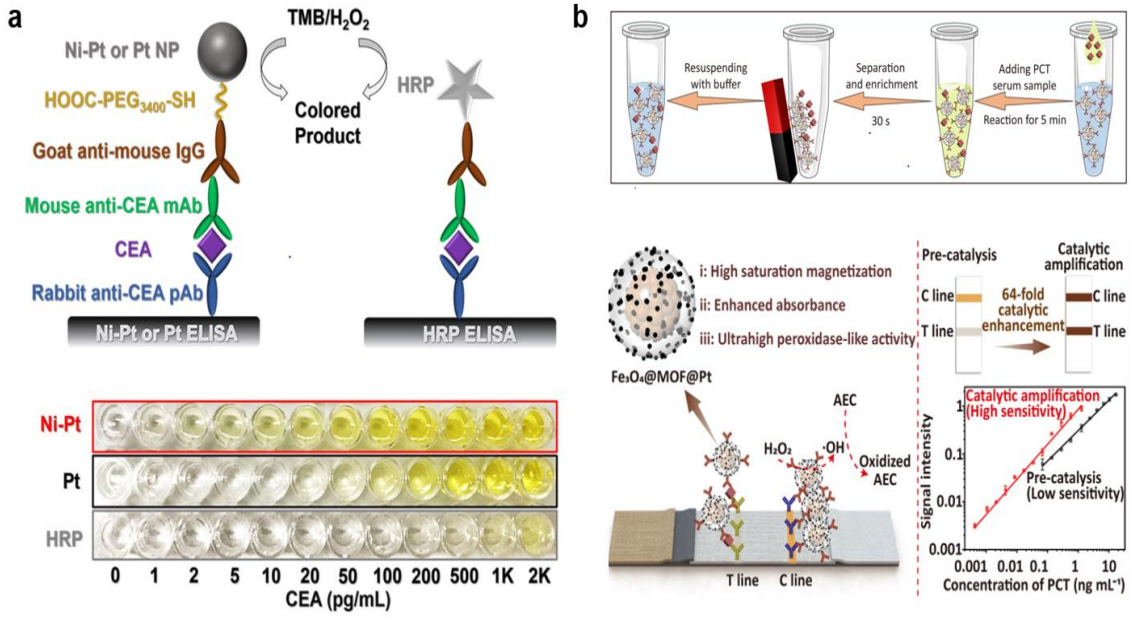

Figure 1.5 *Application of enzyme mimicking nanomaterial for biomarker detection. a) from ref.33 Copyright (2021) American Chemical Society b) from ref.34 Copyright (2022) American Chemical Society*

1.4 Objectives of This Dissertation

This research intends to develop simple and sensitive methods for rapid EV detection. In order to archive sensitive detection, a series of nanomaterial with superior peroxidase-like activity is designed. This nanomaterial not only function as catalysts for signal generation but also mediate the EV separation in our detection methods. Three main research objectives are detailed in Chapter II- IV. In chapter II, we aim to develop a CuS-enclosed microgels based assay that can enable rapid EV isolation and sensitive quantification in complex biological samples. Chapter III aims to develop bimetallic Fe/Co-MIL-88(NH_2) with high peroxidase-like activity that work together with glucose oxidase (GOx) in the cascade enzymatic reactions to oxidize the peroxidase substrate by inputting glucose. An assay applied the Fe/Co-MIL-88(NH_2) coupled glucose oxidase (GOx) cascade reaction is developed for sensitive and visible EV detection. Chapter IV aims to improve the sensitivity and detection range of the cascade reaction-based EV detection method in Chapter III by developing Fe/Co-TPY- MIL-88(NH_2) and using chemiluminescence as signaling strategy.

Reference

1. Théry, C., Zitvogel, L. & Amigorena, S. Exosomes: composition, biogenesis and function. *Nature reviews immunology* **2**, 569 (2002).

2. He, C., Zheng, S., Luo, Y. & Wang, B. Exosome theranostics: biology and translational medicine. *Theranostics* **8**, 237 (2018).

3. Nedaeinia, R. et al. Circulating exosomes and exosomal microRNAs as biomarkers in gastrointestinal cancer. *Cancer Gene Ther.* **24**, 48 (2017).

4. Atayde, V.D. et al. Leishmania exosomes and other virulence factors: Impact on innate immune response and macrophage functions. *Cellular immunology* **309**, 7-18 (2016).

5. Broekman, M.L. et al. Multidimensional communication in the microenvirons of glioblastoma. *Nature reviews. Neurology* **14**, 482-495 (2018).

6. Guo, Y. et al. Effects of exosomes on pre-metastatic niche formation in tumors. *Molecular cancer* **18**, 39 (2019).

7. Schorey, J.S., Cheng, Y., Singh, P.P. & Smith, V.L. Exosomes and other extracellular vesicles in host-pathogen interactions. *EMBO reports* **16**, 24-43 (2015).

8. Huang, T. & Deng, C.-X. Current progresses of exosomes as cancer diagnostic and prognostic biomarkers. *Int. J. Biol. Sci.* **15**, 1 (2019).

9. Vlassov, A.V., Magdaleno, S., Setterquist, R. & Conrad, R. Exosomes: current knowledge of their composition, biological functions, and diagnostic and therapeutic potentials. *Biochimica et Biophysica Acta (BBA)-General Subjects* **1820**, 940-948 (2012).

10. He, D. et al. Molecular-Recognition-Based DNA Nanodevices for Enhancing the Direct Visualization and Quantification of Single Vesicles of Tumor Exosomes in Plasma Microsamples. *Anal. Chem.* **91**, 2768-2775 (2019).

11. Li, A., Zhang, T., Zheng, M., Liu, Y. & Chen, Z. Exosomal proteins as potential markers of tumor diagnosis. *J. Hematol. Oncol.* **10**, 175 (2017).

12. Yu, S. et al. Tumor exosomes inhibit differentiation of bone marrow dendritic cells. *The Journal of Immunology* **178**, 6867-6875 (2007).

13. Buschmann, D. et al. Evaluation of serum extracellular vesicle isolation methods for profiling miRNAs by next-generation sequencing. *Journal of extracellular vesicles* **7**, 1481321 (2018).

14. Kloten, V. et al. Multicenter evaluation of circulating plasma microRNA extraction technologies for the development of clinically feasible reverse transcription quantitative PCR and next-generation sequencing analytical work flows. *Clinical Chemistry* **65**, 1132-1140 (2019).

15. Cheruvanky, A. et al. Rapid isolation of urinary exosomal biomarkers using a nanomembrane ultrafiltration concentrator. *American Journal of Physiology-Renal Physiology* **292**, F1657-F1661 (2007).

16. Zarovni, N. et al. Integrated isolation and quantitative analysis of exosome shuttled proteins and nucleic acids using immunocapture approaches. *Methods* **87**, 46-58 (2015).

17. Park, J. et al. A high-throughput magneto-electrochemical array for the integrated isolation and profiling of extracellular vesicles from plasma. *Nature biomedical engineering* **5**, 678 (2021).

18. Doldán, X., Fagúndez, P., Cayota, A., Laíz, J. & Tosar, J.P. Electrochemical sandwich immunosensor for determination of exosomes based on surface marker-mediated signal amplification. *Analytical chemistry* **88**, 10466-10473 (2016).

19. Xu, H., Liao, C., Zuo, P., Liu, Z. & Ye, B.-C. Magnetic-b
ased microfluidic device for on-chip isolation and detection of tumor-derived exosomes. *Anal. Chem.* **90**, 13451-13458 (2018).

20. Stremersch, S. et al. Identification of Individual Exosome-Like Vesicles by Surface Enhanced Raman Spectroscopy. *Small* **12**, 3292-3301 (2016).

21. Huang, G., Lin, G., Zhu, Y., Duand, W. & Jin, D. Emerging technologies for profiling extracellular vesicle heterogeneity. *Lab on a Chip* **20**, 2423 (2020).

22. Zhang, P., Zhou, X. & Zeng, Y. Multiplexed immunophenotyping of circulating exosomes on nano-engineered ExoProfile chip towards early diagnosis of cancer. *Chemical Science* **10**, 5495-5504 (2019).

23. Min, J. et al. Plasmon-Enhanced Biosensing for Multiplexed Profiling of Extracellular Vesicles. *Adv. Biosys.*, 2000003 (2020).

24. Wu, D. et al. Profiling surface proteins on individual exosomes using a proximity barcoding assay. *Nature Communications* **10**, 3854 (2019).

25. Zhang, P. et al. Molecular and functional extracellular vesicle analysis using nanopatterned microchips monitors tumor progression and metastasis. *Science Translational Medicine* **12**, eaaz2878 (2020).

26. Min, L. et al. Advanced Nanotechnologies for Extracellular Vesicle-Based Liquid Biopsy. **8**, 2102789 (2021).
27. Abreu, C.M., Costa-Silva, B., Reis, R.L., Kundu, S.C. & Caballero, D.J.L.o.a.C. Microfluidic platforms for extracellular vesicle isolation, analysis and therapy in cancer. **22**, 1093-1125 (2022).

28. Huang, Y., Ren, J. & Qu, X. Nanozymes: classification, catalytic mechanisms, activity regulation, and applications. *Chemical reviews* **119**, 4357-4412 (2019).

29. Wang, H., Wan, K. & Shi, X. Recent advances in nanozyme research. *Advanced materials* **31**, 1805368 (2019).

30. Nasir, M. et al. An overview on enzyme-mimicking nanomaterials for use in electrochemical and optical assays. *Microchimica Acta* **184**, 323-342 (2017).

31. Meng, X. et al. Nanozyme-strip for rapid and ultrasensitive nucleic acid detection of SARS-CoV-2. *Biosensors and Bioelectronics* **217**, 114739 (2022).

32. Thangudu, S. & Su, C.-H. Peroxidase mimetic nanozymes in cancer phototherapy: progress and perspectives. *Biomolecules* **11**, 1015 (2021).

33. Xi, Z. et al. Nickel–Platinum Nanoparticles as Peroxidase Mimics with a Record High Catalytic Efficiency. *Journal of the American Chemical Society* **143**, 2660-2664 (2021).

34. Chen, R. et al. "Three-in-One" Multifunctional Nanohybrids with Colorimetric Magnetic Catalytic Activities to Enhance Immunochromatographic Diagnosis. *ACS nano* **16**, 3351-3361 (2022).

Chapter II: Rapid Enrichment and Detection of Extracellular Vesicles Enabled by CuS-Enclosed Microgels

2.1 Introduction

Hydrogel microparticles (microgels) are stable, size-controllable materials with good biocompatibility that are simple to fabricate. The structural diversity and functionality of hydrogels can be improved by encapsulation of nanoparticles (NPs) made from noble metals, metal oxides, or transition-metal chalcogenides.[1] The multiple enclosed CuS nanoparticles enable signal amplification and thus contribute to ultrasensitive detection. Such ionic nanoparticle-modified microgels can be a new promising label material for ultrasensitive detection.

Reported EV concentrations range from 10^4 to 10^{12} vesicles/mL in plasma,[2] but not all EVs are tumor-specific and suitable to be cancer markers in liquid biopsy. During early disease development, the number of pathological cells is low, and so is the concentration of the EVs originated from such cells, thus demanding highly sensitive methods for their detection. Other obstacles for EV analysis in biofluids are their small sizes and the presence of the interfering matrix components, both of which require EV enrichment and isolation prior to detection.

Herein, we report a method that combines the CuS-enclosed microgels and membrane filtration for highly sensitive EV quantification in complex media. The microgels are

designed to carry out dual functions in EV analysis: their large particle sizes facilitate in situ EV isolation, while the enclosed CuS enables ultrasensitive detection of the isolated EVs using chemiluminescence (CL). In this way, only proteins on the EVs but not those freely suspended in samples are detected at very low concentrations. Our method is effective for quantification of EVs in both biofluids and cell culture media, representing a beneficial tool for the discovery of EV-based biomarkers and for the study of EV functions in disease development.

2.2 Experimental Section

Materials. N-(4-Aminobutyl)-N-ethylisoluminal (ABEI), sodium sulfide nonahydrate (SDS), potassium persulfate (KPS), N, N'-Methylenebisacrylamide (bis), acrylic acid (AA), allylamine (ALA) and N-isopropylacrylamide (NIPAM) were purchased from Sigma Aldrich. The biotinylated mouse anti-human ErbB2/HER2, mouse anti-human CD63, and biotinylated mouse anti-human CD63 was obtained from R&D systems, Sino Biological, and BioLegend, respectively. Horseradish peroxidase (HRP)-conjugated secondary antibody was from Cell Signaling Technology; and the streptavidin-HRP-conjugate was attained from Invitrogen. All other chemicals, including 1-(3-dimethylaminopropyl)-3-ethylcarbodiimide hydrochloride (EDC), and N-hydroxysulfosuccinimide (Sulfo-NHS), were purchased from ThermoFisher Scientific.

Cell culture. Human breast cell lines MCF-10A, MDA-231 and SK-BR-3 were obtained from ATCC and cultured in the recommended media containing 1% penicillin streptomycin. MCF-10A cells were cultured in the Dulbecco's Modified Eagle Medium (DMEM)/Nutrient Mixture F-12 supplied with 5% horse serum, 0.1 µg/ml cholera toxin, 10 µg/ml insulin, 0.5 µg/ml hydrocortisone, and 20 ng/ml epidermal growth factor (EGF). MDA-231 and SK-BR-3 cells were cultured in DMEM supplied with 10% and 20% fetal bovine serum (FBS), respectively. All cell lines were maintained at 37 °C in a humidified 5% CO_2 incubator and routinely screened for Mycoplasa contamination.

EV preparation. EV harvest was carried out by a Sorvall™ ST 16 Centrifuge (Thermofisher Scientific) and an Optima XPN-80 ultracentrifuge (Beckman Coulter). The medium was replaced with the EV-depleted culture medium after the cells reached a

confluency of 75%. The cells were cultured for 24-48 hours in this medium, which was then centrifuged at 500 g for 15 min to sediment the cells, and another 20-min centrifugation at 15,000 g to remove the remaining cellular debris. Next, the medium was ultra-centrifuged at 110,000 g for 70 min to harvest the EVs released by the cells. The EV pellet was washed once and resuspended in the freshly prepared 1× DPBS. Particle concentration in the EV solution was measured by NTA with the NanoSight NS300 (Malvern Instruments). The EV prepared was used within three day.

Microgel fabrication and antibody conjugation. Fabrication of the hydrogel microparticles followed the procedure reported previously with some modification.[3] In a typical procedure, 0.152 g of NIPAM, 0.030 g bis, 0.0225 g SDS and 47.5 μL AA were first dissolved with 23.5 mL of DI water in a 50 mL three-neck round bottom flask and stirred for 30 minutes under nitrogen. Secondly, the solution was heated to 70 °C, and 0.02 g KPS in 1.5 mL of water were injected into the flask to initiate the reaction. The reaction solution became milky within 10 minutes. After 10 minutes of reaction, 50 μL of ALA was injected and the solution became yellowish. The reaction continued for 4 hours. The product was cleaned up by dialysis against DI water for 2 days with frequent water changing using a 12-14 kDa dialysis membrane tubing (SpectrumLab). The product was stored at room temperature for future use.

To encapsulate the CuS nanoparticles, the microgel stock was diluted with water to a final volume of 24 mL, in which the final concentration of the -COOH group was about 3 mM. $Cu(NO_3)_2$ was then added to a final concentration of 1.5 mM. The pH was adjusted to 5.6 with 1 M NaOH and the solution was stirred under room temperature for overnight.

The next day, the solution was dialyzed against water for 2 days to remove the unbound Cu^{2+}. After dialysis, Na_2S was added to the solution at a final concentration of 1.5 mM. The solution turned orange and the reaction continued for 1 hour before being dialyzed against water to remove the free sulfide. The final product solution was kept at 4 °C until use.

Streptavidin was conjugated to the CuS-enclosed microgel by EDC/Sulfo-NHS. In brief, 10 µl of EDC at 0.4 mg/mL, 10 µL of Sulfo-NHS at 1.1 mg/mL, and 20 µL of streptavidin at 1 mg/mL were added to 160 µL of the MES buffer (50 mM MES, 0.15M NaCl, pH=6); and the mixture reacted for 15 minutes at room temperature. Then, 20 µL of this mixture was added to 1 ml of the CuS-enclosed microgel solution (10^{12} particles/ml), mixed well and reacted for 2 hours at room temperature. Afterwards, the solution was centrifuged at 500 g for 30 minutes to pass through the Amicon Ultra centrifugal filter (Sartorius Stedim Biotech) and remove the free streptavidin. The streptavidin-conjugated CuS-enclosed microgels were collected on top of the filter.

Microgel characterization. Transmission electron microscopy (TEM) images were recorded on a JEOL JEM-2100 transmission electron microscope at an acceleration voltage of 200 kV. UV−vis absorption spectra were collected using a spectrophotometer (Cary-100, Agilent Technologies). X-ray photoelectron spectroscopy (XPS) was performed using a Kratos AXIS ULTRADLD XPS system equipped with an Al Kα monochromated X-ray source and a 165-mm mean radius electron energy hemispherical analyzer.

EVs quantification with CuS-enclosed microgel. EV detection started by incubating 100 µL of the streptavidin-labeled CuS-enclosed microgel with 0.8 µL of the biotinylated

antibody (5 μg/ml) for 1 hour. Then, 100 μL of the antibody-labeled microgel was added to 100 μL of the EV-containing sample and incubated for 4 hours with gentle agitation. Followed, the reaction mixture was applied to the 0.45-μm Corning™ Costar™ Spin-X™ centrifuge tube filter and centrifuged at 14,000 g for 2 min. The free microgel particles were washed away with 800 μL of 1×PBS. At last, 100 μL of 1 M HNO_3 was added to the membrane to dissolve the CuS nanoparticles enclosed in the microgel; and the released Cu^{2+} was collected in the filtrate by another 2-min centrifugation. The pH of the filtrate was adjusted to 11 by adding 1 M NaOH, to which 10 μL of ABEI and 50 μL of H_2O_2 were injected to generate chemiluminescence (CL). The CL signal was recorded continuously for 120s under the luminescence mode in a GloMax®-Multi+ Microplate Reader (w/ dual injectors, Promega).

EV quantification with ELISA. A 96-well plate was first incubated with the EV solution (50 μL per well) for 12 hours at 4 ℃. After washed with 1×PBS for three times, the plate was blocked at room temperature with 5% milk (100 μL per well) for 4 hours. After blocking, each well was washed twice with 1×PBS, before 100 μL of 0.5 μg/mL biotinylated anti-Human CD63 antibody in 1% BSA was added and incubated at room temperature for 2 hours. The free antibody was then removed by four washes with 1×PBS, before an aliquot (100 μL per well) of 1:20,000 dilution of the HRP-conjugated secondary antibody in 5% milk was added and incubated at room temperature for another hour. Then each well was washed twice with 1×PBS and incubated with the SuperSignal™ West Pico PLUS Chemiluminescent Substrate (ThermoFisher) for 15 minutes before CL measurement.

2.3 Results and Discussion

CuS-enclosed microgel (CuS-MG) for EV isolation and detection. If the EVs secreted from diseased cells are to be detected, highly sensitive methods are demanded because the numbers of target EVs could be very low during the early stage of disease development. In addition, EV enrichment and isolation from the matrix are often required prior to detection to remove the interfering matrix components. In the present work, we solve the difficulties in both EV isolation and detection by the hydrogel microparticles, i.e. microgels (MGs) that encapsulate numerous CuS nanoparticles, as illustrated in Scheme 2.1. The MGs are fabricated through copolymerization of AA, NIPAM and ALA.[4] Because of the high density of carboxyl groups in the polymer network originated from AA, each MG particle can encapsulate a large number of divalent ions like Zn^{2+} and Cu^{2+} in the form of sulfide nanoparticles (NPs) (Gray inset of Scheme 2.1).[4] The NPs possesses high stability in solutions, but can release the encapsulated cations upon stimulation for signaling purpose. Cu^{2+} has been reported to be able to catalyze strong emission from the traditional CL systems, such as luminol-H_2O_2 and ABEI-H_2O_2,[5] through the Fenton-like reaction process to produce the highly reactive species of OH•.[6] Compared to other optical detection methods relying on fluorescence and light absorption, a CL system properly assembled is usually more sensitive, as it requires no excitation light to give out high signal-to-background ratio and is not affected by auto-fluorescence from sample matrix.[7] Thus, each CuS-containing MG can illuminate strong CL through the large number of the encapsulated Cu^{2+} and is an ideal signaling label for EV detection.

Additionally, the size of the MGs can be controlled by adjusting the monomer composition. Therefore, MGs that they could freely pass through a wide-bore filter before EV binding (Process *b* in Scheme 2.1) can be easily fabricated. Since each EV particle carries multiple copies of the target protein and can act as a bridge to link several MG particles together, the present of target EV can then induce aggregation of the MG particles, causing the EV-bound MGs not passing through the filter (Process ***a*** in Scheme 2.1). Once the encapsulated Cu^{2+} are released from the MGs and catalyze CL emission, quantitative detection of EVs can be realized. Although filtration is one of the conventional approaches for EV isolation,[8] typically filters with ultrafine pores are used which have to be handled with specially designed assembly or with high pressure or strong vacuum.[9, 10] The high forces involved could be detrimental to EV structures and the specialized devices are not widely accessible. In contrast, our design induces aggregation of the signaling units of MGs in the presence of target EVs, and only the wide-bore filters that can be handled with a simple table-top centrifuge are required, greatly simplifying the procedure and the technical demand.

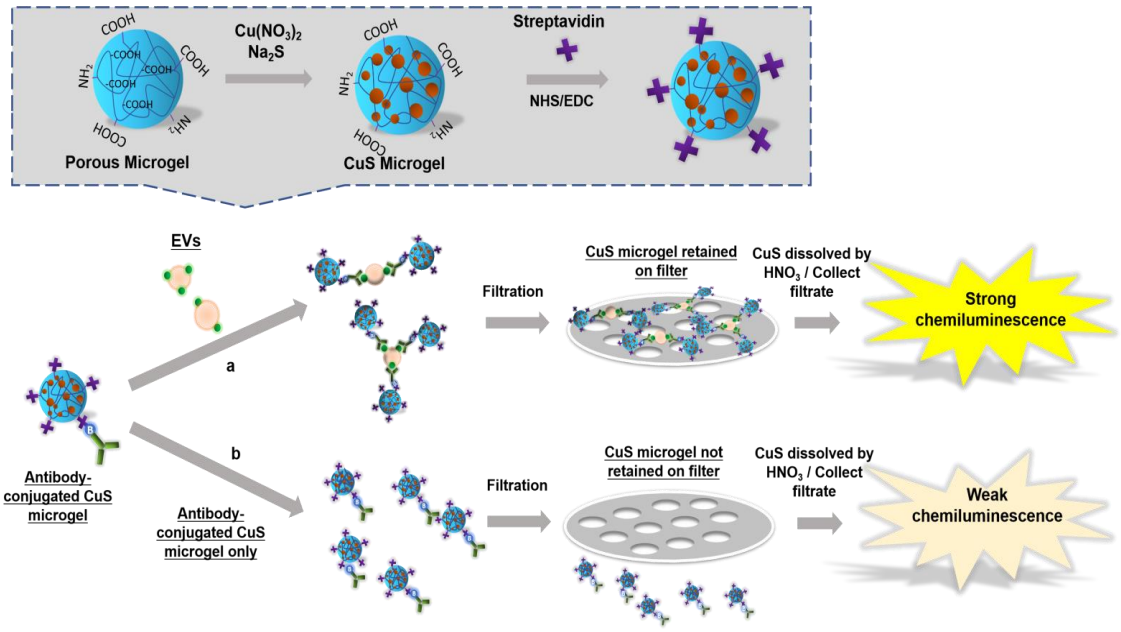

Scheme 2.1 *Schematic illustration of CuS-MG synthesis (upper gray panel) and the CuS-MG based assay for EV quantification (lower panel).*

MG preparation and characterization. The proper size of the MG is very important for the success of our design. The strong repulsion between the negatively charged carboxyl groups of AA typically produces MG larger than 500 nm in diameter. One way to reduce the size is to partially neutralization of the negative charges from the carboxyl groups. We added the crosslinker of ALA, a monomer carrying the positively charged amine group, for this purpose. We adjusted the concentration of ALA in MG synthesis and added it at various time points after the initiation of copolymerization between AA and NIPAM (Table S2.1). We learned from the results that, by keeping all other reaction conditions the same, adding ALA at 10 min instead of 1 hour after the initial polymerization reduced the size of MG from ~ 500 nm to ~ 300 nm, which was further reduced to ~ 100 nm by increasing the ALA amount by 4 folds. Increasing the mass of the crosslinker could form a more rigid gel network, limiting MG expansion and thus its size. Shortening the duration of the initial

polymerization step may have increased the proportion of ALA to be incorporated into polymer network, thus neutralizing more carboxyl groups, effectively suppressing gel expansion. With ALA added at only 10 minutes after the initial copolymerization, the amine groups from ALA may be closer to the surface of the MG for easy conjugation of the target-recognizing molecules like streptavidin and antibody.

Although ALA was added to partially neutralize the carboxyl groups, the MG carried negative surface potentials, which was measured to be around -20 mV, indicating that they contained more carboxyl than amine groups (Figure S2.1). The carboxyl groups are needed to encapsulate Cu^{2+} through strong coordination. CuS NPs were produced using the MG as the reaction vessel, with sequential addition of Cu^{2+} and S^{2-}. TEM images (Figure 2.1a&b) clearly showed that regardless of the size of the MG, ultrafine NPs were enclosed inside each of the gel particle. X-ray photoelectron spectroscopy (XPS) was conducted to confirm the presence of Cu in those particles by displaying the Cu 2p peaks at 932.7 eV and 952.3 eV (Figure 2.1c). The peak intensities obtained from the 500-nm MG were higher than the two smaller ones, indicating their higher Cu content per unit mass of the MG (Figure 2.1c). The 2p peaks for S were also found, although the signal-to-noise ratios of all three MGs were very low (Figure S2.1b). The Cu^{2+} content in each type of MG was quantified by ICP-AES (Figure 2.1d), and the results agreed with the observation shown in Figure 2.1d that larger the size of the MG, more Cu^{2+} were enclosed in each gel particle: while only $1.7 \pm 0.061 \times 10^{4}$ ($n = 3$) Cu^{2+} ion were enclosed in each of the 100-nm MG in average, this concentration increased to $6.4 \pm 0.031 \times 10^{5}$ ($n = 3$) in the 500-nm MG.

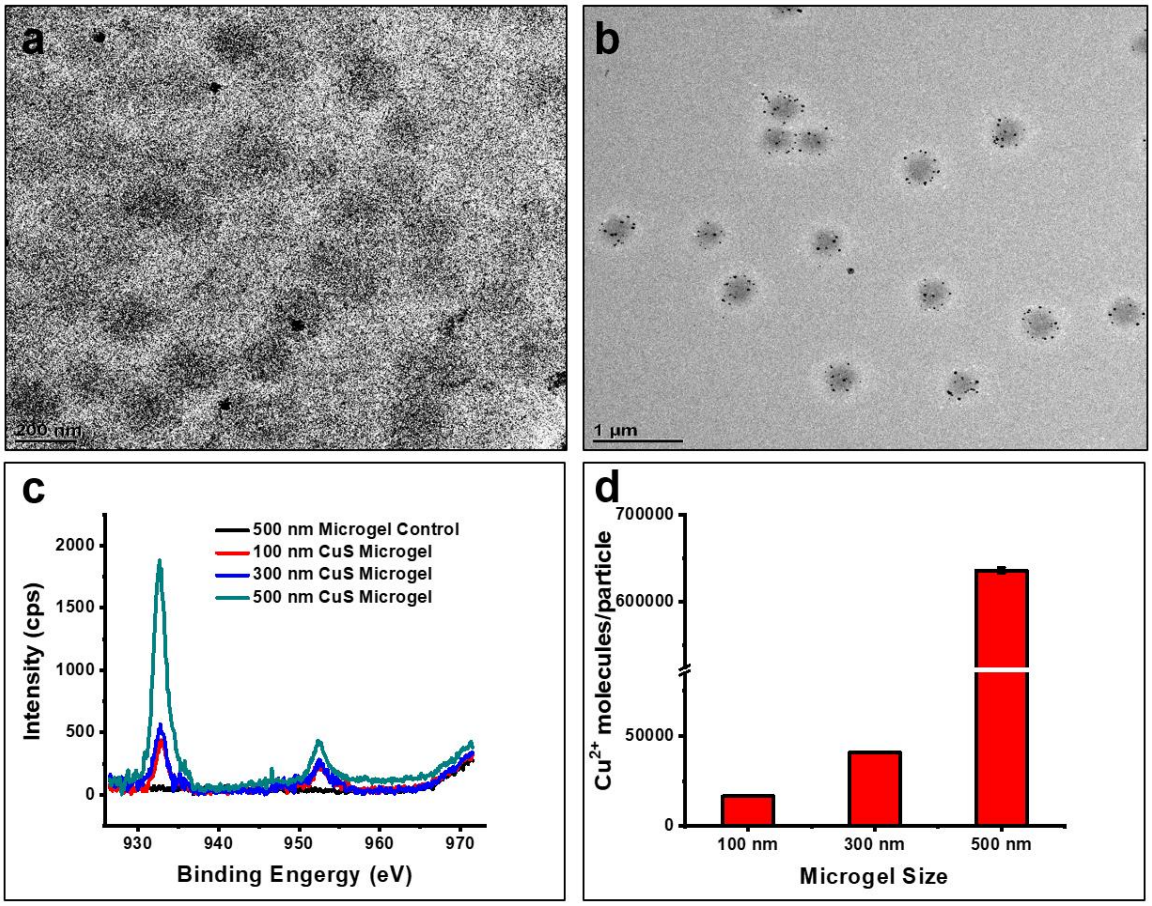

Figure 2.1 *Characterization of CuS-MG. TEM images of CuS-MG with an average diameter of a) 300 nm and b) 500 nm; c) XPS (Cu 2p) element analysis of CuS-MG; d) ICP-AES quantification of Cu2+ concentration in three CuS-MG.*

CL generation by CuS-enclosed MG (CuS-MG). By enclosing numerous CuS NPs inside each MG, CL emission can be directly catalyzed by the CuS NPs, owing to the high porosity of the hydrogel structure and the high surface activity of the ultrafine NPs. Alternatively, free Cu^{2+} ions can be released from the MG by acid digestion and act as catalyst. We compared the CL signals resulted from these two approaches using 8 pM – 435 pM of the 300-nm MG. As shown in Figure 2.2a, with the same amount of MG, the signal from the freed Cu^{2+} after acid digestion was at least two times higher than that from

the intact CuS-MG. Larger difference was observed higher MG concentrations. This is probably because the CuS NPs catalyzed the CL production only through Cu^{2+} on the NP surface, with Cu^{2+} inside the core of the NPs not participating in the reaction. In addition, both reactants including H_2O_2 and ABEI need to diffuse into the MG network to get close to the CuS NPs, which generates a barrier for the reaction. Both lead to lower CL signals from the intact CuS-MG. Thus, acid digestion was employed in the following work for CL production. The digestion was proved to be nearly complete within 15 minutes without damaging the membrane (Figure S2.2a).

We then evaluated the performance of CL generation by the 100-, 300-, and 500-nm MGs, against HRP, the gold standard enzyme used in immunoassays for CL production. Agreeing with their higher Cu contents than the smaller particles, the largest, the largest, 500-nm MG produced the strongest CL if the particle concentration was the same. Both the 300- and 500-nm outperformed HRP in catalyzing CL emission with 10 mM H_2O_2 and 0.5 mM ABEI: using the 300- and 500-nm MGs, a limit of detection (LOD) of 0.0038 and 0.1 pM was obtained, respectively, while that from HRP was only 0.1 nM (Figure 2b). The detection performance of the 100-nm MG was comparable to that of HRP due to the lower content of the enclosed Cu^{2+}. The curves plotting CL intensity vs. MG concentration all exhibited the hyperbolic shape, with slower increase in CL within the lower MG concentration range. Such a feature agrees with previous reports on using Cu^{2+}-based material for CL production;[11] and may be attributed to the two-step catalytic process of the Cu^{2+}-H_2O_2 system:[6, 12] firstly Cu^{2+} is reduced to Cu^{+} by H_2O_2, which is the rate-limiting step, and secondly Cu^{+} is cycled back to Cu^{2+} by H_2O_2-mediate oxidation, accompanied by

production of the highly reactive species, hydroxyl radical, responsible for strong CL emission. Thus, higher Cu^{2+} concentration significantly speeds up the rate-limiting step to attain a comparable rate as the second reaction step, causing more rapid increase in CL with unit increase in MG concentration.

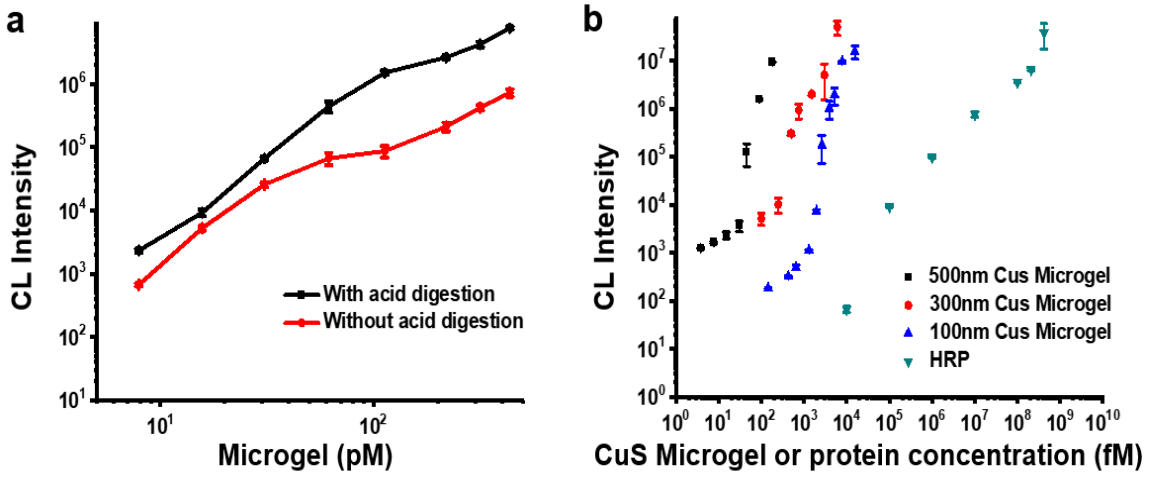

Figure 2.2 *Quantification of EV concentrations with the 300-nm CuS-MG in 1× PBS or Serum. Calibration curves in 1×PBS using a) anti-CD63; b) anti-HER2; and in serum using; c) anti-CD63 or d) anti-HER2. CL_0 = chemiluminescence without EVs. [ABEI] = 0.5 mM, [H_2O_2] =1 mM, pH=11.*

EV quantification with CuS-MG. In our design, the MGs should not be retained by the filter having a pore size larger than its particle diameter before bound to the target EVs. We compared the filter passing rates of the two MGs that generated the higher CL signals. More than 90% of the 300-nm MGs could pass through the 0.45-μm centrifugal filter by a 2-min gentle centrifugation with a bench-top microcentrifuge. This ratio was slightly higher than that of the 500-nm MGs (Figure S2.2b). The following assays thus all employed the 300-nm MG particles.

The 300-nm MGs were conjugated with streptavidin to anchor the biotinylated antibodies targeting various EV proteins, by activating streptavidin with EDC-sulfo-NHS

and linking it to the amine groups on the MG. Although the MGs also carried carboxyl groups, treating them with the activation reagents led to severe aggregations of MGs, reducing MG recovery after conjugation. Interestingly, lower concentrations of streptavidin used for conjugation led to more severe MG aggregation and lower MG recovery when using the 300k MWCO Spin filters to clean up the conjugated MG and remove the free streptavidin. Two μg/mL of streptavidin was the optimal concentration yielding the highest passing rate comparing with lower concentrations (Figure S2.2c).

The present work targeted the EVs carrying two specific surface proteins, CD63 and HER2. CD63 is a tetraspanin protein on EV surface and considered as a universal EV marker. HER2 is considered a cancer biomarker that have been found to be present on the EVs derived from certain tumor cells that carry over expression of HER2. The biotinylated anti-CD63 or anti-HER2 IgG were anchored to the streptavidin-conjugated MG particles, the resultant of which were then mixed with samples containing standard EVs at various concentrations in 1×PBS. The solution was filtrated to remove the unbound MGs, and acid digestion was conducted to release the Cu^{2+} ions from the MG particles retained on top of the filter after EV binding to catalyze CL emission from the luminol derivative of ABEI. Because a large concentration was covered, we used log scale for both axis. The plot showed a linear relationship for both surface markers within the EV concentration range of 10^4 to 10^8 particles/mL (Figure 2.3a&b). The LOD was calculated to be $8.27\pm0.20\times10^2$ EV particles/mL for CD63, and $3.43\pm0.04\times10^3$ EV particles/mL for HER2, based on the 3σ method.

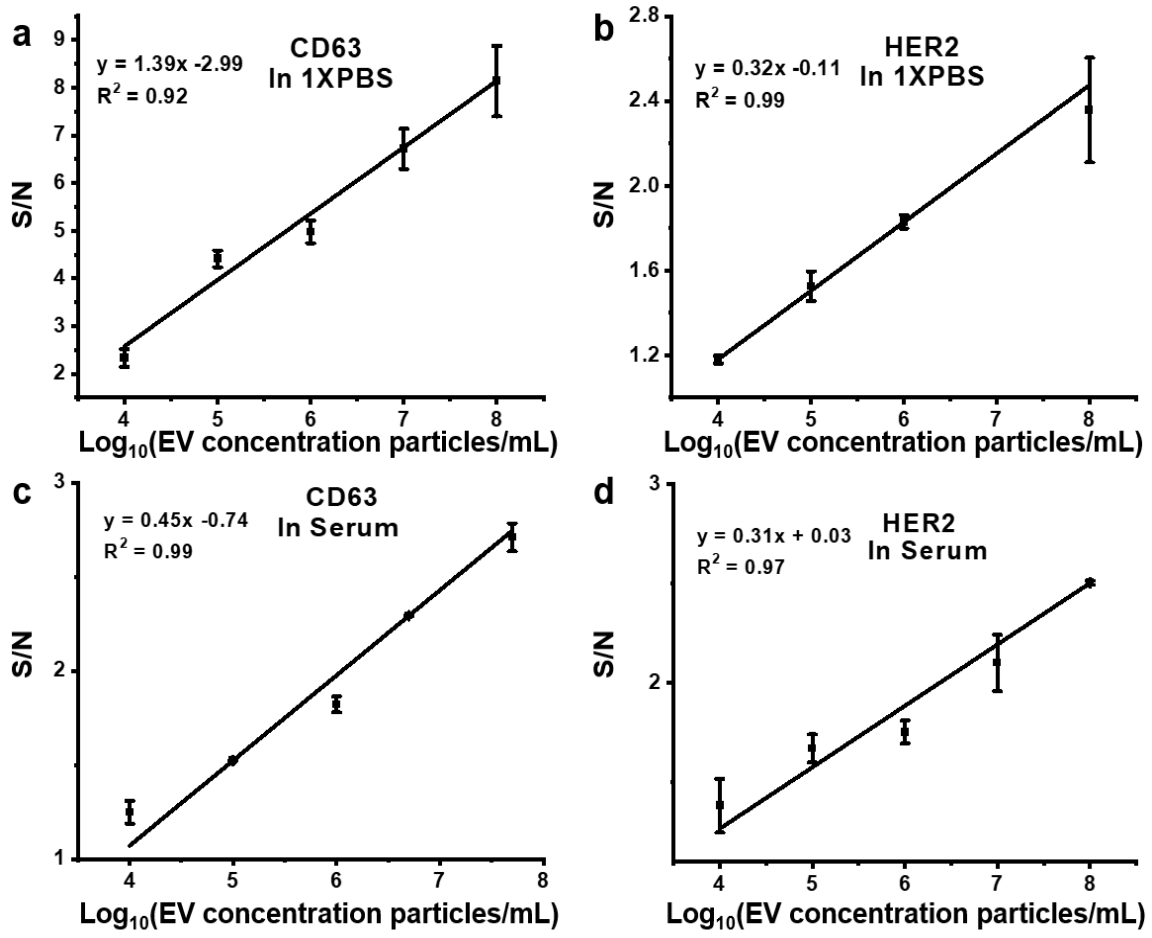

Figure 2.3 *Quantification of EV concentrations with the 300-nm CuS-MG in 1× PBS or Serum. Calibration curves in 1×PBS using a) anti-CD63, b) anti-HER2; and in serum using c) anti-CD63 or d) anti-HER2. CL_0 = chemiluminescence without EVs. [ABEI] = 0.5 mM, $[H_2O_2]$ =1 mM, pH=11.*

Detection of EVs in serum. The high sensitivity of our assay allows it to detect EVs in complex biological samples. We spiked the standard EVs into the 5× diluted EV-free serum; and 100 μL of the spiked serum was applied for our assay. Again, linear relationships between Log (CL) and Log (EV concentration) using either CD63 or HER2 as the target protein were observed (Figure 3c & d). The complex matrix of serum reduced the sensitivity for detection of the CD63-positive EVs by about 3 folds judged by the slope of the calibration curves (Figure 2.3a & c), but interestingly the slope did not change much

for detection of the HER2-positive EVs. This may be due to the difference of target recognition specificity between the two antibodies used: the anti-CD63 antibody may be less specific compared to the anti-HER2 antibody, and could bind to more interfering proteins in serum and be passivated more severely, reducing the total number of MGs available for EV capture. The LOD for CD63- and HER2-based EV detection increased by about 13 and 7 folds, respectively. Still, such an LOD is lower than what could be obtained by NTA (10^8 – 10^9 particles/mL) and ELISA (10^{10} particles/mL), as well as most of those reported in literature by far (Table S2.2)[13-25]. We also tested the recovery of EVs with our method by adding a known amount of the standard EVs to 100 µl of the EV-depleted serum. The percent recovery was calculated by dividing the detected EV concentration with the spiked concentration, and found to be between 96.9% and 99.7% with the various EV concentrations used (Table 2.1). The high EV recovery could be attributed to its high sensitivity as well as simple procedure with the prior-detection requirement of EV purification.

EV Spiked in Serum (Particles/mL)	Recovery Rate (%)
5×10^6	96.9 ± 3.4
2.5×10^6	97.5 ± 2.7
5×10^5	99.7 ± 2.0

Table 2.1 *Percent recovery of spiked EVs in serum samples. EV depleted serum was spiked with different number of EVs and measured by CuS-MG. The data is shown as mean ± %RSD (n=3).*

To briefly demonstrate the applicability of method in clinical testing, we applied it to evaluate the EV concentration in two clinical samples, one from a healthy individual and

the other from a patient with early-stage breast cancer. For each test, we only employed 1 μL of the raw serum sample, diluted it to 100 μL with 1×PBS, and mixed it with the antibody-conjugated MG solution. The CL signals were compared between these two samples (Figure S2.4). The result indicated that, the CL signal from the CD63-positive EV in the serum of the healthy individual was higher than that from the serum of the cancer patient; while the signal from the HER2-positive EVs showed an opposite trend. Since CD63 is considered as a general marker for EVs and HER2 for EVs derived from cancer cells with HER2 overexpression, the relative signal intensity observed by our method indicates that the serum of the cancer patient contained a higher proportion of the EVs carrying the tumor-specific HER2 protein than that of the healthy individual. Recently, numerous works analyzing the protein expression profiles on single EVs have reported the possibility of using the relative contents of EVs carrying different protein markers for disease diagnosis.[26-28] Compared to these single EV analysis techniques, our method provides a much simpler approach to evaluate the relative contents by targeting various EV proteins with comparable sensitivity, enabling examination in a large collection of clinical samples for validation of such hypothesis.

Detection of EVs in cell culture medium. Upon the discovery of the possible functions of EVs in cell-cell communication, cancer metastasis, cell reprogramming, etc., intense works have been devoted to study the biogenesis of EVs from different cells of origin, and how their secretion could be stimulated by external factors.[29, 30] EV secretion by diverse cell lines is being examined extensively. The low sensitivity of the conventional methods like ELISA and WB makes it difficult to monitor EV secretion in the cell culture

medium, which is often in mLs and contains low numbers of EVs if the number of cells are not adequate and the harvest duration is shorter than 24 hrs.[31] Ultracentrifugation or other tedious EV isolation methods are needed to enrich the EVs from the culture media into a much smaller volume for down-stream analysis. Because our method employs filtration to retain the EVs upon binding to the MG particles, and it is highly sensitive, it should be suitable for monitoring EV secretion from stimulated cells without EV pre-concentration nor consumption of a large number of cells.

To demonstrate this capability, we tested the EVs concentration in the culture media of three cell lines: the non-cancer cell line of MCF-10A, and the cancer cell lines of MDA-231 and SK-BR-3. It has been reported that both MCF-10A and MDA-231 have low HER2 expression and SK-BR-3 cells express a higher level of HER2 than the other two.[26, 32] Only 100 μL of the cell culture medium was subject for EV quantification by the CuS-MG conjugated to either the anti-CD63 or anti-HER2 antibodies. The CL signals obtained from the EVs collected from these three cell lines were compared in Figure 2.4a. We can see that, the CL intensities resulted from the anti-CD63 MG were comparable among the three cell lines, but those from the anti-HER2 MG were quite different, with that from the SK-BR-3 cells being the highest, agreeing with its higher HER2 expression level than the other cell lines.

We also employed ELISA to quantify CD63 in these samples, and found a very strong linear relationship with an R value of 0.99 and a significance value < 0.001 between the protein contents and the CL signal obtained by our method (Figure 2.4b), well supporting that the CL signal is proportional to the content of EV proteins secreted by the cells.

However, to obtain the ELISA result, a total of 45-75 mL culture medium which was needed to culture about 4×10^7 – 6×10^7 cells were ultracentrifuged to obtain the precipitated EVs prior to detection. Such a sample consumption is 450-750 times more than what was used in our method (Figure S2.4), which can enrich the EVs on top of the filter by the aid of the CuS-MG and provide high detection sensitivity to assess the EV content in a very small volume of the culture medium. In addition, our method ensures detection of proteins on EVs instead of the free proteins, because free proteins cannot serve as the bridges to link different MGs and induce MG aggregation: negligible signals from the MG particles were obtained with 0.19-19.23 fM of protein (Figure S2.5).

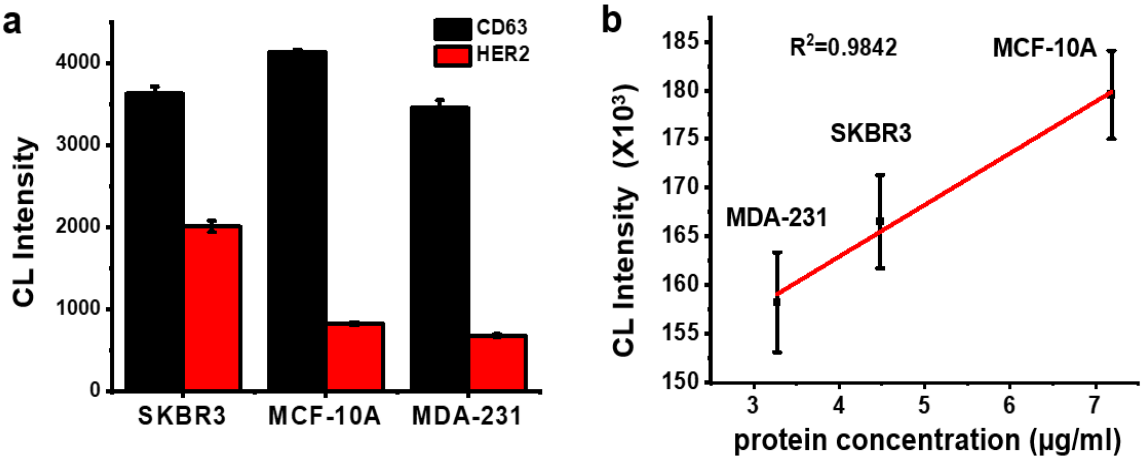

Figure 2.4 *Detection of cell released EVs using CuS-MG. The cell culture medium was collected from three cell lines: MCF-10A, MDA-231 and SK-BR-3. a) Chemiluminescence resulted from EV detection in the culture media of three cell lines targeting CD63 and anti-HER2; b) Linear correlation between CD63 quantification results obtained by ELISA and the chemiluminescent signals from CuS-MG in our assay targeting CD63. [ABEI] = 0.5 mM, [H_2O_2] = 1 mM, pH=11.*

2.4 Conclusions

To summarize, we have developed a method that utilize the CuS-enclosed MG and membrane filters for sensitive and fast detection of EVs in buffer, cell culture medium and biospecimen like serum. Our design offers two unique features: we employ the encapsulated Cu^{2+} for signal amplification, and the filtration process for EV enrichment from a large volume. Using the large number of Cu^{2+} enclosed in each MG, highly intense CL could be emitted with few numbers of EVs. As low as 10^4 particles/mL EVs were detected with our method targeting two different EV surface proteins. Besides, through the filtration process, our method can provide accurate quantification of EVs by removing influence from contaminants and matrix components. We also demonstrated the possibility of applying this method for direct and highly efficient quantification of EVs in serum or in culture medium, consuming much fewer samples than ELISA. Such a capability will benefit study of EV functions and biogenesis, as well as be suitable for disease diagnosis based on EV markers.

Supporting Information

Supporting figures

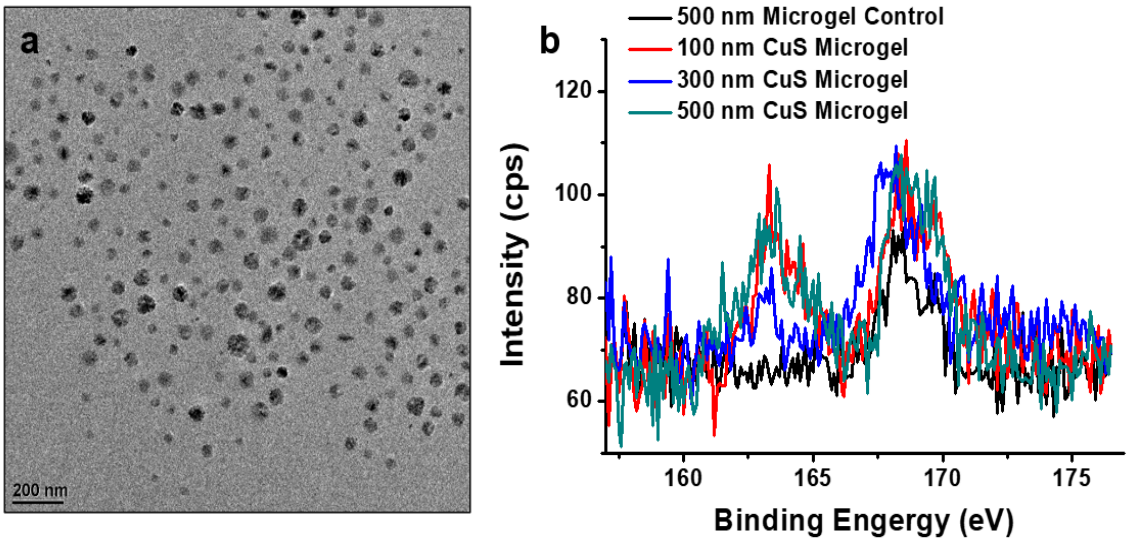

c

Type	Zeta Potential（mV）
original microgel	-19.28±2.86
CuS microgel	-23.59±2.03

Figure S2.1 *a) TEM of 100nm MG, b) XPS (S 2p) spectrum of three sized CuS MG and no CuS MG, c) Zeta potential of original MG and CuS MG.*

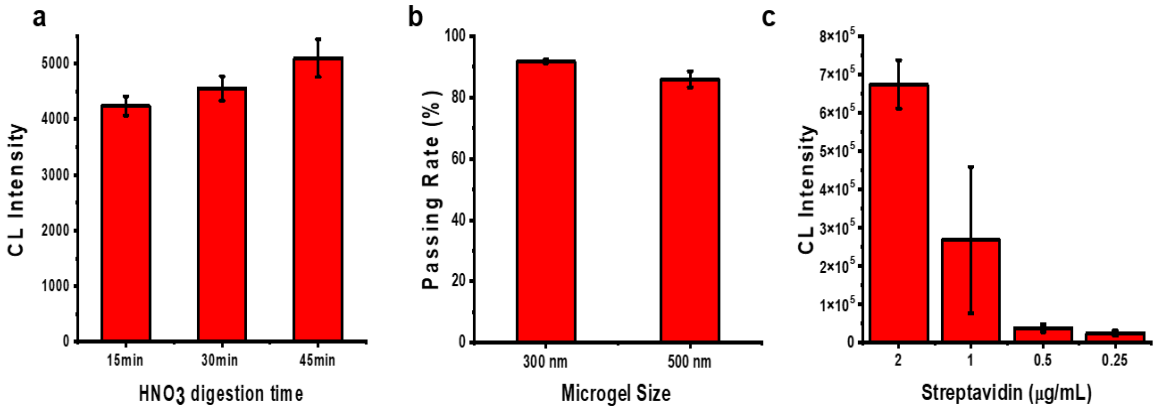

Figure S2.2 *a) Influence of acid digestion time to chemiluminescence; b) Passing rate (0.45 µm filter membrane) of MGs with 300 nm and 500 nm size; c) Optimization of streptavidin concentration for CuS MG labelling. MG concentration is* 5×10^9 *particles/ml for all streptavidin concentrations.*

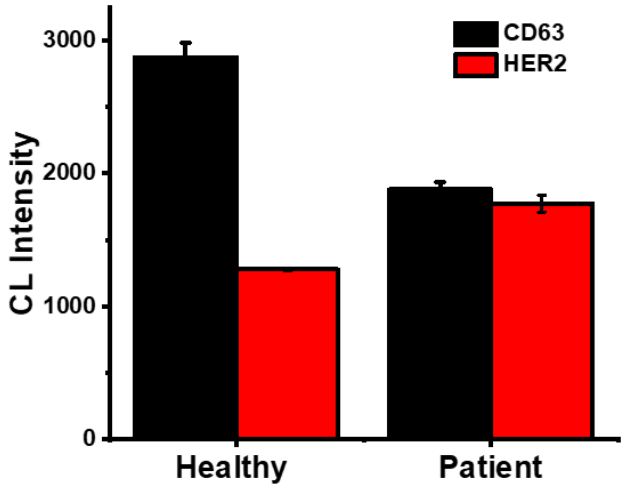

Serum	CD63 (10^x EV)	HER2 (10^x EV)
Healthy	9.87	-
Patient	4.30	5.79

Figure S2.3 *Quantification of exosome in healthy and breast cancer patient serum.With the calibration curve prepared by serial dilution of the lyophilized EV from COLO 1 cell line (HansaBioMed Life Sciences), we can also obtain the concentration of EVs present in the serum samples. It turns out that, in the 100× diluted serum, the concentration of the CD63-positive EVs was about* $6.92\pm0.27\times10^9$ *EVs/mL while that of the HER2-positive EVs being comparable to the background signal in the serum from the healthy individual. In the serum sample from the cancer patient, the CD63- and HER2-positive EVs was found to be about* $2.00\pm0.03\times10^4$*, and* $6.17\pm0.22\times10^5$*, respectively.*

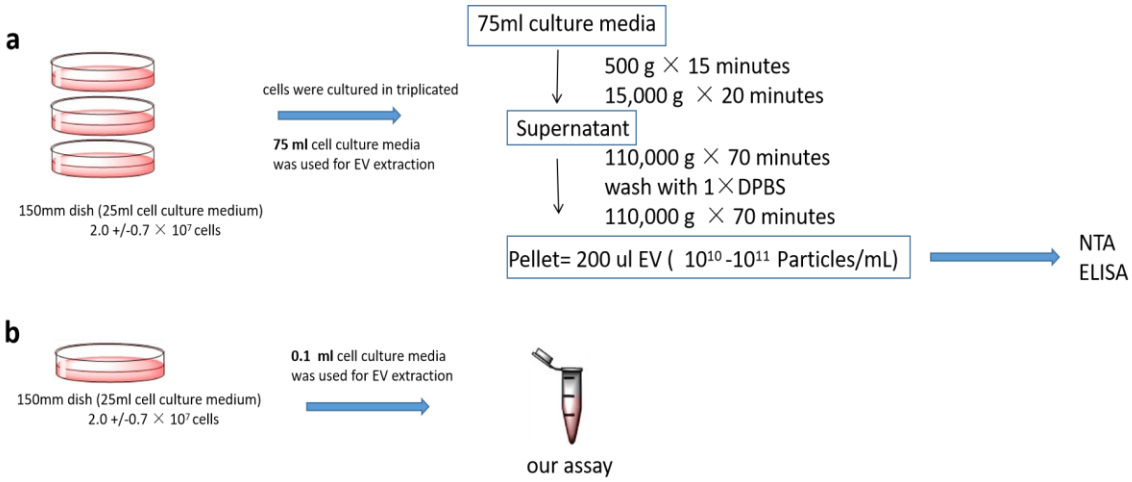

Figure S2.4 *Compare our assay with standard assay*

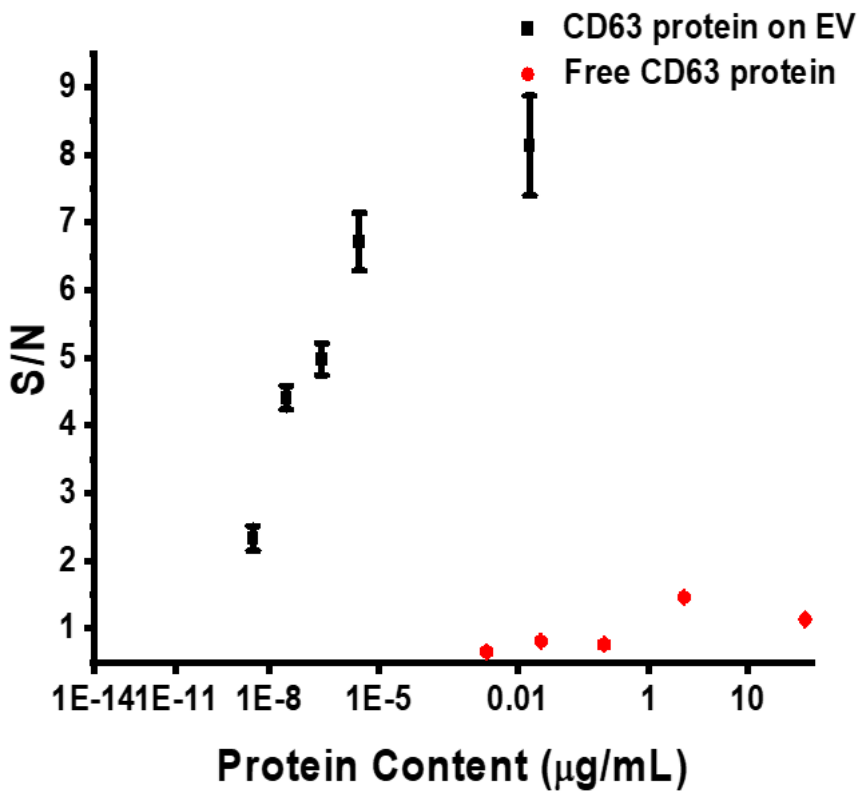

Figure S2.5 *Compare detection of EV and free CD63 protein by CuS MG.*

Supporting Tables

Microgel Name	**Size (DLS)**	**Recipe**	**Bis (%)**	**ALA addition time**
100 nm	83.2 ±16.1	NIPAM: 0.152g Bis: 0.030g SDS: 0.045g AA: 0.048g KPS: 0.02g ALA:0.035g	12.8%	10 mins
300 nm	305.0±22.7	NIPAM: 0.152g Bis: 0.020g SDS: 0.0225g AA: 0.048g KPS: 0.005g ALA:0.035g	8.5%	10 mins
500 nm	539.8±35.6	NIPAM: 0.152g Bis: 0.020g SDS: 0.0225g AA: 0.048g KPS: 0.005g ALA:0.035g	8.5%	1 hour

Table S2.1 *Recipe of the three synthesized MGs.*

Method	LOD (particles/µL)	Linear Range (particles/µL)	Reference
Electrochemical immunosensor	200	10^2 -10^6	[33]
Integrated magneto-electrochemical sensor	1×10^4	10^4-10^7	[34]
Size Exclusion chromatography	3.9×10^4	1×10^5-1.5×10^6	[35]
Microfluidic analysis	50	10^2-10^6	[36]
Bivalent-Cholesterol-Labeled DNA	2.2×10^3	~10^3-10^5	[37]
Electrochemical Detection	20	10^1-10^9	[38]
Graphitic Carbon Nitride Nanosheets	1.3×10^5	1.9×10^6-3.4×10^7	[39]
DNA-capped single-walled carbon nanotubes	5.2×10^5	1.8×10^6-2.2×10^7	[40]
Electrochemical Detection	70	10^3-10^5	[41]
Copper-Mediated Signal Amplification	4.8×10^4	7.5×10^4-1.5×10^7	[42]
Magnetic-Based Microfluidic Device	4.4×10^3	7.6×10^4-7.6×10^8	[43]
Aptamer based amplification	1.16×10^3	1.75×10^3 - 7.0×10^6	[44]
Gold-loaded ferric oxide nanocubes	1×10^3	10^3-10^7	[45]

Table S2.2 *Currently methods for EV detection.*

References

1. Gorelikov, I., Field, L.M. & Kumacheva, E.J.J.o.t.A.C.S. Hybrid microgels photoresponsive in the near-infrared spectral range. **126**, 15938-15939 (2004).

2. Coumans, F.A. et al. Methodological guidelines to study extracellular vesicles. **120**, 1632-1648 (2017).

3. Zhang, J., Xu, S. & Kumacheva, E. Polymer microgels: reactors for semiconductor, metal, and magnetic nanoparticles. *J. Am. Chem. Soc.* **126**, 7908-7914 (2004).

4. Liu, Y. et al. Encapsulation of ionic nanoparticles produces reactive oxygen species (ROS)-responsive microgel useful for molecular detection. *Chem. Commun.* **54**, 4329-4332 (2018).

5. Zhang, S., Zhong, H. & Ding, C. Ultrasensitive flow injection chemiluminescence detection of DNA hybridization using signal DNA probe modified with Au and CuS nanoparticles. *Anal. Chem.* **80**, 7206-7212 (2008).

6. Lyu, L., Zhang, L. & Hu, C. Enhanced Fenton-like degradation of pharmaceuticals over framework copper species in copper-doped mesoporous silica microspheres. *Chem. Eng. J.* **274**, 298-306 (2015).

7. Adcock, J.L., Barnett, N.W. & Francis, P.S. in Encyclopedia of Analytical Science (Third Edition). (eds. P. Worsfold, C. Poole, A. Townshend & M. Miró) 412-419 (Academic Press, Oxford; 2019).

8. Merchant, M.L. et al. Microfiltration isolation of human urinary exosomes for characterization by MS. *PROTEOMICS–Clinical Applications* **4**, 84-96 (2010).

9. Konoshenko, M.Y., Lekchnov, E.A., Vlassov, A.V. & Laktionov, P.P. Isolation of extracellular vesicles: general methodologies and latest trends. *BioMed research international* **2018** (2018).

10. Li, P., Kaslan, M., Lee, S.H., Yao, J. & Gao, Z. Progress in exosome isolation techniques. *Theranostics* **7**, 789 (2017).

11. Khajvand, T., Akhoondi, R., Chaichi, M.J., Rezaee, E. & Golchoubian, H. Two new dinuclear copper (II) complexes as efficient catalysts of luminol chemiluminescence. *J. Photochem. Photobiol. A: Chem.* **282**, 9-15 (2014).

12. Nichela, D.A., Berkovic, A.M., Costante, M.R., Juliarena, M.P. & Einschlag, F.S.G. Nitrobenzene degradation in Fenton-like systems using Cu (II) as catalyst.

Comparison between Cu (II)-and Fe (III)-based systems. *Chem. Eng. J.* **228**, 1148-1157 (2013).

13. Doldán, X., Fagúndez, P., Cayota, A., Laíz, J. & Tosar, J.P. Electrochemical sandwich immunosensor for determination of exosomes based on surface marker-mediated signal amplification. *Anal. Chem.* **88**, 10466-10473 (2016).

14. Jeong, S. et al. Integrated magneto–electrochemical sensor for exosome analysis. *ACS nano* **10**, 1802-1809 (2016).

15. Xu, R. et al. Quantification of small extracellular vesicles by size exclusion chromatography with fluorescence detection. *Anal. Chem.* **88**, 10390-10394 (2016).

16. Zhang, P., He, M. & Zeng, Y. Ultrasensitive microfluidic analysis of circulating exosomes using a nanostructured graphene oxide/polydopamine coating. *Lab on a Chip* **16**, 3033-3042 (2016).

17. He, F., Liu, H., Guo, X., Yin, B.-C. & Ye, B.-C. Direct exosome quantification via bivalent-cholesterol-labeled DNA anchor for signal amplification. *Anal. Chem.* **89**, 12968-12975 (2017).

18. Wang, S. et al. Aptasensor with expanded nucleotide using DNA nanotetrahedra for electrochemical detection of cancerous exosomes. *ACS nano* **11**, 3943-3949 (2017).

19. Wang, Y.-M. et al. Enhancement of the intrinsic peroxidase-like activity of graphitic carbon nitride nanosheets by ssDNAs and its application for detection of exosomes. *Anal. Chem.* **89**, 12327-12333 (2017).

20. Xia, Y. et al. A visible and colorimetric aptasensor based on DNA-capped single-walled carbon nanotubes for detection of exosomes. *Biosens. Bioelectron.* **92**, 8-15 (2017).

21. Dong, H. et al. Highly Sensitive Electrochemical Detection of Tumor Exosomes Based on Aptamer Recognition-Induced Multi-DNA Release and Cyclic Enzymatic Amplification. *Anal. Chem.* **90**, 4507-4513 (2018).

22. He, F., Wang, J., Yin, B.-C. & Ye, B.-C. Quantification of exosome based on a copper-mediated signal amplification strategy. *Anal. Chem.* **90**, 8072-8079 (2018).

23. Xu, H., Liao, C., Zuo, P., Liu, Z. & Ye, B.-C. Magnetic-based microfluidic device for on-chip isolation and detection of tumor-derived exosomes. *Anal. Chem.* **90**, 13451-13458 (2018).

24. Gao, M.-L., He, F., Yin, B.-C. & Ye, B.-C. A dual signal amplification method for exosome detection based on DNA dendrimer self-assembly. *Analyst* **144**, 1995-2002 (2019).

25. Boriachek, K. et al. Avoiding Pre-Isolation Step in Exosome Analysis: Direct Isolation and Sensitive Detection of Exosomes Using Gold-Loaded Nanoporous Ferric Oxide Nanozymes. *Anal. Chem.* **91**, 3827-3834 (2019).

26. Shen, W. et al. A single extracellular vesicle (ev) flow cytometry approach to reveal ev heterogeneity. *Angewandte Chemie International Edition* **57**, 15675-15680 (2018).

27. Lee, K. et al. Multiplexed profiling of single extracellular vesicles. *ACS nano* **12**, 494-503 (2018).

28. Ji, Y. et al. Multiplexed profiling of single-cell extracellular vesicles secretion. *Proceedings of the National Academy of Sciences* **116**, 5979-5984 (2019).

29. Im, E.-J. et al. Sulfisoxazole inhibits the secretion of small extracellular vesicles by targeting the endothelin receptor A. *Nature communications* **10**, 1387 (2019).

30. Benedikter, B.J., Wouters, E.F., Savelkoul, P.H., Rohde, G.G. & Stassen, F.R. Extracellular vesicles released in response to respiratory exposures: implications for chronic disease. *Journal of Toxicology and Environmental Health, Part B* **21**, 142-160 (2018).

31. Théry, C., Amigorena, S., Raposo, G. & Clayton, A. Isolation and characterization of exosomes from cell culture supernatants and biological fluids. *Current protocols in cell biology* **30**, 3.22. 21-23.22. 29 (2006).

32. Fang, S. et al. Clinical application of a microfluidic chip for immunocapture and quantification of circulating exosomes to assist breast cancer diagnosis and molecular classification. *PLoS One* **12**, e0175050 (2017).

33. Doldán, X., Fagúndez, P., Cayota, A., Laíz, J. & Tosar, J.P.J.A.c. Electrochemical sandwich immunosensor for determination of exosomes based on surface marker-mediated signal amplification. **88**, 10466-10473 (2016).

34. Jeong, S. et al. Integrated magneto–electrochemical sensor for exosome analysis. **10**, 1802-1809 (2016).

35. Xu, R. et al. Quantification of small extracellular vesicles by size exclusion chromatography with fluorescence detection. **88**, 10390-10394 (2016).

36. Zhang, P., He, M. & Zeng, Y.J.L.o.a.C. Ultrasensitive microfluidic analysis of circulating exosomes using a nanostructured graphene oxide/polydopamine coating. **16**, 3033-3042 (2016).

37. He, F., Liu, H., Guo, X., Yin, B.-C. & Ye, B.-C.J.A.c. Direct exosome quantification via bivalent-cholesterol-labeled DNA anchor for signal amplification. **89**, 12968-12975 (2017).

38. Wang, S. et al. Aptasensor with expanded nucleotide using DNA nanotetrahedra for electrochemical detection of cancerous exosomes. **11**, 3943-3949 (2017).

39. Wang, Y.-M. et al. Enhancement of the intrinsic peroxidase-like activity of graphitic carbon nitride nanosheets by ssDNAs and its application for detection of exosomes. **89**, 12327-12333 (2017).

40. Xia, Y. et al. A visible and colorimetric aptasensor based on DNA-capped single-walled carbon nanotubes for detection of exosomes. **92**, 8-15 (2017).

41. Dong, H. et al. Highly sensitive electrochemical detection of tumor exosomes based on aptamer recognition-induced multi-DNA release and cyclic enzymatic amplification. **90**, 4507-4513 (2018).

42. He, F., Wang, J., Yin, B.-C. & Ye, B.-C.J.A.c. Quantification of exosome based on a copper-mediated signal amplification strategy. **90**, 8072-8079 (2018).

43. Xu, H., Liao, C., Zuo, P., Liu, Z. & Ye, B.-C.J.A.c. Magnetic-based microfluidic device for on-chip isolation and detection of tumor-derived exosomes. **90**, 13451-13458 (2018).

44. Gao, M.-L., He, F., Yin, B.-C. & Ye, B.-C.J.A. A dual signal amplification method for exosome detection based on DNA dendrimer self-assembly. **144**, 1995-2002 (2019).

45. Boriachek, K. et al. Avoiding pre-isolation step in exosome analysis: direct isolation and sensitive detection of exosomes using gold-loaded nanoporous ferric oxide nanozymes. **91**, 3827-3834 (2019).

Chapter III. Bimetallic Metal–Organic Framework Fe/Co-MIL-88(NH_2) Exhibiting High Peroxidase-like Activity and Its Application in Detection of Extracellular Vesicles

3.1 Introduction

Metal organic frameworks (MOFs) are porous crystalline materials constructed from metal ions or metal cluster nodes and organic linkers with high regularity of coordination bonds. They can be formed from diverse metal cations like Cu^{2+}, Co^{2+}, Fe^{3+}, Ga^{3+}, etc., and ligands like carboxylates, phosphonates, or N-donating azolate linkers. By changing the type and ratio of the metal and ligand in the MOF frameworks, their structures and pore sizes can be tuned. Their tunable physicochemical properties and porous structures permit MOFs to be employed in many areas, such as catalysis,[1] gas storage and separation,[2, 3] energy production and conversion.[4, 5]

In recent years, their application scope has been expanded to biomedical sensing and imaging, taking advantage of their reversible metal-ligand coordination structure and high loading capacity.[6, 7] Most interestingly, the tailorable cavities with a high number of exposed unsaturated metal sites and channels formed from diverse metal nodes and bridging linker in MOFs mimic the coordination environment and electron transfer routes in natural enzymes.[8, 9] Several types of MOFs have been discovered to possess intrinsic peroxidase-mimicking catalytic activity, including the zeolitic imidazolate frameworks (ZIFs), the Fe-based MIL-MOFs (MIL = Material Institute of Lavoisier), the Zr-based UiO-

MOFs (UiO = University of Olso), the Cu-based HKUST-MOFs (HKUST = Hong Kong University of Science and Technology), the Ni-based MOFs, MIL101 (Fe, Co)@MIP, and the Prussian blue-based MOFs.[10-14] These MOF-based peroxidase mimics often contain transition metals like Fe, Co, Ni, Cu, etc., because such metals can catalyze generation of free radicals. For example, Fe can catalyze the Fenton reaction that produces hydroxyl radicals from H_2O_2. Superior to the biological enzymes, like horseradish peroxidase (HRP) employed in enzyme-linked immunosorbent assay (ELISA), MOFs have highly tunable catalytic activity and can be synthesized at lower costs in a larger scale,[15-17] attracting great attention in biosensing.

Herein, a bimetallic MIL-88 MOF was synthesized by using 2-aminoterephthalate as the ligand and both Fe and Co as metal cations. This bimetallic Fe/Co-MIL-88(NH_2) shows high peroxidase-like activity and high dispersity in aqueous solutions. It can act as the peroxidase-mimic and work together with glucose oxidase (GOx) in the cascade enzymatic reactions to oxidize the peroxidase substrate by inputting glucose. This reaction system can be used for sensitive EV detection in biological samples, and acquire the detection limit two orders of magnitude lower than that obtained with HRP, proving the feasibility of the peroxidase-mimicking bimetallic MOFs being promising tools in liquid biopsy. In addition, Fe/Co-MIL-88(NH_2) was used as a labeling tag for sandwich Elisa in replace of HRP and archiving the detection limit three orders of magnitude lower than that obtained with HRP based Elisa.

3.2 Experimental Section

Materials. Ferric chloride, 6-hydrate ($FeCl_3 \cdot 6H_2O$, 98.1%) was acquired from J. T. Baker (Phillipsburg, NJ). Sodium chloride, potassium phosphate dibasic salt (anhydrous), acetic acid, N, N-dimethylformamide (DMF) and cobalt(II) nitrate hexahydrate ($Co(NO_3)_2 \cdot 6H_2O$, 99%) were purchased from Fisher Scientific (Waltham, MA). 2-Aminoterephthalic acid ($H_2(NH_2)BDC$), TMB (3,3', 5,5"-tetramethylbenzidine), polyethylene glycol 400, potassium chloride, glycine (for electrophoresis, ≥99%) and glutaraldehyde solution were from Sigma-Aldrich (Saint Louis, MI). Ethanol (EtOH, Anhydrous) was from KOPTEC. The amino group modified CD63 aptamer was produced by IDT, Inc. (Coralville, IA). The mouse anti-human CD9 (Clone MM2/57) and HRP were obtained from Sino Biological (Beijing, China) and Cell Signaling Technology (Danvers, MA), respectively. Streptavidin was purchased from Thermo Fisher Scientific (Waltham, MA). All chemicals were at the analytical reagent grade and used without further purification. Ultrapure water with electric resistance > 18.2 MΩ was produced by the Milipore Milli-Q water purification system (Billerica, MA).

Synthesis and activation of Fe-MIL-88(NH_2) and Fe/Co-MIL-88(NH_2). The MOF materials were prepared via a solvothermal method. In a typical approach for production of the bimetallic Fe/Co-MIL-88(NH_2), 0.082 g $FeCl_3 \cdot 6H_2O$, 0.090 g $Co(NO_3)_2 \cdot 6H_2O$, and 0.053 g $H_2(NH_2)BDC$ were dissolved in 3.181 g DMF in a 23 mL glass bottle, stirred for 40 min, and then heated in 120 °C for 24 hours. After cooling down to room teperature, the brown-color crystal Fe/Co-MIL-88(NH_2) were washed with DMF, collected by centrifugation, and dried at room temperature. The monometalic Fe-MIL-88(NH_2) was

synthesized in the same way, but by mixing 0.163 g $FeCl_3 \cdot 6H_2O$ and 0.057 g $H_2(NH_2)BDC$ in 3.058 g DMF, and heated in 140 °C. Both MOF crystals were washed twice with ethanol at 60 °C or room temperature, and then dried by vacuum to remove the residual DMF that may impede with the subsequent enzyme activity measurement and sensing performance.

Powder X-ray Diffraction (PXRD) Characterization. The phase purity of Fe-MIL-88(NH_2) and Fe/Co-MIL-88(NH_2) was examined by powder X-ray diffraction on a PANalytical Empyrean Series 2 diffractometer operated at 45 kV and 40 mA (Cu Kα radiation, λ = 1.5418 Å). The data collection was performed at room temperature in the range from 5° to 40° with a step size of ~0.026°. The simulated Fe-MIL-88(NH_2) powder pattern was obtained from the Fe-MIL-88(NH_2) single crystal data.[18]

Peroxidase-like activity evaluation of Fe/Co-MIL-88(NH_2) and Fe/Co-MIL-88(NH_2). The peroxidase-like activity of the two MOF materials was evaluated using the reaction between H_2O_2 and 3,3′,5,5′-tetramethylbenzidine (TMB). In brief, 50 μg/mL MOF, 1 mM TMB, and H_2O_2 at various concentrations (0, 0.005, 0.05, 0.1, 0.5 and 1 mM) were added to 0.4 mL of 200 mM NaAc-HAc buffer (pH 4.1). The mixture was incubated at 37° C for 15 min, and the visible light absorbance at 652 nm of the TMB oxidation product, i.e. oxTMB, was read in the synergy HT microplate reader.

Enzyme Kinetics Analysis of activated Fe/Co-MIL-88(NH_2). The steady-state kinetics assays were performed as follows. The activated Fe/Co-MIL-88(NH_2) at the concentration of 50 μg/ml in 100 μL of 200 mM NaAc-HAc buffer (pH 4.1) was incubated with 1.0 mM TMB and H_2O_2 at various concentrations (0, 0.05, 0.1, 0.5, 1.0, and 10 mM)

at 37°C. A time-course mode was used to monitor the absorbance change at 652 nm with a 10 s interval for 15 min in the synergy HT microplate reader. The Beer–Lambert law was used to convert the absorbance to oxTMB concentration using the molar absorptivity at 652 nm of oxTMB (39,000 $M^{-1} \cdot cm^{-1}$)[19] and the optical length of 0.233 cm of the 96 well plates. The slope of the concentration change within the first 15 min time period was then calculated to represent the initial velocity (V).

Preparation of Fe/Co-MIL-88(NH_2)/Aptamer Bioconjugate. Aptamer conjugation started by dispersing 35 mg Fe/Co-MIL-88(NH_2) in 20 ml 1× PBS, followed by addition of 100 µl glutaraldehyde. After stirring the solution for 2 hours, the solid was centrifuged down, washed with 1× PBS for 2 times, and dispersed in 2 ml 1× PBS. Next, 10 µL of 0.1mM aptamer was added to the mixture and the solution was put on a rotating plate and shaken overnight. The Fe/Co-MIL-88(NH_2)/ aptamer conjugate was then collected by centrifugation (20,000 *g*, 3 min), and redispersed in 2 ml 0.1 M glycine buffer containing 8 mM PEG for 1 hour to passivate the MOF surface.

Cell culture and EV collection. HeLa cells (HeLa ATCC® CCL- 2™) were cultured in DMEM medium (Corning) containing 10% fetal bovine serum (FBS, Gibco) and 1% penicillin/streptomycin (Corning). All cell lines were maintained at 37 °C in a humidified 5% CO_2 incubator and routinely screened for Mycoplasma contamination. EV harvest was carried out by a Sorvall™ ST 16 Centrifuge (Thermo Fisher Scientific) and an Optima XPN-80 ultracentrifuge (Beckman Coulter). The medium was replaced with the EV-depleted culture medium after the cells reached a confluency of 75%. The cells were cultured for 24-48 hours in this medium, which was then centrifuged at 500 *g* for 15 min

to sediment the cells, and another 20-min centrifugation at 15,000 *g* to remove the remaining cellular debris. Next, the medium was ultra-centrifuged at 110,000 *g* for 70 min to harvest the EVs released by the cells. The EV pellet was washed once and re-suspended in the freshly prepared 1× PBS. The EV solution was used within three days of preparation.

Detection of EV relying on the HRP-mimicking activity of Fe/Co-MIL-88(NH_2). Twenty µl of the EV sample was mixed with 170 µl of the Fe/Co-MIL-88(NH_2)/aptamer bioconjugate at 17.5 mg/mL and 10 µl of the biotin-anti-CD9 antibody solution at 0.10 mg/ml. The mixture was shaken at room temperature for 3 hrs. The Fe/Co-MIL-88(NH_2)/aptamer -EV-anti-CD9 antibody was centrifuged down (20,000 *g*, 3 min) and resuspended in 100 µl of the streptavidin solution at 17 µg/ml. After 1-hour incubation, the product was centrifuged down (20,000g, 3 min), washed with 1×PBS for 1 time, and mixed with 100 µl biotin-GOx at 0.013 mg/ml. After two washes with 1×PBS, the final product was resuspended in 30 µl 1× PBS, 20 µl of which was mixed with 5 µl TMB (40 mM), 5 µl glucose (40 mM) and 370 µl NaAc-HAc buffer and incubated in 37 ˚C for 1 hour. With the MOF bioconjugates removed by centrifugation, the clear solution was tested in the synergy HT microplate reader (BioTek Instruments, Inc.).

3.3 Result and Discussion

Design and characterization of bimetallic Fe/Co-MIL-88(NH_2) MOFs. For reliable applications of the MOF-based peroxidase mimics, dispersity and stability in aqueous solution are critical.[20] The Fe-based MIL-88 MOF has high aqueous compatibility because it uses hydrophilic bridging ligands like 2-aminoterephthalic acid, which also bring in the benefit of easy conjugation with biomolecules like antibodies.[21, 22] It has also been reported to possess peroxidase-like activity. The porous structure of MIL-88 exposes plenty of Fe(III) on surface that can serve as the activity centers to catalyze the heterogeneous Fenton reactions at the solid/liquid interface. In aqueous solutions, the unsaturated, open iron sites can be terminated by water or hydroxide.[23, 24] If these non-bridging ligands are replaced by the Lewis base H_2O_2, Fe(III) can be reduced to Fe(II),[25, 26] which then reacts directly with H_2O_2 to generate hydroxyl radicals. In addition, incorporating the Fe-based reaction sites in the solid MOF structures can help prevent rapid diffusion of the iron ions and the radicals in the bulk solution during the Fe(III)/Fe(II) conversion cycles,[9, 25] enhancing the catalytic activity.

However, the rate of conversion of Fe(III) to Fe(II) is much slower than that of hydroxyl radical generation by Fe(II) reacting with H_2O_2, limiting its catalytic power.[27] Other transition metals can trigger Fenton-like reactions as well. For example, Co(II) can be oxidized by H_2O_2 to produce hydroxyl radicals and Co(III)OH, which can be recycled back to Co(II) to generate more radicals.[28, 29] The standard redox potential of the Co(III)/Co(II) pairs is 1.3 V, higher than that (0.771 V) of the Fe(III)/Fe(II) pairs.[29, 30] Some Co-based nanozymes have been reported and exhibited high catalytic activity.[31, 32] Preparation of

mixed metal MOFs having Fe in combination with other transition metals like Co and Zn have been proved to be possible.[33] We thus hypothesize that, adding Co(II) to the Fe-based MIL-88 MOF could improve its peroxidase-mimicking activity, while maintaining its biocompatibility (Figure 3.1a).

The bimetallic Fe/Co-MIL-88(NH_2) was synthesized by the solvothermal method,[21] as described in the Experimental Section. Fe(III) and Co(II) can coordinate with the carboxyl groups on the NH_2BDC^{2-} ligands, forming the trinuclear transition metal (TM) clusters (TM = Fe and Co) (Figure 3.1a). The Fe-MIL-88(NH_2) was also prepared with the same procedure for activity comparison. Because adding a second metal ion may affect the final morphology of MIL-88 and reduce its stability, we varied the mole ratio of Fe : Co used during the synthesis to see at what ratio a stable bimetallic structure can be obtained. We found that with the input ratio at 1:1, the synthesized Fe/Co-MIL-88(NH_2) MOF exhibited a hexagonal rod-like morphology with a lateral length of about 700 − 1,100 nm and an average diameter of 500 nm when examined by TEM (Figure 3.1b). DLS measurement showed that the average hydrodynamic diameter of the Fe/Co-MIL-88(NH_2) was around 600 nm, similar to Fe-MIL-88(NH_2) (Figure 3.1c). PXRD was also performed to characterize the crystal structure. The peaks of the Fe/Co-MIL-88(NH_2) matched well with those of the simulated Fe-MIL-88(NH_2) spectrum which confirmed the MIL-88 topology (Figure 3.1d). Small variations between the actual and simulated XRD spectra were observed: the flexibility of the MIL-88 architecture could lead to changes in peak position and shape.[34-36] Furthermore, we carried out EDS line scanning (Figure S3.1), and confirmed the coexistence of Fe (0.70 keV) and Co (0.77 keV) in the Fe/Co-MIL-88(NH_2)

framework. The atomic% of Fe and Co was found to be 7.18 % and 2.23 %, respectively, although the mole ratio of the two metals was 1:1 when added to the synthesis solution. Fe(III) is a harder Lewis acid compared to Co(II), and can bind more easily to the carboxylate anion, which is a hard Lewis base. Such a difference in the coordination capability between Fe and Co may contribute to the lower Co/Fe ratio incorporated in the framework compared to that in the starting materials. All these results support that, adding Co to this MOF structure at a 1:1 Fe : Co ratio does not affect the final morphology of MIL-88, and yields a stable MOF structure containing a certain level of Co. Further increase of the Co content in the bimetallic MOF turned out to greatly reduce the MOF stability.

The as-synthesized Fe/Co-MIL-88(NH_2) was initially distributed in DMF, the organic solvent used for synthesis. It was reported previously that, exchanging the high boiling point solvent DMF with a lower boiling point solvent like ethanol at elevated temperatures could release the DMF and free ligands resided in the stagnant pore space for the Fe- and MIL-based MOF.[37, 38] This process is called activation, and can enhance the access to the permanent porosity and increase the surface area of the MOF, which should promote H_2O_2 adsorption to result in higher catalytic activity. Thus, all of the MOF materials used in the following assays were treated by hot ethanol and dried in vacuum. The size distribution profile and the PXRD spectrum of the MOF were highly similar before and after activation (Figure S3.2), confirming that activation did not break or alter the coordination framework. Notably, the resultant MOF was very stable during dry storage: the DSL (Figure S3.3) and

PXRD (Figure S3.4) results of Fe/Co-MIL-88(NH_2) stored for 1 or 3 weeks at room temperature were the same as the freshly synthesized sample.

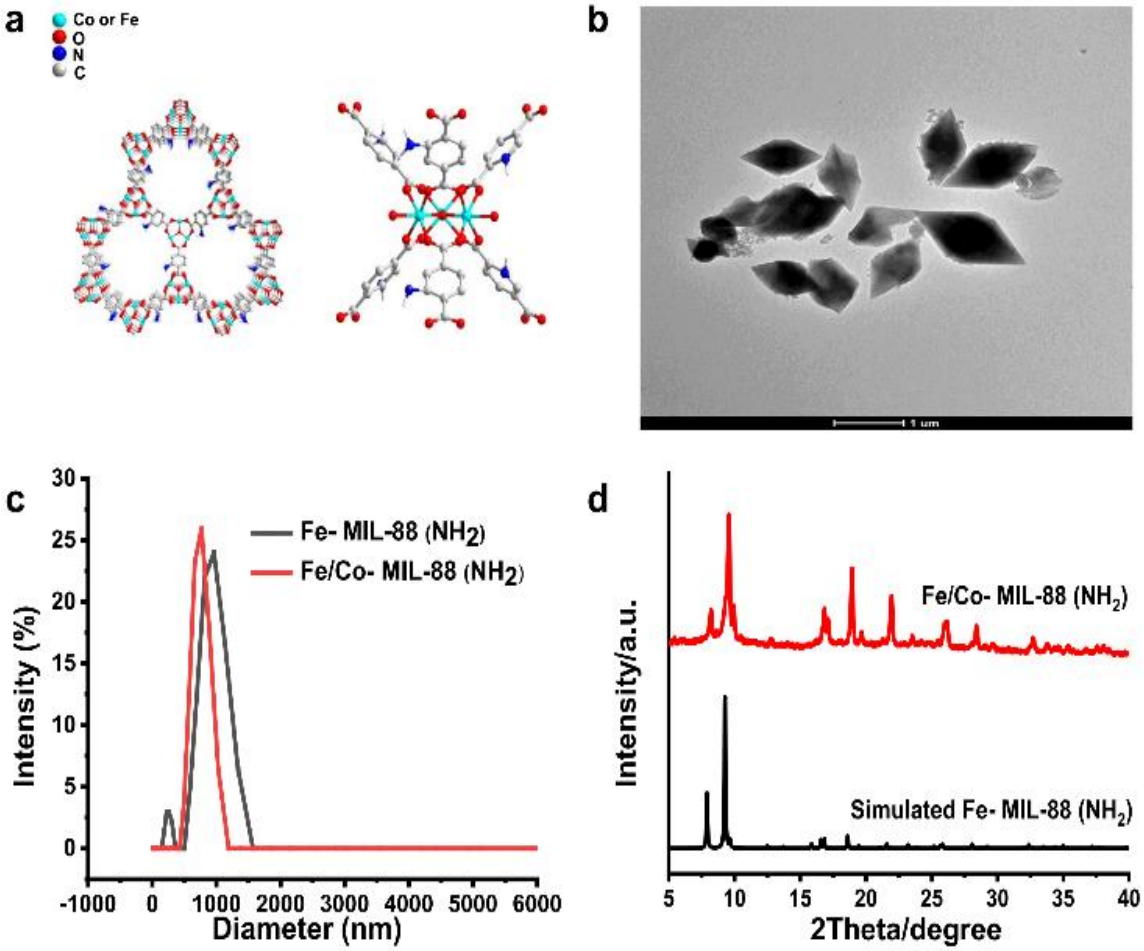

Figure 3.1 *MOF characterization. a) Structure schematic diagram and b) TEM image of Fe/Co-MIL-88(NH_2), c) DSL and d) powder XRD results for simulated Fe- MIL-88(NH_2) and synthesized Fe/Co-MIL-88(NH_2).*

Peroxidase-like Activity of Fe/Co-MIL-88(NH_2). We evaluated the peroxidase-like activities of Fe/Co-MIL-88(NH_2) MOF using the model reaction, i.e. the oxidation of the colorless TMB into the blue oxTMB by H_2O_2 (Figure 3.2a).[19] As seen from Figure 3.2b, the characteristic, visible light absorption at 652 nm for oxTMB was observed when mixing 25 µg/mL Fe/Co-MIL-88(NH_2) with 1.0 mM H_2O_2 and 1.0 mM TMB in 200 mM NaAc-

HAc buffer at pH 4.1. In contrast, the absorbance value was close 0 with only the MOF and H_2O_2, or with only the TMB and H_2O_2. These results point out that the bimetallic MOF could act like a peroxidase to catalyze reactions with H_2O_2. However, a small increase in absorbance observed by mixing the MOF with TMB indicates the existence of a low level of the oxidase-like activity, but the peak intensity was ~ 6.1 folds smaller than that generated by the reaction with MOF and H_2O_2. Low oxidase-like activity has also been reported in other Fe-based MOF materials.[39]

We also compared the catalytic activity of the pure Fe-based MIL-88(NH_2) MOF with that of the bimetallic one, both MOF materials going through the activation procedure. Using the same amount (5.0 μg) of the MOF crystals, Fe/Co-MIL-88(NH_2) indeed resulted in ~ 2.5-fold faster increase in absorbance along with increasing H_2O_2 concentrations than Fe-MIL-88(NH_2) (Figure 3.2c). At the highest H_2O_2 concentration tested, i.e. 1 mM, the bimetallic MOF produced a signal ~2.1 times higher. This result illustrates that, introduction of Co(II) does enhance the catalytic capability of the Fe-based MIL-88(NH_2). It is worth noting that, without "activation", the bimetallic MOF resulted in a signal increase with increasing H_2O_2 concentrations~3.5-fold slower than that obtained with the activated version (Figure S3.5), probably due to the lower access to the permanent pore surfaces with the trapped DMF solvent.

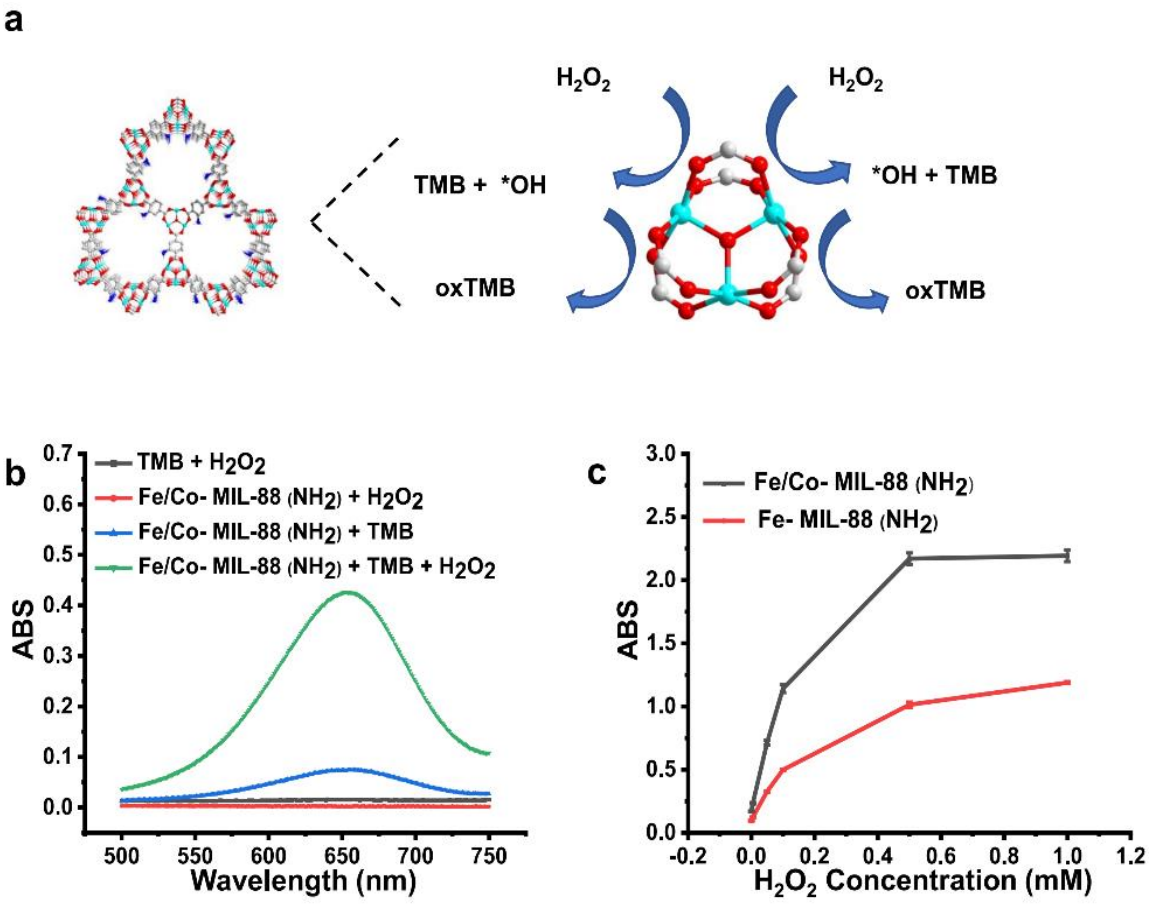

Figure 3.2 *Peroxidase-like activity of Fe/Co-MIL-88(NH_2). a) Schematic illustration of the reaction between TMB and H_2O_2 catalyzed by MOF; b) UV-Vis absorption spectra of the 200-µL mixture of 1.0 mM TMB and 1.0 mM H_2O_2 with or without 25 ug/ml MOF, and the two control reactions of mixing the MOF with TMB or H_2O_2 only. All reactions measured at 5 min; c) Absorbance (at λ = 652 nm) of oxTMB produced by the 15-min reaction of 1 mM TMB and various H_2O_2 concentrations catalyzed by 50 µg/ml Fe-MIL-88(NH_2) or Fe/Co-MIL-88(NH_2). All reactions took place in 200 mM NaAc-HAc buffer at pH 4.1.*

Steady-State Kinetics Analysis. More detailed assessment of the catalytic capability of the bimetallic MOF was carried out by the steady-state kinetic analysis. The absorbance change at 652 nm was monitored with the MOF at a fixed concentration reacting with varying TMB or H_2O_2 concentrations. The initial production rate (V in $\mu M.min^{-1}$) of oxTMB within the first 15-min of the reaction window (Figure 3.3a) was plotted against the H_2O_2 concentrations ([S]) to yield the Michaelis−Menten curve (Figure 3.3b). Rearranging Fig. 3.3b to the Lineweaver-Burk plot (Figure S3.6) can attain the Michaelis constant (K_m) and maximum reaction velocity (V_{max}) from the slope and Y-intercept of this linear regression curve: $[1/V = (K_m/V_{max}) \times (1/[S]) + 1/V_{max}]$. The catalytic constant (k_{cat}) can be obtained by dividing the V_{max} by the molar concentration of the "enzyme", the bimetallic Fe/Co-MIL-88(NH_2), which was calculated by counting the number of individual crystal dispersed in a solution of 10 µL under an optical microscope. The K_m and k_{cat} against the other substrate, TMB, was also measured (Figure S3.7). K_m indicates the binding affinity between the substrate and the enzyme, a smaller value representing a higher affinity. A high value of k_{cat} corresponds to a fast signal generation speed achievable per unit concentration of the enzyme.

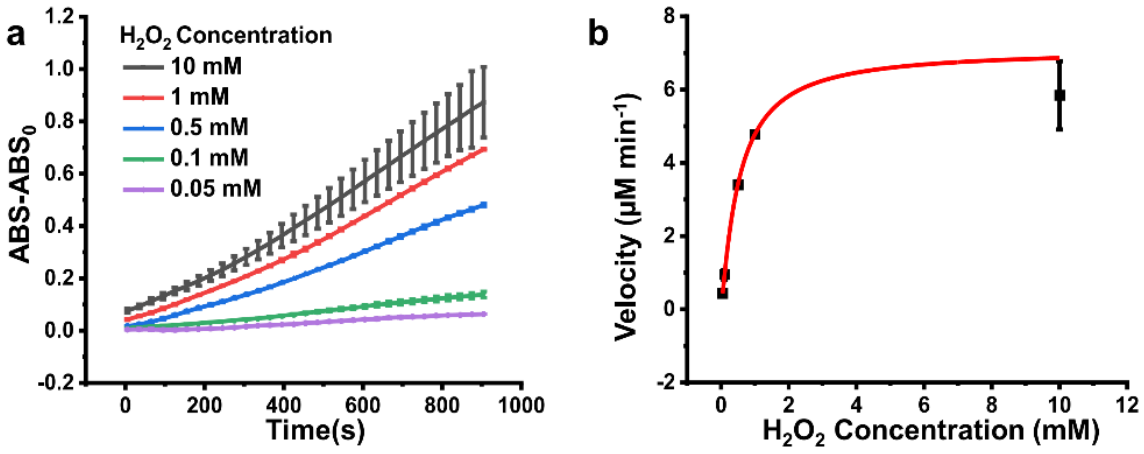

Figure 3.3 *Steady-state kinetics study. a) Increase of absorbance at λ = 652 nm between 0 and 900 seconds after mixing 1.0 mM TMB, 50 μg/mL Fe/Co-MIL-88(NH_2), and 0.050 – 10 mM H_2O_2; b) Plotting the initial reaction velocity calculated from the absorbance change shown in a) against the corresponding H_2O_2 concentrations. All reactions were in 200 mM NaAc-HAc buffer at pH 4.1.*

A K_m of 0.71 mM was found for Fe/Co-MIL-88(NH_2) to H_2O_2, smaller than that of the HRP and most of the MOF-based HRP mimics reported in literature (Table 3.1). In addition, the k_{cat} of Fe/Co-MIL-88(NH_2) measured with varying H_2O_2 concentrations were 3.8×10^4 s^{-1}, much larger than those of HRP. Similarly, the K_m and k_{cat} values related to TMB were also more optimal than the reported values. In particular, compared to the monometallic Fe-MIL-88 (NH_2), the bimetallic MOF has higher affinities to both TMB and H_2O_2, and higher values of k_{cat}. The high enzymatic activity could be owing to the highly porous MOF structure and the exposed metal sites on the MOF surface that strongly facilitate the binding and reaction with H_2O_2. Addition of the more active metal of Co also helps enhance the peroxidase-like activity of the Fe-based MOF. On the other hand, the high k_{cat} constant obtained from the bimetallic MOF we prepared could be attributed to its much larger average size (~ 700 – 1,100 nm in length × ~ 500 nm in diameter) compared to the MOF materials reported in Table 3.1 (dimensions ranging from 80 nm to 200 nm):

a larger crystal contains more metals than a smaller one per crystal, and thus more active sites.

Enzyme or Enzyme Mimicking MOF	Substrate	K_m [mM]	k_{cat} [S^{-1}]		Ref
HRP	TMB	0.43	$4.0*10^3$		40
	H_2O_2	3.7	$3.5*10^3$		
Co–Ferrocene MOF	TMB	-	-		41
	H_2O_2	28	-		
Copper hexacyanoferrate	TMB	-	-		42
	H_2O_2	72	-		
COF-MOF hybrid	TMB	0.29	14		43
	H_2O_2	0.46	10		
NH_2-MIL-88B (Fe)	TMB	1.0	5.0		
	H_2O_2	0.91	3.0		
Fe/Co-MIL-88 (NH_2)	TMB	0.16	$1.1*10^4$		This work
	H_2O_2	0.71	$3.8*10^4$		

Table 3.1 *Comparison of the catalytic parameters of HRP and HRP-mimicking MOFs.*

Bimetallic Fe/Co-MIL-88 (NH_2) as HRP-mimic for signal amplification via a cascade enzymatic reaction. The high peroxidase-mimicking activity possessed by Fe/Co-MIL-88 (NH_2) supports the feasibility that it can be exploited to detect the trace amounts of biomarkers like EVs in clinical samples for disease diagnosis and prognosis. Among different EV classes, exosomes derived from endosomes have attracted great attention in biomarker study, because their unique biogenesis pathways make them carry the molecular composition originated from their parent cells and reflective to the complex physiological states of the cell of origin.[44] We designed the detection assay that starts with using the MOF to isolate the target exosomes from samples and then employs the cascade enzymatic reaction for signal generation (Figure 3.4a), taking advantage of both the high

peroxidase-like activity. The large physical size of the MOF is suitable for exosome isolation from samples for enrichment and purification before detection, because it can be rapidly centrifuged down and removed from solutions. Since multiple surface proteins could present on the surface of each exosome captured by the MOF, they could bind to multiple copies of the GOx-labeled antibodies to catalyze the reaction between glucose and oxygen and generate H_2O_2, the substrate for the peroxidase-like MOF. Like in the enzyme activity measurements mentioned above, TMB can be oxidized and the signal of oxTMB can be used to quantify the target exosomes in samples.

We first tested the feasibility of the cascade enzymatic reaction by conjugating the GOx with biotin and the MOF with streptavidin. Pulling down the biotinylated GOx by the streptavidin-conjugated MOF produced the blue oxTMB in 200 mM acetate buffer (pH 4.1), when supplied with glucose and TMB. We also explored the conditions of the detection platform, and found that, 6.0 mg MOF yielded a relatively higher change in the absorbance signal from oxTMB than 3.0 and 0.30 mg (Figure S3.8). In consideration of keeping material consumption low, we chose to use 3.0 mg in the following experiments. We also found that, among the different glucose (0.50, 1.0, 2.0, 15 mM) and TMB (0.50, 1.0, and 1.5 mM) concentrations tested, the lowest concentrations led to the largest signal to background ratio (Figure S3.8), because higher substrate concentrations significantly increased the background signal with low GOx concentrations. We speculate that, with a high glucose concentration, the speed of H_2O_2 generation may exceed that of H_2O_2 decomposition. The accumulated H_2O_2 could oxidize TMB to result in high background.

Under the optimal reaction condition, i.e. using 3.0 mg MOF, 0.50 mM glucose and 0.50 mM TMB, as low as 0.17 nM GOx could be detected (Figure S3.8).

Next, we employed the bimetallic MOF to detect exosomes in biological samples. Since CD63 is a specific tetraspanin marker displayed on exosome surface, we labeled the bimetallic MOF with the anti-CD63 aptamer for exosome capture, using glutaraldehyde as the crosslinker. Glutaraldehyde firstly reacted with the $–NH_2$ groups on the surface of the bimetallic MOF, and then linked with the NH_2-modified aptamer (Figure S3.9a). The residual reactive glutaraldehyde was quenched by 0.1 M glycine, and the MOF surface was further covered by polyethylene glycol (PEG) through physical adsorption to prevent non-specific binding. Size measurement by DLS displayed comparable size distribution profiles of the Fe/Co-MIL-88(NH_2) with or without glutaraldehyde modification (Figure S3.9b). However, aptamer conjugation caused ~23% reduction of the signal-to-noise ratio generated from the MOF-catalyzed TMB oxidation, while further surface passivation with PEG had little effect on the peroxidase activity of MOF (Figure S3.9c). Substrate access to the open metal site on MOF surface may be impeded by the conjugated aptamer and ad adsorbed PEG. Aptamer could also increase the negative charges on the MOF surface that may reduce the affinity of the electron-rich substrates of TMB and H_2O_2.

Then the biotinylated anti-CD9 was employed to bind to another specific tetraspanin marker for exosome, CD9, on exosome surface. We chose to use streptavidin to bridge the biotinylated GOx on the MOF and the biotinylated anti-CD9 on exosome. In this way, the detection antibody or GOx was conjugated with the small biotin tag that imposes negligible impedance to their biological activities. In addition, we expect the multiple layers of the

biotin-streptavidin assembly may help immobilize more GOx on each MOF surface through attachment of exosomes, which could be at limited amounts in biological samples. Using the standard exosomes purchased from a commercial supplier and 3.0 mg MOF, we confirmed that the cascade enzymatic reaction using GOx and peroxidase-mimicking MOF can detect exosomes dispersed in 1× PBS at concentrations ranging from 1.6×10^5 - 1.6×10^6 particles/mL (P/mL) (Figure 3.4b). The limit of detection (LOD) was calculated to be 7.8×10^4 P/mL with the 3σ method. Such a detection range is lower than that obtained by NTA (10^8–10^9 P/mL) and the HRP-based ELISA (between 10^6 ~ 10^8 P/mL) (Figure S3.10).[45, 46]

Exosome detection in biological samples. With the superior detection performance demonstrated for the bimetallic MOF, we applied the assay to detect exosomes in cell culture medium and human serum. We harvested the exosomes in the culture medium of HeLa cells for 12, 24, and 48 hrs, and took 1 μL of the harvested EVs to be analyzed by the aptamer-conjugated bimetallic MOF. The harvested EVs were diluted 15,000 times and 20 μL of the dilution was used in the assay. We clearly observed that the blue color of the detection solution turned darker with longer harvest times and the absorbance increase was significantly different between different time points (Figure 3.4c). This result supports that our assay can be used to monitor exosome production from cell lines, which could be stimulated to increase or reduce vesicle productions for exosome biogenesis study. The large dilution factor we used for this harvested EV sample illustrates the possibility of direct sampling of the cell culture medium for monitoring of EV production by cells by our assay, avoiding the tedious steps of ultracentrifugation.

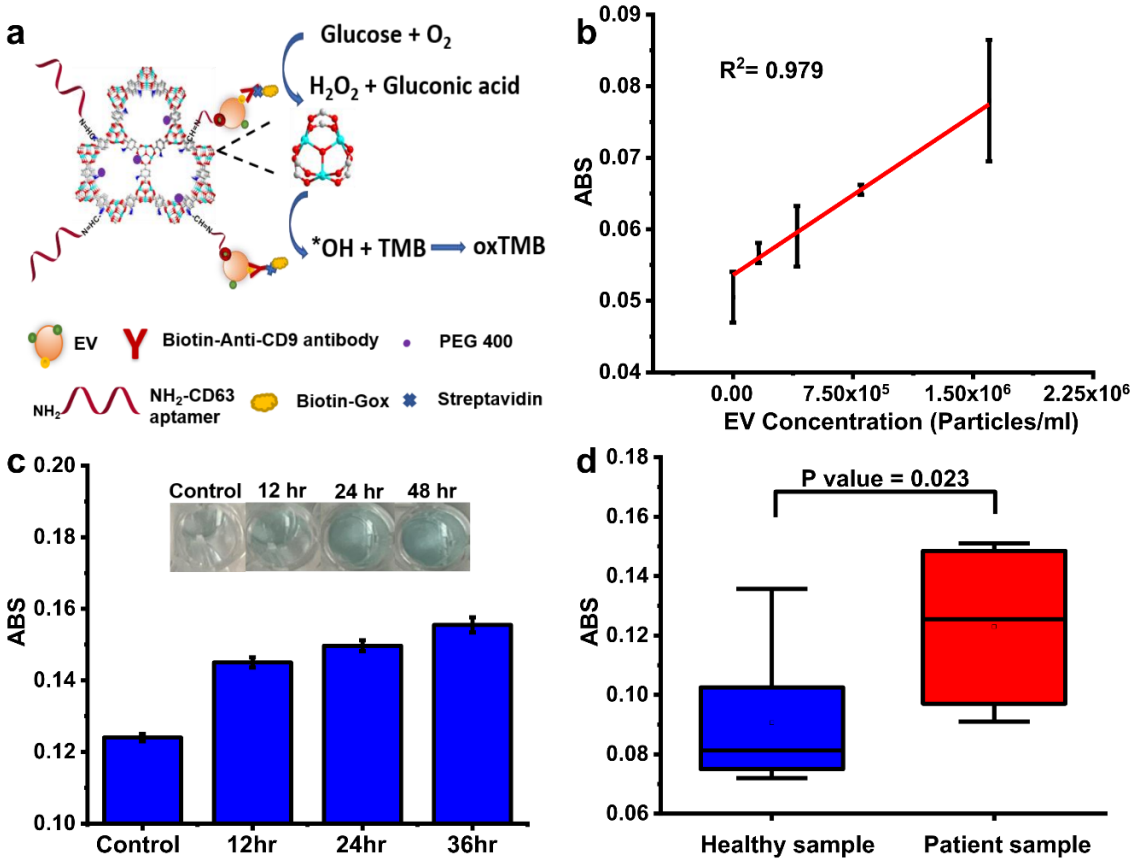

Figure 3.4 *Application of Fe/Co-MIL-88(NH_2) for EV detection. a) Scheme of EV detection facilitated by the cascade reaction between the peroxidase-mimicking Fe/Co-MIL-88(NH_2) and GOx; b) Calibration curve of the assay for detection EVs dispersed in 1× PBS; c) Colorimetric signal resulted from detection of EVs secreted by HeLa cells at various time points; d) Detection of EVs in the sera samples from healthy controls (n=8) and breast cancer patients (n=8). The detection solution contained 0.50 mM TMB, 3.0 mg MOF, and 0.50 mM glucose, in 200 mM NaAc-HAc buffer at pH 4.1.*

Moreover, we detected exosomes in serum samples collected from breast cancer patients and healthy people (n = 8 for each cohort). We found that the exosome concentrations in these clinical samples were much higher than the upper detection limit of our assay, and 10,000× dilution was needed for all samples. This means that we only needed far less than 1 μL serum for each measurement. The exosome concentrations were found significantly higher ($p < 0.05$) in patients' sera samples (Figure 3.4d) than that found

in the samples of healthy controls. The bimetallic MOF can enable sensitive exosome detection in complex biological matrices with ultra-low sample consumption, proving its high potential in clinical applications.

Fe/Co-MIL-88 (NH_2)-Catalyzed Luminol Reaction for Chemiluminescence Signal Generation. HRP mimicking Fe/Co-MIL-88 (NH_2) was used for catalyzing the generation of chemiluminescence in the presence of luminol and H_2O_2. The catalytical ability of activated Fe/Co-MIL-88 (NH_2) and activated Fe-MIL-88 (NH_2) for chemiluminescence generation was compared. Notably, the chemiluminescence signal to background ratio catalyzed by activated Fe/Co-MIL-88 (NH2) are 21 times greater than the Signal to background generated by activated Fe-MIL-88 (NH_2). (Figure 3.5a) This is due to higher peroxidase activity of activated Fe/Co-MIL-88 (NH_2) on luminol- H_2O_2 reaction. The potential CL mechanism could be briefly explained as followed. Under alkaline condition, the luminol and H_2O_2 can be transformed into H_2O- and luminol monoanion (LH-) .Under basic condition, H_2O_2 decomposition on metallic peroxidase mimic surface proceeds to generate •OH and $O_2^{\bullet-}$.[47] Then, LH- reacts with the produced •OH to form luminol radical ($L^{\bullet-}$) and $O_2^{\bullet-}$, Finally, the $L^{\bullet-}$ reacts with $O_2^{\bullet-}$ to generate the excited-state aminophatalate dianion (AP^{2-*}) ,followed by returning to the ground state with light emission. Before comparing activated Fe/Co-MIL-88(NH_2) with HRP, the selection of optimal test conditions was particularly important.[48] In this system, we optimized the concentrations of luminol and H_2O_2 concentration. As shown in Figure S3.11, the optimal concentrations of luminol and H_2O_2 are 0.002 mM and 1 mM. Next, the performance of activated Fe/Co-MIL-88 (NH_2) and HRP for chemiluminescence signal

generation was compared. Activated Fe/Co-MIL-88 (NH_2) outperformed HRP in catalyzing CL emission with 1 mM H_2O2 and 0.002 mM: as low as 0.0044 fM(3σ) of the activated Fe/Co-MIL-88 (NH_2), could be detected, while the limit of detection (LOD) of HRP was only 0.1 nM(3σ) (Figure 3.5b**)**. The superior detectability of Fe/Co-MIL-88 (NH_2) is due to the abundance catalytical sites in the framework as well as the ions releasing at extremely basic conditions. The curves plotting CL intensity vs Fe/Co-MIL-88 (NH_2) concentration all exhibited a hyperbolic shape, showing slower increase in CL within the lower Fe/Co-MIL-88 (NH_2) concentration range. Such a feature agrees with our previous report on using Cu^{2+}-based material for CL production;[49] and may be attributed to the two-step catalytic process of the Co^{2+}-H_2O_2 system and Fe $^{3+}$-H_2O_2 system for ROS specifics generation. In Co^{2+}-H_2O_2 system, first Co^{2+} is oxidized into Co^{3+}, second Co^{3+} is cycled back to Co^{2+} by H_2O_2-mediate reduction, accompanied by production of the highly reactive species, hydroxyl radical, responsible for strong CL emission. In Fe $^{3+}$-H_2O_2 system, first Fe (III) reduces to Fe (II) on MOF. Next, the generated surface Fe (II) is oxidized by with to form •OH and •O. Thus, higher Co^{2+} and Fe^{3+} concentration significantly speeds up the rate-limiting step to attain a comparable rate as the second reaction step, causing more rapid increase in CL with unit increase in MOF concentration. In the following study, activated Fe/Co-MIL-88(NH_2) was employed because of their superior detectability compared to HRP.

Application of Fe/Co-MIL-88(NH_2) for sandwich ELISAs for exosome detection. In this study, exosome immunoassays were developed and their clinical applications to cancer diagnosis were evaluated. The anti-CD9 antibody was adsorbed on the high binding

plate to capture CD9 positive exosome. Next CD63 modified activated Fe/Co-MIL-88 (NH_2) was applied to detect the captured exos0me on plate. Due to the expression specificity of these proteins, CD9-CD63 pair assay is detecting general exosome. (Figure 3.5c) To validate the exosome assay, a standard curve was generated from a serial dilution of the exosome standard using the assay. As shown in Figure 3.5d, with increasing the concentration of exosome, the CL intensity is gradually increased in the range of $1X10^7$ – 5 $X10^8$ particles/ml. The limit of detection (LoD) of the CD9-CD63 assay was calculated at $1X10^7$ particles/mL. Such an LOD is lower than what could be obtained by NTA (108−109 particles/mL) and ELISA (10^{10} particles/mL).[45, 46] The exosome detection assay was further validated for clinical applications in breast cancer diagnosis. Plasma samples from 5 breast cancer patients and healthy people were tested. We observed that exosome concentrations obtained with the CD9-CD63 (Figure 3.5e) assays from 5 breast cancer patient samples were significantly higher than EV concentrations obtained from healthy controls (P-value < 0.05) Our results are consistent with previous study which observed that the level of exosome in the blood is higher in cancer patients than in healthy individuals[50, 51]

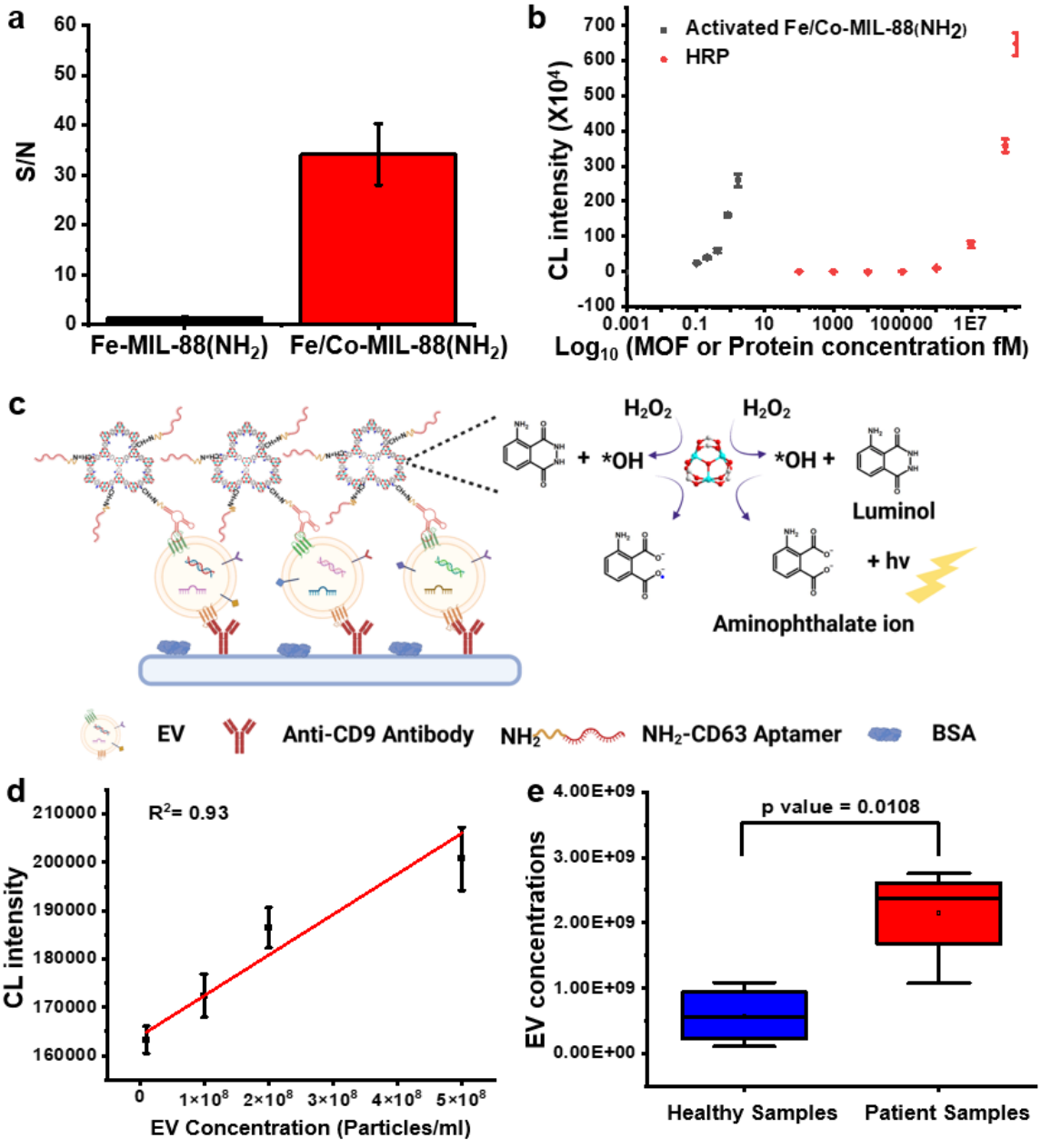
a
S/N
Fe-MIL-88(NH2)
Fe/Co-MIL-88(NH2)
b
Activated Fe/Co-MIL-88(NH2)
HRP
CL intensity (X10^4)
Log10 (MOF or Protein concentration fM)
c
H2O2
H2O2
*OH
*OH +
Luminol
+ hv
Aminophthalate ion
EV
Anti-CD9 Antibody
NH2-CD63 Aptamer
BSA
d
R2= 0.93
CL intensity
EV Concentration (Particles/ml)
e
p value = 0.0108
EV concentrations
Healthy Samples
Patient Samples

Figure 3.5 *Application of activated Fe/Co-MIL-88(NH_2) for chemiluminescence signal generation and sandwich ELISAs. a) Compare chemiluminescence generated by activated Fe-MIL-88(NH_2) and activated Fe/Co-MIL-88(NH_2), MOF concentration= 5ug/ml, Luminol 0.002mM, H_2O_2= 1mM, pH =13; b) The chemiluminescence performance of activated Fe/Co-MIL-88(NH_2) comparing with standard HRP, Activated Fe/Co-MIL-88(NH_2) in Luminol 0.002mM, H_2O_2= 1mM, pH =13, HRP in 1XPBS; c) Detection of EV with Fe/Co-MIL-88(NH_2) based sandwich ELISAs; d) Detection of extracellular vesicle with activated Fe/Co-MIL-88(NH_2) based ELISAs; e) Detection of serum samples from healthy people and patients.*

3.4 Conclusion

In the present work, we report a bimetallic Fe/Co-MIL-88(NH2) with superior peroxidase catalytic activities and good stability, and evaluate its peroxidase-like activity. Because of the abundant active site and synergistic effect between Fe and Co, the Fe/CoIn the present work, we report a bimetallic Fe/Co-MIL-88(NH2) with superior peroxidase catalytic activities and good stability, and evaluate its peroxidase-like activity. Because of the abundant active site and synergistic effect between Fe and Co, the Fe/Co-MIL-88(NH2) exhibits superior catalytic activity to HRP and the monometallic Fe-MIL-88(NH2). It can also enable-MIL-88(NH2) exhibits superior catalytic activity to HRP and the monometallic Fe-MIL-88(NH2). It can also enable sensitive exosome detection while forming a cascade reaction with GOx, demonstrating great potential to be signaling labels in bioassays for detection of biomarkers. We believe that the design of including multiple metals in one MOF structure could produce more MOFs with superior enzyme-like characteristics and expand the collection of nanozymes for broader scopes of applications.[52-54]

Some improvements are still needed to further move forward clinical applications of this peroxidase-like MOF material. For example, the dynamic range is quite narrow in the current format. The intrinsic oxidase activity towards TMB of the bimetallic MOF produces a high background at low target concentrations: with a low target concentration, only a very low amount of GOx could be immobilized on the MOF and generate a very low amount of H_2O_2, being outcompeted by O_2 in the air to produce oxTMB. On the other hand, with a high target concentration, the colorimetric signal would drop significantly, probably because the H_2O_2 concentration is too high and at very close proximity to the

MOF that would destroy the MOF structure and prevent further signal increase. Both factors contribute to a narrow detection dynamic range by the cascade enzymatic reaction scheme. Other signaling strategies and MOF designs could be adopted to improve the detection range in future studies.

Supporting Information

Supporting figures

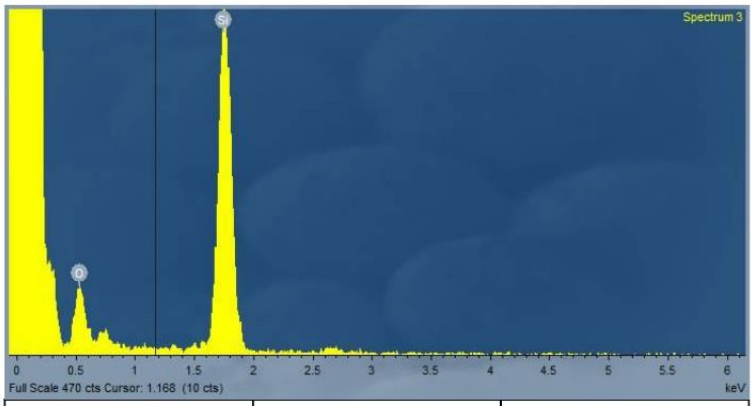

Element	Weight %	Atomics%
Fe	15.15+/- 3.61	7.18
Co	4.98+/- 2.62	2.23

Figure S3.1 *EDS measurement of Fe/Co-MIL-88(NH2).*

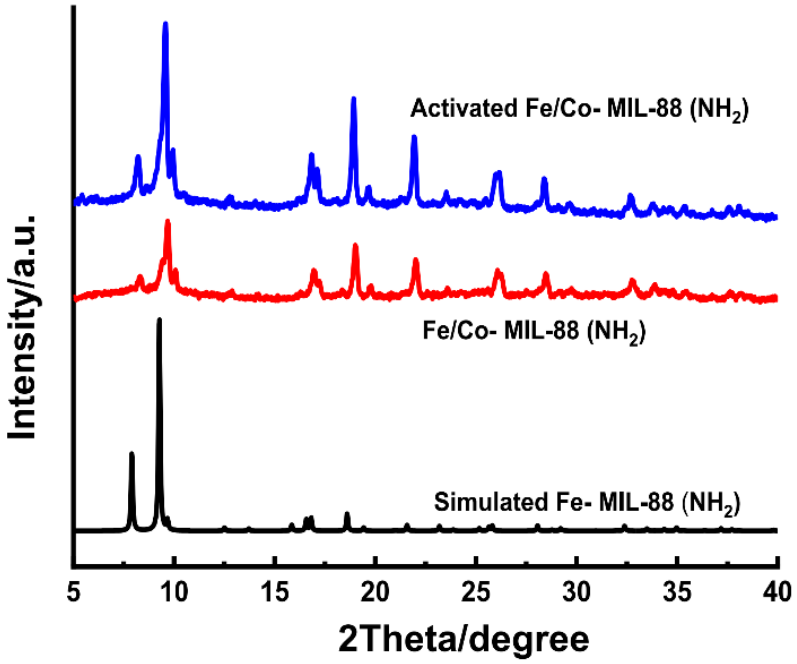

Figure S3.2 *Powder X-ray diffraction patterns for Fe/Co MIL-88(NH_2) before and after activation.*

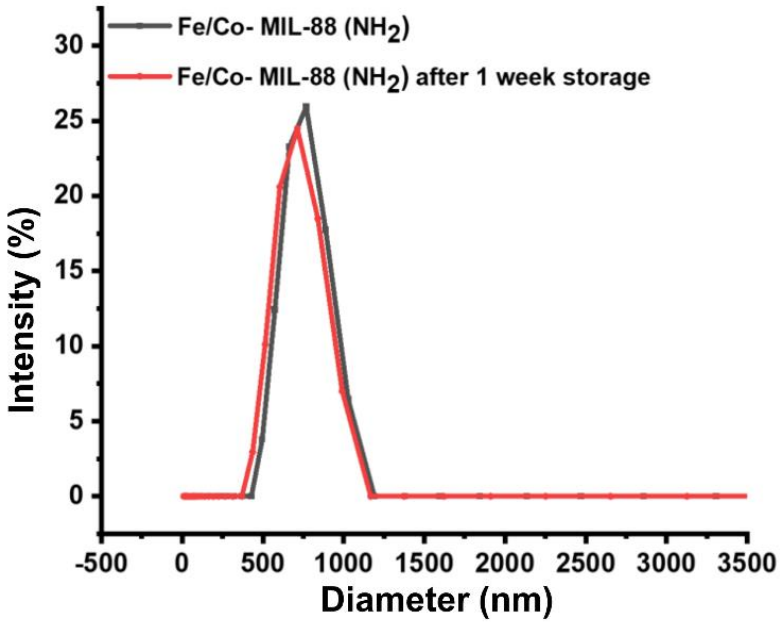

Figure S3.3 *Dynamic Light Scattering results of Fe/Co-MIL-88(NH_2) before and after stored at room temperature for 1 week.*

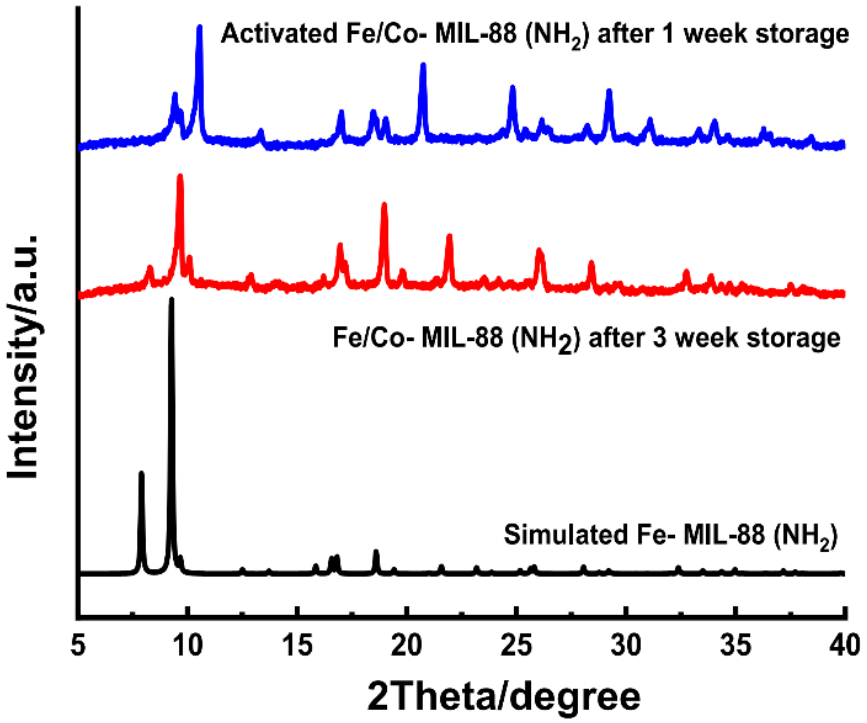

Figure S3.4 *Powder X-ray diffraction results of Fe/Co MIL-88(NH_2) stored at room temperature for 1 and 3 weeks.*

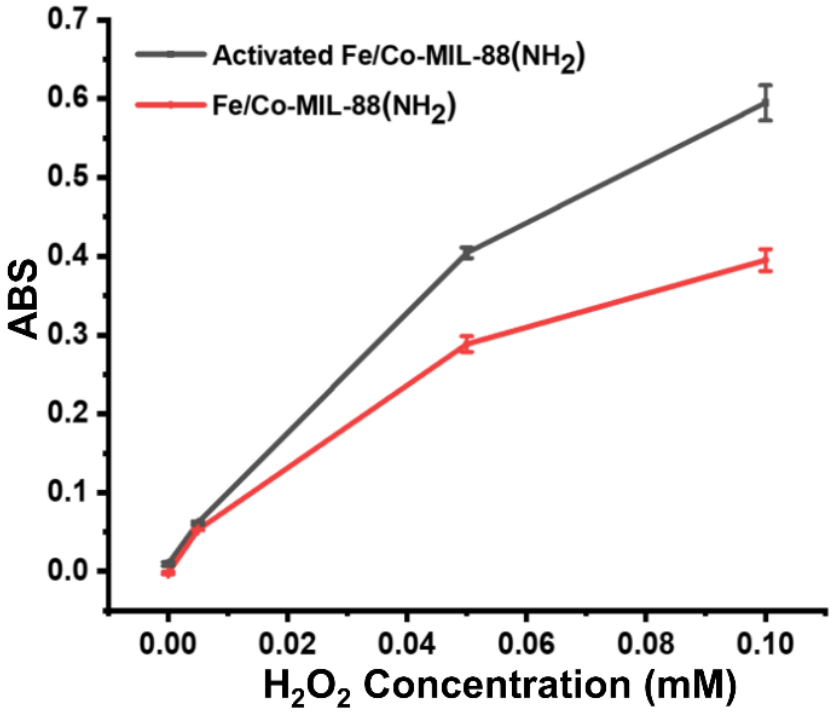

Figure S3.5 *Catalytic ability comparison before and after activation. After activation, more increase of the absorbance signal per unit increase of the H_2O_2 concentration was observed. MOF = 25 µg/ml in 200 mM NaAc-HAc buffer at pH 4.1. Reaction time = 15 min.*

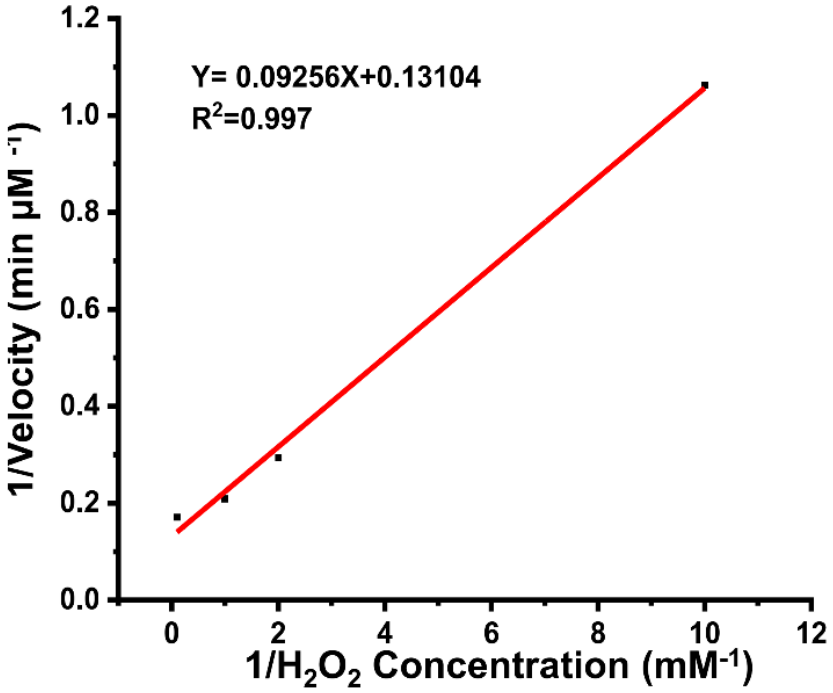

Figure S3.6 *The double reciprocal of Michaelis–Menten fitting curve plotting the initial velocities within the first 15 min against H_2O_2 concentrations, TMB =1 mM, Fe/Co-MIL-88(NH_2) = 50 μg/ml in 200 mM NaAc-HAc buffer at pH 7.4.*

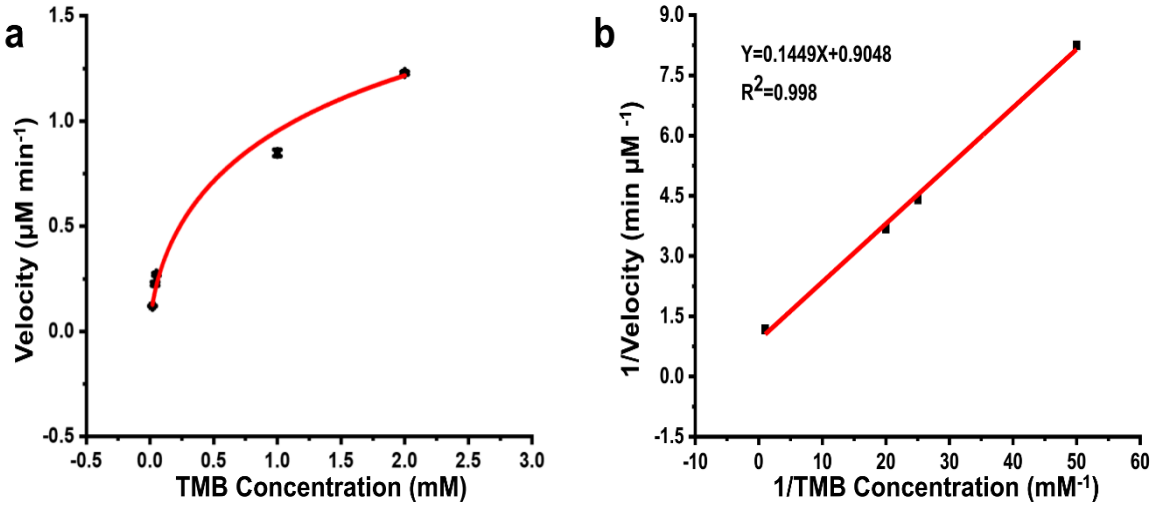

Figure S3.7 *Steady-state kinetics study of Fe/Co-MIL-88(NH_2). a) The Michaelis–Menten curve that plots the initial •OH generation velocities within the first 15 min against TMB concentrations. b) The double reciprocal of Michaelis–Menten fitting curve using data shown in a), H_2O_2 =1 mM, Fe/Co-MIL-88(NH_2) = 25 μg/ml in 200 mM NaAc-HAc buffer at pH 4.1.*

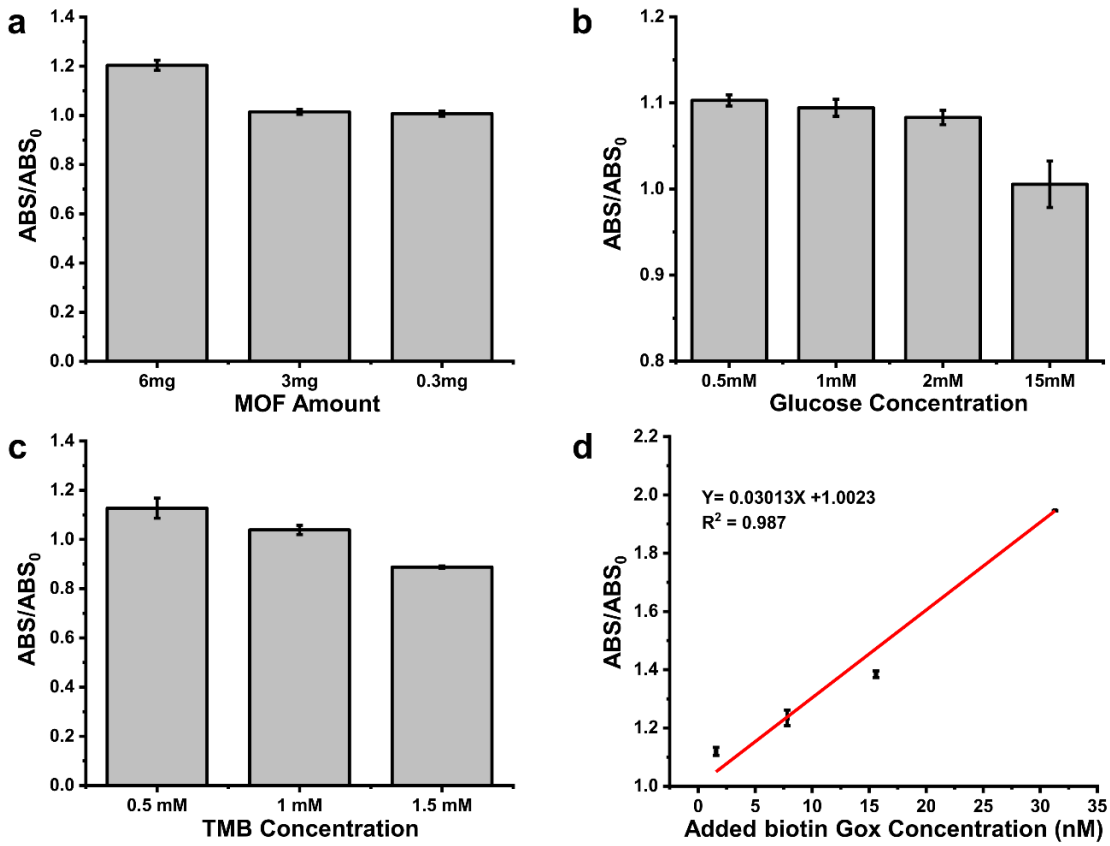

Figure S3.8 *Optimization of the cascade enzymatic reaction in 200 mM NaAc-HAc buffer at pH=4.1. a) Absorbance signal change with the addition of different amount of the MOF while keeping TMB and glucose at 1.0 and 2.0 mM, respectively. b) Absorbance signal change with the addition of different concentrations of glucose, while keeping TMB at 1.0 mM and MOF amount as 3.0 mg per reaction, respectively. c) Absorbance signal change with the addition of different concentrations of TMB, while keeping glucose at 2 mM and MOF amount as 3.0 mg per reaction. d) Detection of biotinylated GOx at the optimized enzyme and substrate conditions: MOF amount = 3.0 mg, TMB = 0.50 mM, Glucose = 0.50 mM. Reaction time = 30min.*

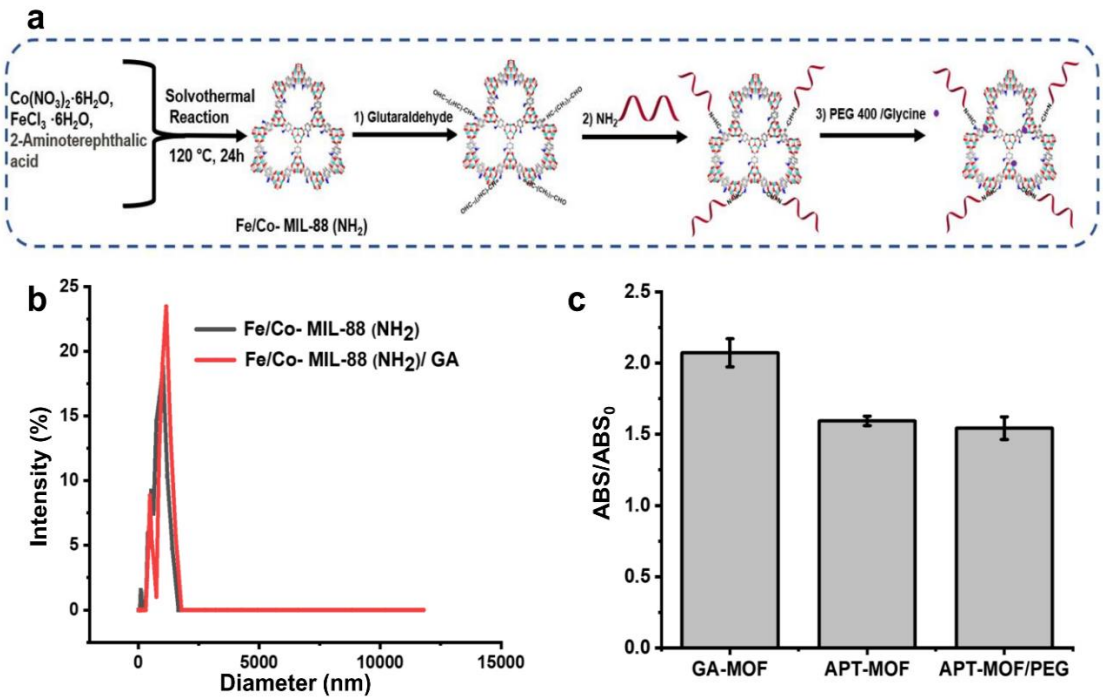

Figure S3.9 *a) Conjugation of Fe/Co-MIL-88(NH_2) with the anti-CD63 aptamer through glutaraldehyde followed by passivation of the surface-active groups with PEG 400 and glycine. b) Dynamic Light Scattering measurement of Fe/Co-MIL-88(NH_2) before and after reaction with glutaraldehyde. c) Peroxidase activity assessment after reaction with glutaraldehyde (GA-MOF), aptamer modification (APT-MOF), and surface passivation (APT-MOF/PEG). TMB = 1 mM, MOF = 0.7 mg/ml, H_2O_2 = 0.5 mM, in 200 mM NaAc-HAc buffer at pH = 4.1. Reaction time = 15 min. Background: H_2O_2 = 0 mM.*

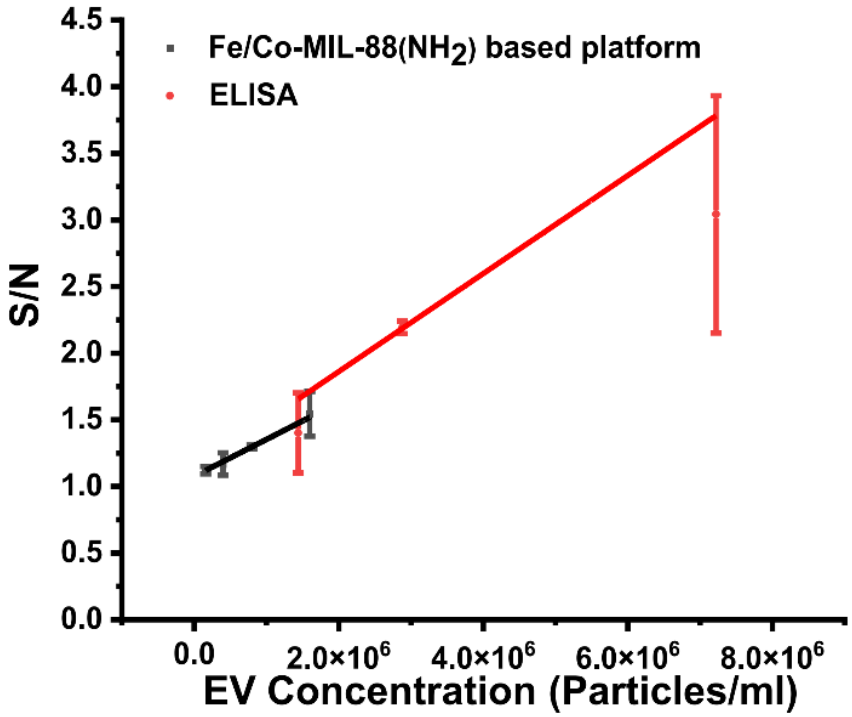

Figure S3.10 *Comparison of standard curves measuring spiked EVs using conventional ELISA vs. the Fe/Co-MIL-88(NH_2) based EV detection platform. The LODs obtained from the ELISA and the Fe/Co-MIL-88(NH_2) based EV detection platform were 4.6 × 10^6 p/mL and 7.8 × 10^4 p/mL, respectively. Anti-CD9 and anti-CD81 were applied as capturing antibodies, anti-CD63 was applied as detection antibodies, and the secondary antibody conjugated with HRP was employed for signal development in the conventional ELISA.*

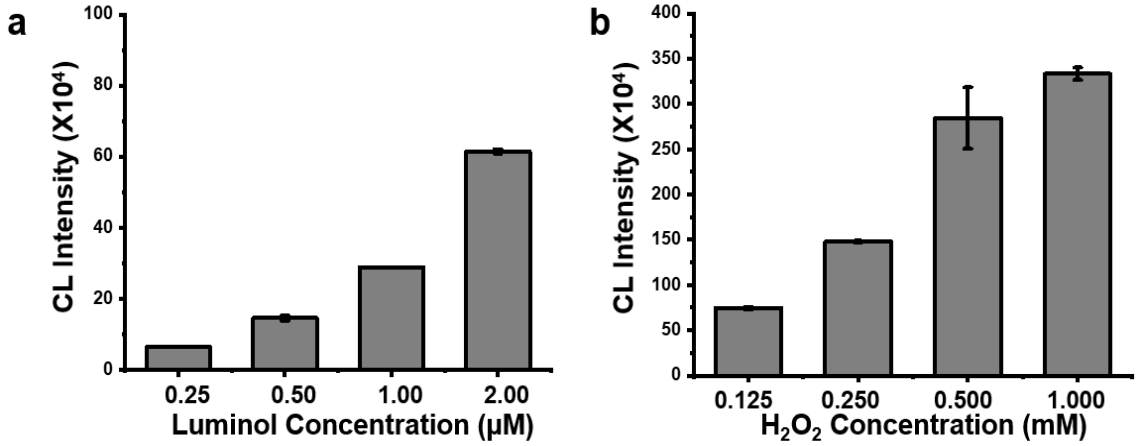

Figure S3.11 *Substrate optimization for chemiluminescence. a) optimization of luminol concentration; b) optimization of H_2O_2 concentration.*

Reference

1. Lu, K., Aung, T., Guo, N., Weichselbaum, R. & Lin, W.J.A.M. Nanoscale metal–organic frameworks for therapeutic, imaging, and sensing applications. **30**, 1707634 (2018).

2. Yang, H. et al. Pore-space-partition-enabled exceptional ethane uptake and ethane-selective ethane–ethylene separation. **142**, 2222-2227 (2020).

3. Hong, A.N. et al. Pore-space partition and optimization for propane-selective high-performance propane/propylene separation. **13**, 52160-52166 (2021).

4. Lu, X.F., Fang, Y., Luan, D. & Lou, X.W.D.J.N.l. Metal–organic frameworks derived functional materials for electrochemical energy storage and conversion: a mini review. **21**, 1555-1565 (2021).

5. Indra, A., Song, T. & Paik, U.J.A.M. Metal organic framework derived materials: progress and prospects for the energy conversion and storage. **30**, 1705146 (2018).

6. Xu, W. et al. Metal–organic frameworks enhance biomimetic cascade catalysis for biosensing. **33**, 2005172 (2021).

7. Rasheed, T., Rizwan, K.J.B. & Bioelectronics Metal-organic frameworks based hybrid nanocomposites as state-of–the-art analytical tools for electrochemical sensing applications. **199**, 113867 (2022).

8. Zhang, X. et al. Advances in organometallic/organic nanozymes and their applications. **429**, 213652 (2021).

9. Ji, S. et al. Matching the kinetics of natural enzymes with a single-atom iron nanozyme. **4**, 407-417 (2021).

10. Wang, S. et al. Enhancing luminol electrochemiluminescence by combined use of cobalt-based metal organic frameworks and silver nanoparticles and its application in ultrasensitive detection of cardiac troponin I. **91**, 3048-3054 (2019).

11. Shao, K. et al. Target-triggered signal-on ratiometric electrochemiluminescence sensing of PSA based on MOF/Au/G-quadruplex. **118**, 160-166 (2018).

12. Wang, Z., Jiang, X., Yuan, R., Chai, Y.J.B. & Bioelectronics N-(aminobutyl)-N-(ethylisoluminol) functionalized Fe-based metal-organic frameworks with intrinsic mimic peroxidase activity for sensitive electrochemiluminescence mucin1 determination. **121**, 250-256 (2018).

13. Zhao, X. et al. Bimetallic Metal–Organic Frameworks: Enhanced Peroxidase-like Activities for the Self-Activated Cascade Reaction. **13**, 36106-36116 (2021).
14. Zhang, Y. et al. Bimetallic molecularly imprinted nanozyme: Dual-mode detection platform. **196**, 113718 (2022).

15. Huang, Y., Ren, J. & Qu, X.J.C.r. Nanozymes: classification, catalytic mechanisms, activity regulation, and applications. **119**, 4357-4412 (2019).

16. Niu, X. et al. Metal–organic framework based nanozymes: promising materials for biochemical analysis. **56**, 11338-11353 (2020).

17. He, L. et al. Ru (III)-based metal–organic gels: intrinsic horseradish and NADH peroxidase-mimicking nanozyme. **11**, 29158-29166 (2019).

18. Wei, Y.-S. et al. A Single-Crystal Open-Capsule Metal–Organic Framework. *J. Am. Chem. Soc.* **141**, 7906-7916 (2019).

19. Jiang, B. et al. Standardized assays for determining the catalytic activity and kinetics of peroxidase-like nanozymes. **13**, 1506-1520 (2018).

20. Liu, B., Vikrant, K., Kim, K.-H., Kumar, V. & Kailasa, S.K.J.E.S.N. Critical role of water stability in metal–organic frameworks and advanced modification strategies for the extension of their applicability. **7**, 1319-1347 (2020).

21. Ma, M. et al. Iron metal–organic frameworks MIL-88B and NH2-MIL-88B for the loading and delivery of the gasotransmitter carbon monoxide. **19**, 6785-6790 (2013).

22. Mo, G. et al. A sensitive electrochemiluminescence biosensor based on metal-organic framework and imprinted polymer for squamous cell carcinoma antigen detection. **310**, 127852 (2020).

23. Pereira, M., Oliveira, L. & Murad, E.J.C.m. Iron oxide catalysts: Fenton and Fentonlike reactions–a review. **47**, 285-302 (2012).

24. Li, J., Chu, D., Dong, H., Baker, D.R. & Jiang, R.J.J.o.t.A.C.S. Boosted oxygen evolution reactivity by igniting double exchange interaction in spinel oxides. **142**, 50-54 (2019).

25. Gao, C., Chen, S., Quan, X., Yu, H. & Zhang, Y.J.J.o.C. Enhanced Fenton-like catalysis by iron-based metal organic frameworks for degradation of organic pollutants. **356**, 125-132 (2017).

26. Yang, X.-j., Xu, X.-m., Xu, J. & Han, Y.-f.J.J.o.t.A.C.S. Iron oxychloride (FeOCl): an efficient Fenton-like catalyst for producing hydroxyl radicals in degradation of organic contaminants. **135**, 16058-16061 (2013).

27. Zhou, W., Gao, J., Zhao, H., Meng, X. & Wu, S.J.E.t. The role of quinone cycle in Fe2+–H2O2 system in the regeneration of Fe2+. **38**, 1887-1896 (2017).

28. Spier, E., Neuenschwander, U. & Hermans, I.J.A.C.I.E. Insights into the Cobalt (II)-Catalyzed Decomposition of Peroxide. **52**, 1581-1585 (2013)

29. Leonard, S. et al. Cobalt-mediated generation of reactive oxygen species and its possible mechanism. **70**, 239-244 (1998).

30. Dong, H., Fan, Y., Zhang, W., Gu, N. & Zhang, Y.J.B.C. Catalytic mechanisms of nanozymes and their applications in biomedicine. **30**, 1273-1296 (2019).

31. Zhou, X. et al. Trimetallic AuPtCo Nanopolyhedrons with Peroxidase-and Catalase-Like Catalytic Activity for Glow-Type Chemiluminescence Bioanalysis. (2021).

32. Lu, W. et al. Synergistic Lewis acid-base sites of ultrathin porous Co3O4 nanosheets with enhanced peroxidase-like activity. **14**, 3514-3522 (2021).

33. Jiang, Z.-J., Cheng, S., Rong, H., Jiang, Z. & Huang, J.J.J.o.M.C.A. General synthesis of MFe 2 O 4/carbon (M= Zn, Mn, Co, Ni) spindles from mixed metal organic frameworks as high performance anodes for lithium ion batteries. **5**, 23641-23650 (2017).

34. McKinlay, A.C. et al. Nitric Oxide Adsorption and Delivery in Flexible MIL-88(Fe) Metal–Organic Frameworks. *Chem. Mater.* **25**, 1592-1599 (2013).

35. Horcajada, P. et al. How Linker's Modification Controls Swelling Properties of Highly Flexible Iron(III) Dicarboxylates MIL-88. *J. Am. Chem. Soc.* **133**, 17839-17847 (2011).

36. Ramsahye, N.A. et al. Impact of the Flexible Character of MIL-88 Iron(III) Dicarboxylates on the Adsorption of n-Alkanes. *Chem. Mater.* **25**, 479-488 (2013).

37. Mondloch, J.E., Karagiaridi, O., Farha, O.K. & Hupp, J.T.J.C. Activation of metal–organic framework materials. **15**, 9258-9264 (2013).

38. Otun, K.O.J.I.C.A. Temperature-controlled activation and characterization of iron-based metal-organic frameworks. **507**, 119563 (2020).

39. He, J., Zhang, Y., Zhang, X. & Huang, Y.J.S.r. Highly efficient Fenton and enzyme-mimetic activities of NH2-MIL-88B (Fe) metal organic framework for methylene blue degradation. **8**, 1-8 (2018).

40. Gao, L. et al. Intrinsic peroxidase-like activity of ferromagnetic nanoparticles. **2**, 577-583 (2007).

41. Fang, C. et al. Co–ferrocene MOF/glucose oxidase as cascade nanozyme for effective tumor therapy. **30**, 1910085 (2020).

42. Wang, D. et al. Self-Assembled Single-Site Nanozyme for Tumor-Specific Amplified Cascade Enzymatic Therapy. **133**, 3038-3044 (2021).

43. Zhang, L. et al. Nature-inspired construction of MOF@ COF nanozyme with active sites in tailored microenvironment and pseudopodia-like surface for enhanced bacterial inhibition. **60**, 3469-3474 (2021).

44. Kalluri, R. & LeBleu, V.S. The biology, function, and biomedical applications of exosomes. *Science* **367**, eaau6977 (2020).

45. Zarovni, N. et al. Integrated isolation and quantitative analysis of exosome shuttled proteins and nucleic acids using immunocapture approaches. **87**, 46-58 (2015).

46. Doldán, X., Fagúndez, P., Cayota, A., Laíz, J. & Tosar, J.P.J.A.c. Electrochemical sandwich immunosensor for determination of exosomes based on surface marker-mediated signal amplification. **88**, 10466-10473 (2016).

47. Li, J., Liu, W., Wu, X. & Gao, X.J.B. Mechanism of pH-switchable peroxidase and catalase-like activities of gold, silver, platinum and palladium. **48**, 37-44 (2015).

48. Carrara, S., Aliprandi, A., Hogan, C.F. & De Cola, L.J.J.o.t.A.C.S. Aggregation-induced electrochemiluminescence of platinum (II) complexes. **139**, 14605-14610 (2017).

49. Jiang, Q., Liu, Y., Wang, L., Adkins, G.B. & Zhong, W.J.A.c. Rapid enrichment and detection of extracellular vesicles enabled by CuS-enclosed microgels. **91**, 15951-15958 (2019).

50. Jakobsen, K.R. et al. Exosomal proteins as potential diagnostic markers in advanced non-small cell lung carcinoma. **4**, 26659 (2015).

51. Silva, J. et al. Analysis of exosome release and its prognostic value in human colorectal cancer. **51**, 409-418 (2012).

52. Wu, J. et al. Nanomaterials with enzyme-like characteristics (nanozymes): next-generation artificial enzymes (II). **48**, 1004-1076 (2019).

53. Wei, H. & Wang, E.J.C.S.R. Nanomaterials with enzyme-like characteristics (nanozymes): next-generation artificial enzymes. **42**, 6060-6093 (2013).

54. Wang, X. et al. eg occupancy as an effective descriptor for the catalytic activity of perovskite oxide-based peroxidase mimics. **10**, 1-8 (2019).

Chapter IV Highly Stable Fe/Co-TPY-MIL-88(NH2) Metal Organic Framework (MOF) for Improved Performance in Sensing Extracellular Vesicle

4.1 Introduction

Multienzyme cascade reaction, consisting at least two consecutive enzyme-catalyzed reactions in one-pot cascade process, offers highly efficient catalytic performance due to high local concentration, efficient mass transfer, and reduced intermediate decomposition compared with a single enzyme reaction.[1-3] Owing to such advantages, multienzyme cascade reaction has been applied as a signal amplification for glucose sensing, [4-6] Acetylcholine sensing, [7] antibody against hepatitis C virus sensing, prostate-specific antigen.[8] In those work enzyme-mimicking nanomaterial was involved in the cascade reaction and archiving sensitive biosensing. Comparing with other nanozyme, such as iron oxide, gold nanoparticles, Metal organic frameworks (MOFs) would be an ideal material for such enzyme cascade system owing to the abundance of active catalytic sites in the framework, high specific surface area, various framework compositions, abundant organic ligands, and good biocompatibility.[9-11] What's more, MOF has also been considered as promising material for biomolecules such as DNA,[12] peptide[13], and exosome[14, 15] separation due to its large surface area and dynamic geometrical shapes. High stability in aqueous solution and high biocompatibility are critical properties for such application. Also, tuning MOF pore size or surface modification is required to selectively and specifically separate biomolecules.

To apply MOF as peroxidase mimics for biomolecule separation and colorimetric signal generation, a bimetallic Fe/Co-MIL-88(NH_2) with superior peroxidase catalytic activities

and good stability was developed in our previous work. However, when the analytes concentration is high, the MOF structure is destroyed quickly, preventing further signal increase. The open metal sites in the MIL-88(NH_2) MOF could be attached by water or analytes and results in destroying of MOF structure. This factor negatively affects our detection platform's performance and limits MOF application for biosensing. Pore space partition strategy which strategy entails the insertion of a pore-partition agent in the framework has been applied for MIL-88(NH_2) series MOF and improving the stability and performance of MOF for gas separation.[16, 17] In this work, pore partition agent, 2,4,6-tri(4-pyridinyl) -1- pyridine (TPY), is introduced to MIL-88 MOF to form Fe/Co-TPY-MIL-88(NH_2) MOF. With more coordination bonds forming between the open metal sites and ligand, the stability of MOF is expected to be improved in aqueous condition.

Bimetallic MOF Fe/Co-MIL-88(NH_2) was developed and showed high enzyme activity. However, the oxidase activity of Fe/Co-MIL-88(NH_2) towards TMB dye and limited stability at high analytes concentrations results in high background and signal dropping at high analytes concentrations. Thus Fe/Co-MIL-88(NH_2)'s application in EV enrichment as well as formation of cascade enzyme reaction was limited. Herein, Fe/Co-TPY-MIL-88(NH_2) MOF with TPY blocking the open metal sites is developed. The Fe/Co-TPY-MIL-88(NH_2) shows high peroxidase-like activity and superior stability in aqueous solutions. In addition, instead of using TMB, a chemiluminescent signaling strategy was investigated. Fe/Co-TPY-MIL-88(NH2) act as the peroxidase-mimic and work together with glucose oxidase (GOx) in the cascade enzymatic reactions to generate chemiluminescence by inputting glucose. The MOF/chemiluminescence reaction system exhibited a lower

background than the MOF/colorimetric reaction system. The lower background enabled the platform acquire the two orders of magnitude lower limit of detection. The superior stability realized the detection of EV at high concentrations. Lastly, the platform was applied for clinical samples detection, proving the feasibility of the peroxidase-mimicking bimetallic TPY-MOFs being promising tools in liquid biopsy.

4.2 Experimental Section

Materials. Ferric chloride, 6-hydrate ($FeCl_3 \cdot 6H_2O$, 98.1%) was acquired from J. T. Baker (Phillipsburg, NJ). Sodium chloride, potassium phosphate dibasic salt (anhydrous), acetic acid, N, N-dimethylformamide (DMF), and cobalt (II) nitrate hexahydrate ($Co(NO_3)_2 \cdot 6H_2O$, 99%) were purchased from Fisher Scientific (Waltham, MA). 2-Aminoterephthalic acid ($H_2(NH_2)BDC$), TMB (3,3', 5,5"-tetramethylbenzidine), polyethylene glycol 400, potassium chloride, glycine (for electrophoresis, ≥99%) and glutaraldehyde solution were from Sigma-Aldrich (Saint Louis, MI). 2,4,6-tri(4-pyridinyl) -1- pyridine (TPY) was purchased from ITC. Ethanol (EtOH, Anhydrous) was from KOPTEC. The amino group modified CD63 aptamer was produced by IDT, Inc. (Coralville, IA). The mouse anti-human CD9 (Clone MM2/57) and HRP were obtained from Sino Biological (Beijing, China) and Cell Signaling Technology (Danvers, MA), respectively. Streptavidin was purchased from Thermo Fisher Scientific (Waltham, MA). All chemicals were at the analytical reagent grade and used without further purification. Ultrapure water with electric resistance > 18.2 MΩ was produced by the Millipore Milli-Q water purification system (Billerica, MA).

Synthesis and activation of Fe/Co-TPY-MIL-88(NH_2). The MOF materials were prepared via a solvothermal method. In a typical approach for the production of the bimetallic Fe/Co-TPY- MIL-88(NH_2), 0.082 g $FeCl_3 \cdot 6H_2O$, 0.090 g $Co(NO_3)_2 \cdot 6H_2O$, 2,4,6-tri(4-pyridinyl) -1- pyridine and 0.053 g $H_2(NH_2)BDC$ were dissolved in 3.181 g DMF in a 23 mL glass bottle, stirred for 40 min, and then heated in 120 °C for 24 hours. After cooling to room temperature, the brown-color crystal Fe/Co-TPY-MIL-88(NH_2) was

washed with DMF, collected by centrifugation, and dried at room temperature. MOF crystals were washed twice with ethanol at 60 °C or room temperature and then dried by vacuum to remove the residual DMF that may impede the subsequent enzyme activity measurement and sensing performance.

Powder X-ray Diffraction (PXRD) Characterization. The phase purity of Fe/Co-TPY- MIL-88(NH_2) was examined by powder X-ray diffraction on a PANalytical Empyrean Series 2 diffractometer operated at 45 kV and 40 mA (Cu Kα radiation, λ = 1.5418 Å). The data collection was performed at room temperature from 5° to 40° with a step size of ~0.026°. The simulated Fe/Co-TPY- MIL-88(NH_2) powder pattern was obtained from the Fe-TPY-MIL-88(NH_2) single crystal data.

Peroxidase-like activity evaluation of Fe/Co-TPY-MIL-88(NH_2) The peroxidase-like activity of the two MOF materials was evaluated using the reaction between H_2O_2 and 3,3′,5,5′-tetramethylbenzidine (TMB). In brief, 50 μg/mL MOF, 1 mM TMB, and H_2O_2 at various concentrations (0, 0.005, 0.05, 0.1, 0.5 and 1 mM) were added to 0.4 mL of 200 mM NaAc-HAc buffer (pH 4.1). The mixture was incubated at 37° C for 15 min, and the visible light absorbance at 652 nm of the TMB oxidation product, i.e., oxTMB, was read in the synergy HT microplate reader.

Enzyme Kinetics Analysis of activated Fe/Co-TPY-MIL-88(NH_2). The steady-state kinetics assays were performed as follows. The activated Fe/Co-MIL-88(NH_2) at the concentration of 50 μg/ml in 100 μL of 200 mM NaAc-HAc buffer (pH 4.1) was incubated with 1.0 mM TMB and H_2O_2 at various concentrations (0, 0.05, 0.1, 0.5, 1.0, and 10 mM) at 37°C. A time-course mode was used to monitor the absorbance change at 652 nm with

a 10 s interval for 15 min in the synergy HT microplate reader. The Beer-Lambert law was used to convert the absorbance to oxTMB concentration using the molar absorptivity at 652 nm of oxTMB (39,000 $M^{-1} \cdot cm^{-1}$)[18] and the optical length of 0.233 cm of the 96 well plates. The slope of the concentration change within the first 15 min period was then calculated to represent the initial velocity (V).

Preparation of Fe/Co-MIL-88(NH_2)/Aptamer Bioconjugate. Aptamer conjugation started by dispersing 35 mg Fe/Co-TPY-MIL-88(NH_2) in 20 ml 1× PBS and adding 100 µl glutaraldehyde. After stirring the solution for 2 hours, the solid was centrifuged, washed with 1× PBS 2 times, and dispersed in 2 ml 1× PBS. Next, ten µL of 0.1mM aptamer was added to the mixture, and the solution was put on a rotating plate and shaken overnight. The Fe/Co-MIL-88(NH_2)/ aptamer conjugate was then collected by centrifugation (20,000 *g*, 3 min) and redispersed in 2 ml 0.1 M glycine buffer containing 32mM PEG(NH_2) for 1 hour to passivate the MOF surface.

Detection of EV relying on the HRP-mimicking activity of Fe/Co-TPY-MIL-88(NH_2). Twenty µl of the EV sample was mixed with 170 µl of the Fe/Co-TPY- MIL-88(NH2)/aptamer bioconjugate at 17.5 mg/mL and 10 µl of the biotin-anti-CD9 antibody (or biotin-anti-HER2 antibody) solution at 0.10 mg/ml. The mixture was shaken at room temperature for 3 hrs. The Fe/Co-MIL-88(NH2)/aptamer -EV-anti-CD9 antibody was centrifuged down (20,000 g, 3 min) and resuspended in 100 µl of the streptavidin solution at 17 µg/ml. After 1-hour incubation, the product was centrifuged down (20,000g, 3 min), washed with 1×PBS once, and mixed with 100 µl biotin-GOx at 0.013 mg/ml. After two washes with 1×PBS, the final product was resuspended in 1× PBS, 25 µl of which was

mixed with 25 µl luminol (0.032 mM), 25 µl glucose (1 mM) and was tested in the Promega GloMax Multiplus Plate Reader.

4.3 Results and Discussion

Design and characterization of bimetallic Fe/Co-TPY-MIL-88(NH_2). In the framework of Fe/Co-MIL-88(NH_2), there are unsaturated, open metal sites which could be attacked guest such as water, hydroxide and biomolecules in the aqueous solutions resulting in structural destroy of MOF. It has been reported that with insertion of second ligand could form more metal-ligan bond and blocking the open metal sites thus improving the stability of MOF.[19-21] To enhance stability of MOF in biological buffers and enable CL-based detection from cascade reactions, we proposed to use the pore space partition strategy in MOF fabrication. The strategy entails the insertion of a pore-partition agent in the Fe/Co-MIL-88(NH_2) framework. It utilizes the symmetry and size matching between the agent, the geometrical pattern of framework coordination sites, and the dimension of channels.(Figure S 4.1) We hypothesized that the stability of Fe/Co-MIL-88(NH_2) will be improved due to the formation of coordination bonds between the open metal sites and pore-partition agent.[22] 2,4,6-tri(4-pyridinyl) -1- pyridine (TPY) which is a planar tritopic ligand with C3 symmetry is selected as the pore-partition agent to occupy all the open metal sites simultaneously. In Fe/Co-MIL-88(NH_2), the unsaturated, open iron sites could form three metal-ligand bonds from three different trinuclear on each layer along the ab plane. Such three metal-ligand bonds are in the manner of C3 symmetry and point to the center of the hexagonal channel. Thus, a planar tritopic ligand with C3 symmetry is ideal to fit such geometric features.

Bimetallic Fe/Co-TPY-MIL-88(NH_2) was synthesized by the solvothermal method, as described in the Experimental Section. Fe(III) and Co(II) can coordinate with the carboxyl

groups on the NH_2BDC^{2-} ligands, forming the trinuclear transition metal (TM) clusters (TM = Fe and Co). In addition, each TPY ligand coordinates with the three metal ions by its three pyridyl ends, giving a rigid framework. (Figure 4.1a) Transmission microscopy (TEM) revealed that the synthesized Fe/Co-TPY-MIL-88(NH_2) MOF exhibited a uniform fat hexagonal dipyramid morphology with a lateral length of about 500 – 800 nm and an average diameter of 300 nm. (Figure 4.1b). Dynamic light scattering (DLS) measurement showed that the average hydrodynamic diameter of the Fe/Co-MIL-88(NH_2) was around 2000 nm. (Figure 4.1c). The surface properties and shape of the non-spherical MOF particles could affect the diffusion coefficient of MOF, thus causing the hydrodynamic size of synthesized Fe/Co-TPY-MIL-88(NH_2) to be larger than the size observed under TEM. PXRD was also performed to characterize the crystal structure. The peaks of the Fe/Co-TPY-MIL-88(NH_2) matched well with those of the simulated Fe-TPY-MIL-88(NH_2) spectrum, which confirmed that Fe/Co-TPY-MIL-88(NH_2) shared the same tocology with Fe -TPY-MIL-88(NH_2), implying that TPY may successfully participate in constructing the framework (Figure 4.1d). Furthermore, we carried out EDS line scanning (Figure S4.2) and confirmed the coexistence of Fe (0.70 keV) and Co (0.77 keV) in the Fe/Co-TPY-MIL-88(NH_2) framework. The atomic% of Fe and Co was found to be 1.65 % and 1.36 %, respectively, and the mole ratio of the two metals was 1:1 when added to the synthesis solution.

The as-synthesized Fe/Co-TPY-MIL-88(NH_2) was initially distributed in DMF, the organic solvent used for synthesis. To improve the permanent porosity and increase the surface area of the MOF, all of the MOF materials used in the following assays were treated

by hot ethanol and dried in vacuum. And the processed was called activation. The size distribution profile and the PXRD spectrum of the MOF were highly similar before and after activation (**Figure S4.3**), confirming that activation did not break or alter the coordination framework. Notably, the resultant MOF was very stable during storage in different conditions: the DSL (**Figure S4.4**) result of Fe/Co-TPY-MIL-88(NH_2) stored for 1 week at room temperature was the same as the freshly synthesized sample.

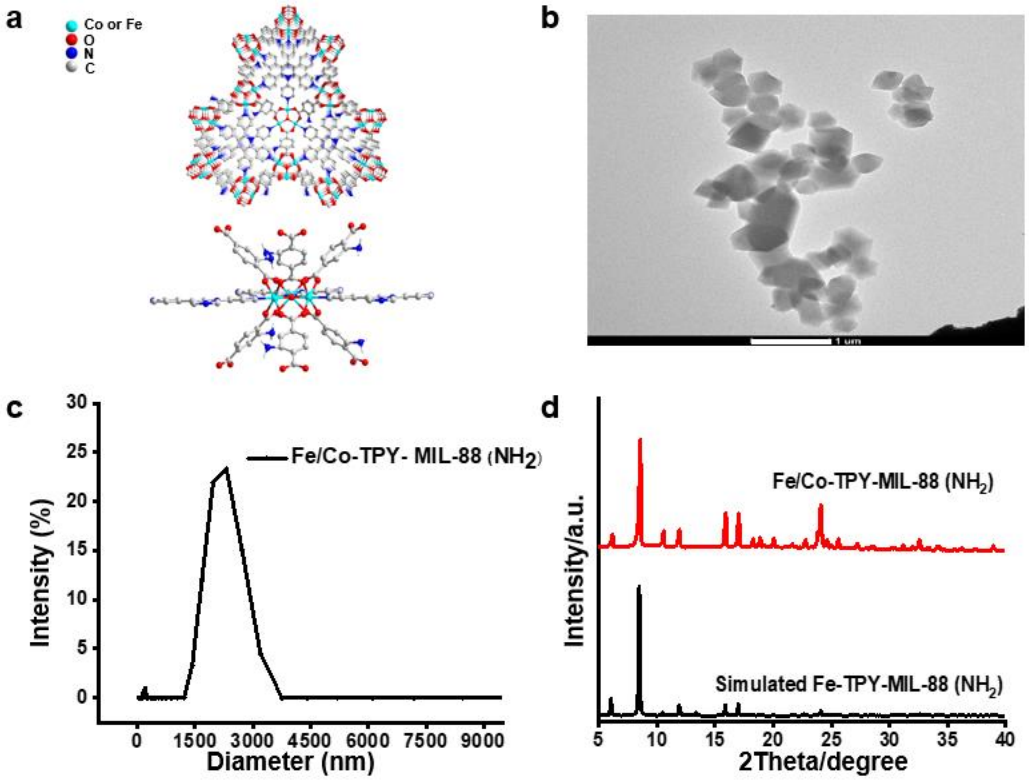

Figure 4.1 *MOF characterization. a) Structure schematic diagram and b) TEM image of Fe/Co-TPY-MIL-88(NH2); c) DSL of Fe/Co-TPY-MIL-88(NH2) and d) powder XRD results for simulated Fe- TPY-MIL-88(NH2) and synthesized Fe/Co-TPY-MIL-88(NH2).*

Evaluation Peroxidase-like Activity of Fe/Co-TPY-MIL-88(NH_2). We firstly evaluated the peroxidase-like activities of Fe/Co-TPY-MIL-88(NH_2) MOF using the model reaction, i.e., the oxidation of the colorless TMB into the blue oxTMB by H_2O_2 which is also the

gold standard assay in the field(Figure 4.2.a)**.**[18] As seen from Figure S4.5**,** the visible light absorption value at 652 nm for oxTMB was 0.41 when mixing 50 μg/mL Fe/Co-TPY-MIL-88(NH_2) with 1.0 mM H_2O_2 and 1.0 mM TMB in 200 mM NaAc-HAc buffer at pH 4.1. In contrast, the absorbance value was close 0 with only the MOF and H_2O_2, or was 0.075 with only MOF and TMB. These results proved that the Fe/Co-TPY-MIL-88(NH_2) could act like a peroxidase to catalyze the decomposition of H_2O_2 and exhibit a low oxidase-like activity. Still, the activity was ~ 6.0 folds smaller than peroxidase-like activity. Low oxidase-like activity has also been reported in other Fe-based MOF materials.[23] We carried out steady-state kinetic analysis to get a more detailed assessment of the catalytic capability of the bimetallic TPY-MOF. The absorbance change at 652 nm was monitored with the MOF at a fixed concentration reacting with varying TMB or H_2O_2 concentrations. The initial production rate (V in $\mu M.min^{-1}$) of oxTMB within the first 15-min of the reaction window was plotted against the H_2O_2 concentrations ([S]) to yield the Michaelis−Menten curve (Figure 4.2b). Rearranging Figure 4.2b to the Lineweaver-Burk plot (Figure S4.6) can attain the Michaelis constant (K_m) and maximum reaction velocity (V_{max}) from the slope and Y-intercept of this linear regression curve: $[1/V = (K_m/V_{max}) \times (1/[S]) + 1/V_{max}]$. The catalytic constant (k_{cat}) can be obtained by dividing the V_{max} by the molar concentration of the "enzyme," the bimetallic Fe/Co-TPY-MIL-88(NH_2), which was calculated by counting the number of individual crystals dispersed in a solution of 10 μL under an optical microscope. The K_m and k_{cat} against the other substrate, TMB, were also measured (Figure S4.7). K_m indicates the binding affinity between the substrate and the enzyme, a smaller value representing a higher affinity. A high value of k_{cat} corresponds to

a fast signal generation speed achievable per unit concentration of the enzyme. As shown in Figure 4.3.c, a K_m of 0.69 mM was found for Fe/Co-TPY-MIL-88(NH_2) to H_2O_2, close to that of Fe/Co-MIL-88(NH_2). While the K_m of Fe/Co-TPY-MIL-88(NH_2) was smaller than the K_m of Fe/Co-MIL-88(NH_2). These results show that blocking the open metal sites by ligand does not affect the accessibility of H_2O_2 to MOF, and the affinity of TMB to MOF was negatively affected. In addition, the k_{cat} of Fe/Co-TPY-MIL-88(NH_2) measured with varying H_2O_2 concentrations were $5.25 \times 10^6\ s^{-1}$, much larger than those of Fe/Co-MIL-88(NH_2). Similarly, the k_{cat} values related to TMB were also more optimal. The high enzymatic activity could be due to the more active metal of Co also included in the Fe/Co-TPY-MIL-88(NH_2). The EDS scanning spectra results proved that the Fe to Co ratio was close to 1:1 while the Fe: Co ratio in Fe/Co-MIL-88(NH_2) framework was close to 3:1.

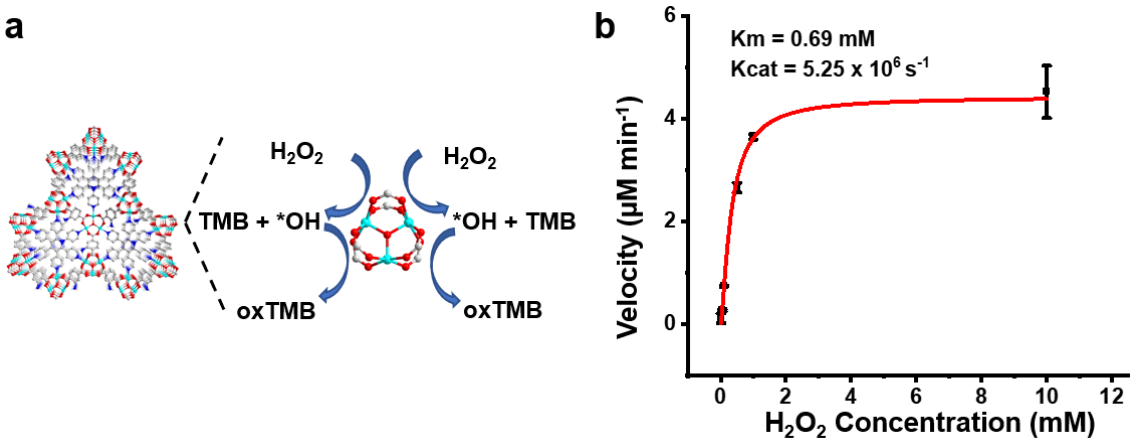

c

Enzyme Mimicking MOF	Substrate	K_m [mM]	K_{cat} [S^{-1}]
Fe/Co--MIL-88 (NH_2)	TMB	0.160	$1.1*10^4$
	H_2O_2	0.710	$3.8*10^4$
Fe/Co-TPY-MIL-88 (NH_2)	TMB	0.627	$2.35*10^6$
	H_2O_2	0.697	$5.25*10^6$

Figure 4.2 *Peroxidase-like activity of Fe/Co-MIL-88(NH_2). a) Schematic illustration of the reaction between TMB and H_2O_2 catalyzed by MOF; b) Plotting the initial reaction velocity calculated from the absorbance change against the corresponding H_2O_2 concentrations. 1.0 mM TMB, 50 μg/mL Fe/Co-TPY-MIL-88(NH_2), and 0.005 – 10 mM H_2O_2. All reactions were in 200 mM NaAc-Hac buffer at pH 4.1; c) Comparison of the catalytic parameters of Fe/Co-MIL-88 (NH_2) and Fe/Co-TPY-MIL-88 (NH_2).*

Bimetallic Fe/Co-TPY- MIL-88 (NH_2) as HRP-mimic for signal generation via a cascade enzymatic reaction. In our previous work, Gox coupled peroxidase-mimicking Fe/Co-MIL-88(NH_2) was applied for colorimetric signal generation for biosensing. However, the intrinsic oxidase-like activity of Fe/Co-MIL-88(NH_2) causes a high background signal by oxidizing TMB directly without hydroxyl radical. In order to solve this problem, we propose to apply chemiluminescence signaling strategy which requires reactive radical to initiate the signal generation. The working principle of CL signaling approach based on peroxidase-mimicking Fe/Co-TPY-MIL-88(NH_2) coupled GOx

cascade reaction is illustrated in **(**Figure 4.3a**)** GOx catalyzes the reaction of glucose and O_2 to produce H_2O_2 and gluconic acid. Then, Fe/Co-TPY-MIL-88(NH_2) with peroxidase-mimic activity catalyzes the decomposition of H_2O_2 to produce some reactive intermediates, such as OH•, $O^{2\bullet-}$, or $^1O_2$, which may react with luminol to generate CL.[24] The chemiluminescence signaling generation catalyzed by MOF is evaluated by the catalytic oxidation reaction with the substrate luminol and the oxidant H_2O_2. As indicated in Figure S4.8, Fe/Co-TPY-MIL-88(NH_2) can catalyze the luminol/ H_2O_2 reaction to produce strong CL signals (which is similar to HRP) when mixing 50 μg/mL Fe/Co-TPY-MIL-88(NH_2) with 1.0 mM H_2O_2 and 0.002mM luminol in 10 mM Borate buffer at pH 10. In contrast, the CL signal was ~ 4 orders of magnitude folds lower in the luminol/ H_2O_2 or luminol/ Fe/Co-TPY-MIL-88(NH_2) systems, which proves that H_2O_2 and Fe/Co-TPY-MIL-88(NH_2) are essential to the oxidation of luminol. The results demonstrate that Fe/Co-TPY-MIL-88(NH_2) possesses peroxidase-like activity to generate CL signals by catalyzing the luminol/ H_2O_2 reaction. In addition, the background was negligible in comparison with TMB/H_2O_2 reaction system. Thus, Fe/Co-TPY-MIL-88(NH_2) catalyzed luminol/ H_2O_2 reaction was potential to apply as a signaling strategy. Several parameters affecting the CL signal intensity of the Fe/Co-TPY-MIL-88(NH_2)/luminol/ H_2O_2 system were investigated to optimize the reaction, including the pH and the luminol concentration. When mixing 50 μg/mL Fe/Co-TPY- MIL-88(NH_2) with 1.0 mM H_2O_2 and 0.002mM luminol, the signal-to-noise ratio (S/N) first increases as the pH value is changed from 5 to 10, owing to the alkaline-promoted luminol/ H_2O_2 CL reaction. In addition, at higher pH the framework is more likely to be attached and release cobalt and iron metal ions due to the strong affinity

between metal cations and hydroxide, accelerating CL signal generation. The S/N decreases rapidly when the pH value is higher than 11 due to the high background signal of luminol at very basic conditions (Figure 4.3b). Figure. S4.9 showed the effect of luminol concentration within 0.004 - 0.16mM. The S/N increases as the luminol concentration increase from 0.004 to 0.032 mM and then rapidly decreases for concentrations larger than 0.032 mM. Thus, the luminol concentration was set at 0.032mM in the following experiments. Since Fe/Co-TPY-MIL-88(NH_2) catalyzed luminol/ H_2O_2 reaction performed better at basic conditions, which could be extreme for the natural enzyme. It's critical to examine the activity of GOx at basic conditions. The glucose oxidase activity was evaluated by benzoquinone. Benzoquinone can replace O_2 as an electron acceptor in the oxidation of d-glucose-catalyzed GOx. This reaction will generate hydroquinone which has an absorbance peak at 289nm. **(**Molar absorptivity (εHQ = 2600 L·mol−1·cm−1 at λmax, HQ = 289 nm**)**[25, 26] The Gox activity at pH = 5,7,9,10,11,12 was measured. The absorbance, which indicates hydroquinone generation, was monitored for the first 1 minutes, with 0.025%(w/v) benzoquinone, 0.5 M Glucose, 0.00375mg/ml Gox. Condition pH 5 gave the highest velocity. The Gox activity slowly decreased as the pH increased from 5 to 10. The velocity dropped 42% at pH =11. The velocity was close to zero at pH 12. And PH 10 was selected as the optimal condition for cascade reaction from the overlap graph of two kinetic curve. (Figure 4.3.b).

The peroxidase-mimicking Fe/Co-TPY-MIL-88 (NH_2) coupled GOx for CL signal generation via a cascade enzymatic reaction was verified. The CL signal was monitored for 2 minutes when mixing 25 μg/mL Fe/Co-TPY-MIL-88(NH_2) with 0.0025mg/ml GOx,

1.0 mM glucose, and 0.032mM luminol in 10 mM Borate buffer at pH 10. Figure 4.3.c showed that the CL signal gradually increased as time progressed. In contrast, there were almost no CL signals in either the MOF/luminol/GOx or MOF/luminol/ glucose systems. There is a little peak in the presence of glucose/luminol/GOx due to oxidation of luminol by generated H_2O_2. These phenomena verified Fe/Co-TPY- MIL-88 (NH_2) coupled GOx for CL signal generation via a cascade enzymatic reaction. The CL kinetic behavior of Fe/Co-TPY- MIL-88 (NH_2) /GOx/glucose/luminol system at pH 9,10,11,12 is further investigated by mixing 25 µg/mL MOF, 0.25mg/ml, 1mM glucose and 0.0032mM luminol**.** The kinetic curves obtained under the different pH conditions are shown in Figure S4.10a. The kinetic curves show that only pH 10 produces an intensive CL emission with long flat periods, while all other pH CL systems present a much faster-decay CL emission. The CL emission produced by the MOF/GOx/glucose/luminol system can last over 30 minutes. (Figure S4.10b) The possible explanation for the intensive, long flat CL signal at pH 10 is at a relatively mild condition; the metal ions were slowly released, thus inducing an intensive, long flat signal. However, at pH 11-12, the metal ions were quickly released and thus inducing shark peak signals. MOF constructed from high-valent metal ions and carboxylate-based ligands display lability toward basic conditions due to the strong affinity between metal ions and hydroxide.[27] We examined the ion releasing by ICP-OES. 20 mg MOF was suspended in 9.785 ml of 1mM glucose, 0.032mM Luminol, 0.25mg GOx at pH 10 for 120 seconds. 0.0139mg cobalt ions and 0.0328mg iron ions were released to the supernatant. (Table S4.1) In addition, the inhibition of GOx activity under harsh conditions results in a weaker signal than the signal at pH 10. At pH 9, the kinetic curve exhibits a

flat-type signal. But the signal is weaker in comparison with the signal at pH 10. Strong and long-lasting emission is favorable for accurate and sensitive CL analysis.[28, 29] Thus, pH 10 is selected as the optimal condition for MOF coupled GOx cascade reaction. Lastly, we spiked the Gox with different concentrations into MOF/ glucose/luminol solution at pH 10. And the lowest GOx concentration that the system could detect was 0.15nM using 0.25µg MOF**,** 1mM glucose, and 0.032mM luminol. (Figure S4.11) The limit of detection of GOx in the CL system was lower than 0.17nM GOx, which can be detected in 3.0 mg MOF, 0.50 mM glucose, and 0.50 mM TMB system.

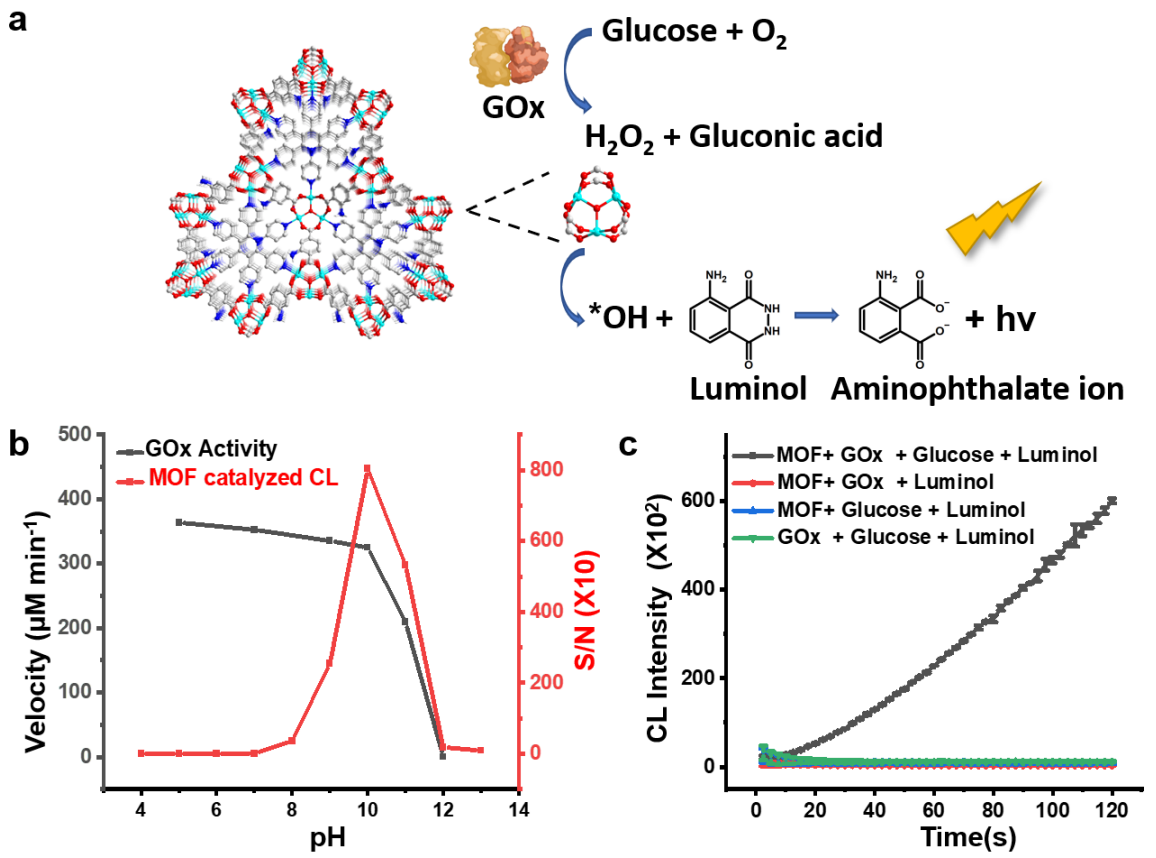

Figure 4.3 *a) Schematic illustration of Fe/Co-TPY-MIL-88 (NH_2) as HRP-mimic coupled GOx cascade enzymatic reaction for chemiluminescence signal generation; b) Effects of pH on the luminol/H_2O_2/ Fe/Co-TPY-MIL-88 (NH_2) chemiluminescence system : 0.002 mM luminol, 1 mM H_2O_2, 50 μg/mL MOF in acetate buffer (pH 4.0 , 10mM), acetate buffer (pH 5.0, 10mM), phosphate buffer (pH 6.0, 10mM), phosphate buffer (pH 7.0, 10mM), phosphate buffer (pH 8.0, 10mM), borate buffer (pH 9.0, 10mM), borate buffer (pH 10.0, 10mM), NaOH solution (pH 11.0), NaOH solution (pH 12.0), NaOH solution (pH 13.0) and effects of pH on the GOx activity, Benzoquinone= 0.025% , Glucose= 0.5 M , Gox = 0.00375mg/ml , T= 1min; c) Kinetic curves of different luminol chemiluminescence systems: MOF/GOx /luminol/glucose, MOF/GOx/luminol, MOF/luminol/glucose, GOx /luminol/glucose. Assay conditions: Glucose=1mM, Luminol= 0.032mM, MOF= 25μg /ml in borate buffer (pH 10.0, 10mM).*

Exosome detection in biological samples. Next, we employed the Fe/Co-TPY- MIL-88(NH_2) to detect exosomes in biological samples. Since CD63 is a specific tetraspanin marker displayed on exosome surface, we labeled the Fe/Co-TPY- MIL-88(NH_2) with the anti-CD63 aptamer for exosome capture, using glutaraldehyde as the crosslinker. Glutaraldehyde firstly reacted with the $–NH_2$ groups on the surface of the Fe/Co-TPY-MIL-88(NH_2) and then linked with the NH_2-modified aptamer. Then MOF surface was modified with NH_2-modified polyethylene glycol (PEG-NH_2) through a reaction with glutaraldehyde. The residual reactive glutaraldehyde was quenched by 0.1 M glycine. (Figure S4.12). Fe/Co-TPY- MIL-88(NH_2)/ Aptamer /PEG -NH_2 bioconjugates were then applied for exosome capturing. Then the biotinylated anti-CD9 was employed to bind to another specific tetraspanin marker for exosome, CD9, on exosome surface. We used streptavidin to bridge the biotinylated GOx on the MOF and the biotinylated anti-CD9 on the exosome. In this way, the detection antibody or GOx was conjugated with the small biotin tag that imposes negligible impedance to their biological activities. In addition, we expect the multiple layers of the biotin-streptavidin assembly may help immobilize more GOx on each MOF surface through the attachment of exosomes, which could be at limited amounts in biological samples. Lastly, luminol, glucose was added for CL signal generation (Figure 4.3a).

To ensure high exosome capture efficacy and sufficient enzyme activity for signal generation, Apt: MOF ratio and MOF: EV were optimized. In addition, to reduce nonspecific binding, passivation agent concentration was optimized. The detection strategy was optimized by detecting 4×10^6 P/mL standard exosome spiking in 1XPBS. Apt: MOF

ratio, passivation agent, and MOF: EV were optimized. As shown in Figure S13 b, 76396 aptamer molecules on each MOF particle gave the best signal-to-noise ratio (S/N). Furtherer increasing aptamer molecules on MOF could hinder the peroxidase-like activity of MOF, thus reducing the S/N. Increasing the concentration of passivation agent PEG-NH_2 from 4 mM to 32 mM improved the S/N by 3.8 times. (Figure S4.12b) More PEG-NH_2 conjugated on MOF could reduce the non-specific adsorption of biotin GOx on MOF surface, thus reducing the background signal. As shown in Figure S13 d, a higher MOF: EV ratio could achieve higher S/N. As the ratio increased from 500:1 to 2000:1, the S/N improved 1.63 times. 1000: 1 (3mg MOF) was chosen for the following study. Since the S/N between 500:1 to 2000:1 was not so significant.

Next, exosome capturing efficiency was investigated. 1.6×10^8 exosome particles were spiked in 200 μL 1×PBS. 3mg aptamer-MOF or aptamer-Beads(1μm) was added to capture exosomes. After 3 hours of incubation, nanoparticles were centrifuged. And the exosome numbers in the supernatant were measured by our assay. 1.26×10^5 exosome particles were left in supernatant after MOF enrichment and the recovery rate for CD63-specific exosome was 99.92%. 2.45×10^5 particles were left in the supernatant after beads enrichment, and the recovery rate for CD63 specific exosome was 99.85%. The recovery rates for both materials were high, and the difference between the two materials was not significant because excess nanomaterial was needed for signal generation. In our previous study, we found that when EV concentrations are high, the signal dropped due to depositions of Fe/Co-MIL-88(NH_2) structure in serum. Because some complex components or extracellular vesicle in serum could attack the MOF structure. Here the stability of MOF

during EV enrichment was studied by testing the metal ions in supernatant after incubation During the 3-hr incubation, negligible Fe/Co-TPY- MIL-88(NH_2) MOF was decomposed, as confirmed by ICP-OES measurement of the released ions in the supernatant (Table S4.1). In contrast, more than 1.93 % Co and 1.68% Fe of the MOF without TPY decomposed in serum under the same incubation condition, again showing the benefit of using TPY to saturate the open metal site and increase MOF stability.

Using the standard exosomes purchased from a commercial supplier and 3.0 mg MOF, we confirmed that the cascade enzymatic reaction using GOx and peroxidase-mimicking MOF can detect exosomes dispersed in 1× PBS at concentrations ranging from 5×10^5 - 2×10^7 particles/mL (P/mL) (Figure 4.4c). The limit of detection (LOD) was calculated to be 10 P/mL with the 3σ method, which is lower than that obtained by NTA (10^8–10^9 P/mL), the HRP-based ELISA (between $10^6 \sim 10^8$ P/mL).[30, 31] In addition, the detection range was about one order of magnitude wider than that (1.6×10^5 - 1.6×10^6 P/mL) obtained with the Fe/Co-MIL-88(NH_2) MOF in our previous study. The calculated limit of detection is quite low by the 3-sigma (3σ) method. There might by false negatives due to only a limited amount of variability is incorporated into the calculation. Thus, the analytical sensitivity which can be visualized by the slope of the calibration curve was applied to evaluated the sensitivity of the platform in this study at the same time.[32-34] Analytical sensitivity of current platform was compared with Fe/Co-MIL-88(NH_2) MOF based platform in previous study. (Figure S4.13) The slope of current platform is about 2.3 times steeper than the platform obtained with the Fe/Co-MIL-88(NH_2) MOF proving the superior sensitivity of current platform.

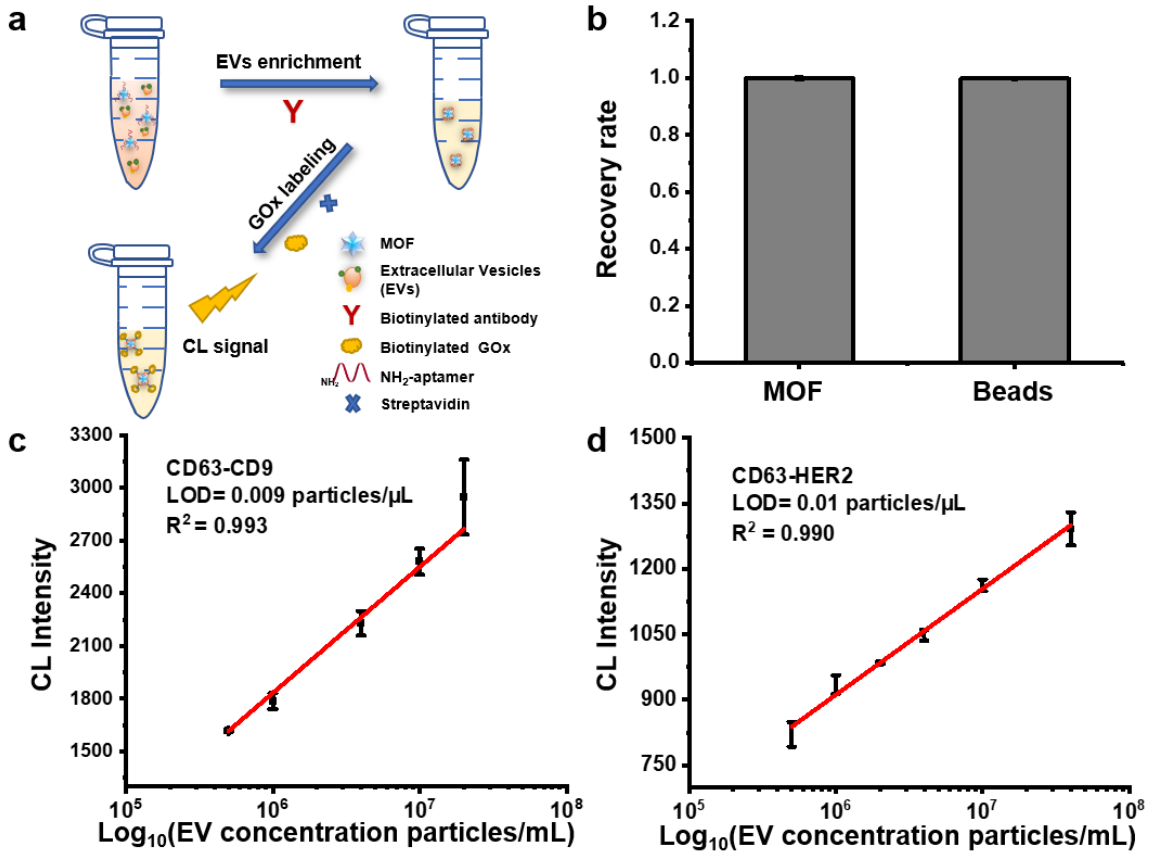

Figure 4.4 *a) Scheme of EV detection facilitated by the cascade reaction between the peroxidase-mimicking Fe/Co-TPY-MIL-88(NH_2) and GOx, b) Recovery rate of MOF enrichment Vs. Beads enrichment, c) Calibration curve of the assay for detection EVs dispersed in 1× PBS with CD63-CD9 method, d) Calibration curve of the assay for detection EVs dispersed in 1× PBS with CD63-HER2 method.*

Exosome detection in serum samples. With the superior detection performance demonstrated for the bimetallic MOF, we applied the CD63-CD9 assay to detect exosomes in human serum collected from breast cancer patients and healthy people (n = 8 for each cohort). We found that the exosome concentrations in these clinical samples were much higher than the upper detection limit of our assay, and 2,000× dilution was needed for all samples, which means that we only needed far less than 1 μL serum for each measurement. The exosome concentrations were found to be significantly higher ($p < 0.05$) in patients' sera samples (**Figure 4.5a**) than that found in the samples of healthy controls. The CD63-

HER2 assay was applied to detect exosomes in the same human serum collected from breast cancer patients and healthy people (n = 8 for each cohort). And we found that CD63-HER2 exosome subpopulation concentrations were significantly higher ($p < 0.05$) in patients' sera samples (**Figure 4.5b**). In addition, such difference ($p = 0.0087$) was more significant than the one resulted from CD63-CD9 exosome subpopulation ($p = 0.013$). The Fe/Co-TPY-MIL-88(NH_2) can enable sensitive exosome detection in complex biological matrices with ultra-low sample consumption, proving its high potential in clinical applications.

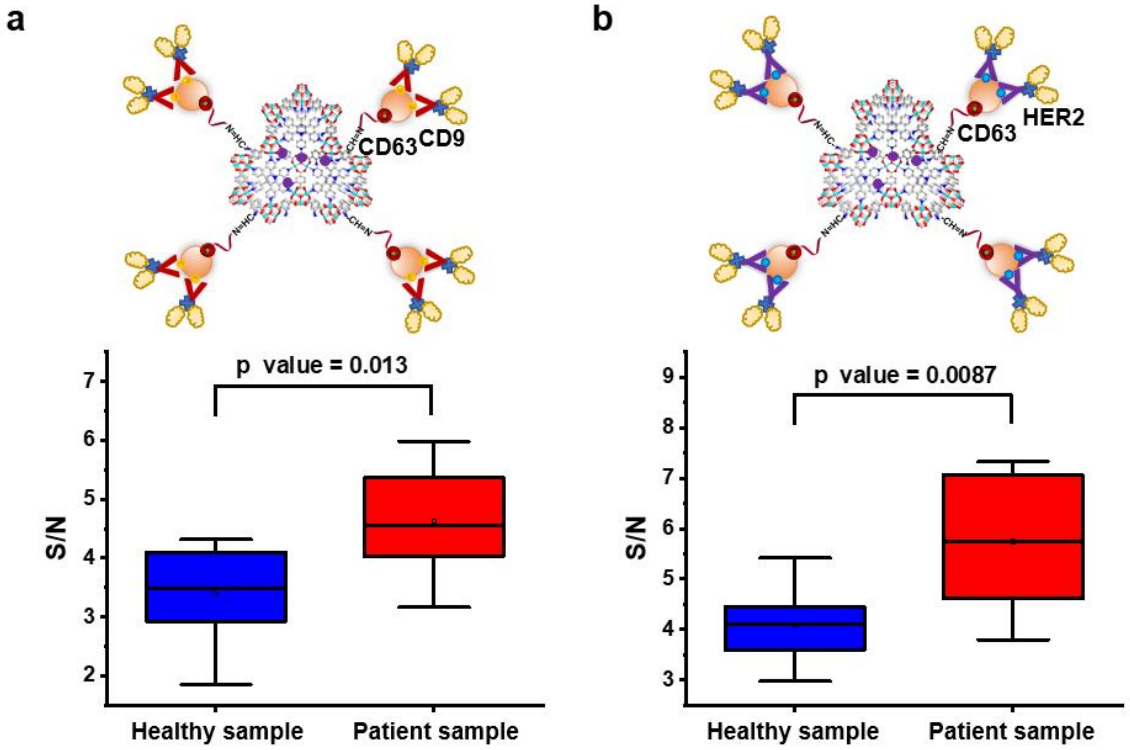

Figure 4.5 *Application of Fe/Co-TPY-MIL-88(NH_2) for EV detection in the sera samples from healthy controls (n=8) and breast cancer patients (n=8). a) CD63-CD9 method, b) CD63-HER2 method. The detection solution contained glucose=1mM, luminol= 0.032mM in borate buffer (pH 10.0, 10mM).*

4.4 Conclusion

In present work Fe/Co-TPY-MIL-88(NH_2) MOF with pore partition agent, 2,4,6-tri(4-pyridinyl) -1- pyridine (TPY), is developed. In comparison with Fe/Co-MIL-88(NH_2), Fe/Co-TPY-MIL-88(NH_2) shows high peroxidase-like activity and superior stability in aqueous solutions. What's more, it can act as the peroxidase-mimic and work together with glucose oxidase (GOx) in the cascade enzymatic reactions to generate chemiluminescence by inputting glucose. Comparing with colorimetric system, MOF/chemiluminescence system realized lower background due to no oxidized activity of MOF to luminol. As, a result, this reaction system can be used for sensitive exosome detection in biological samples and acquire the detection limit three orders of magnitude lower than that obtained with Fe/Co-MIL-88(NH_2), In addition, improved stability of MOF wider the detection range for exosome detection.

Supporting Information

Supporting figures

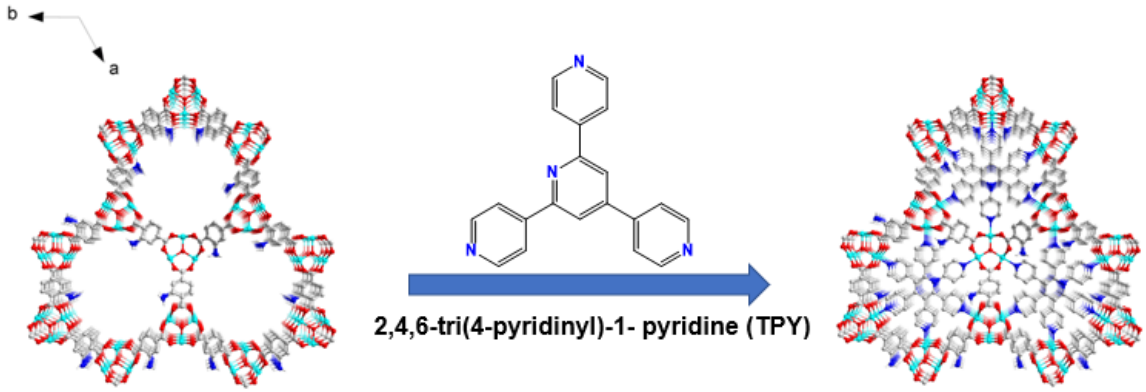

Figure S4.1 *Illustration of pore space partition through symmetry matching regulated ligand insertion. viewed along c axis.*

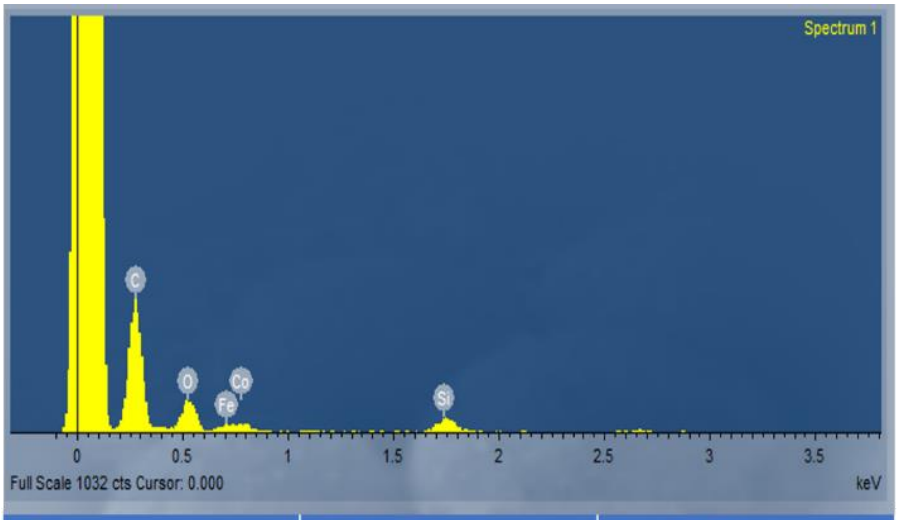

Element	Weight %	Atomics%
Fe	6.55 +/- 3.01	1.65
Co	5.69 +/- 1.79	1.36

Figure S4.2 *EDS scanning spectra of activated Fe/Co-TPY-MIL-88(NH2)*

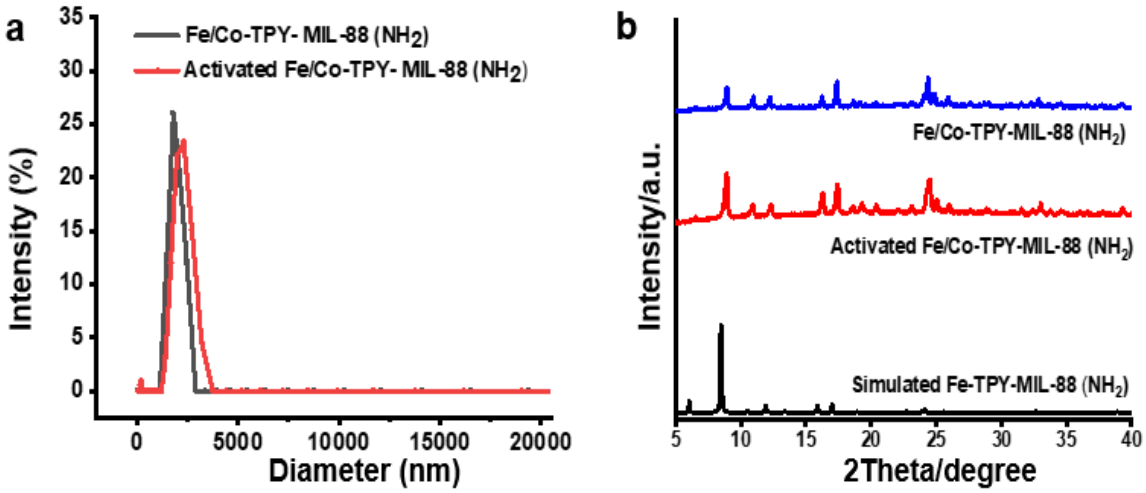

Figure S4.3 *a) Dynamic Light Scattering of and; b) Powder X-ray diffraction patterns for Fe/Co-TPY- MIL-88(NH_2) before and after activation.*

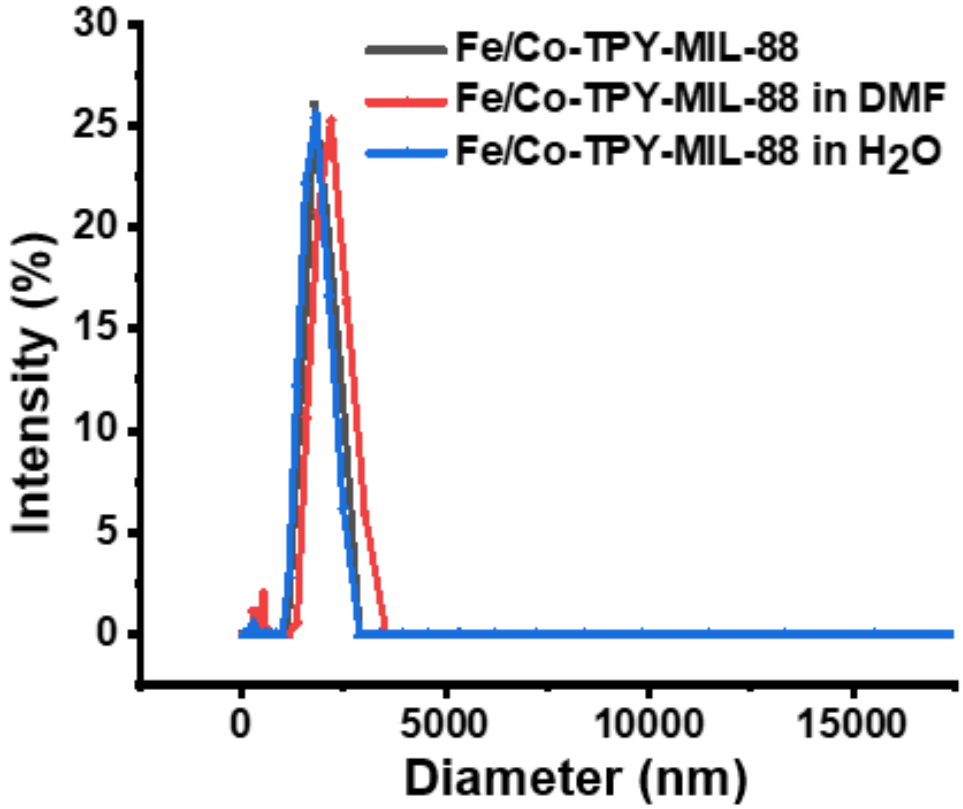

Figure S4.4 *Dynamic Light Scattering results of Fe/Co-TPY-MIL-88(NH_2) before and after stored at room temperature for 1 week.*

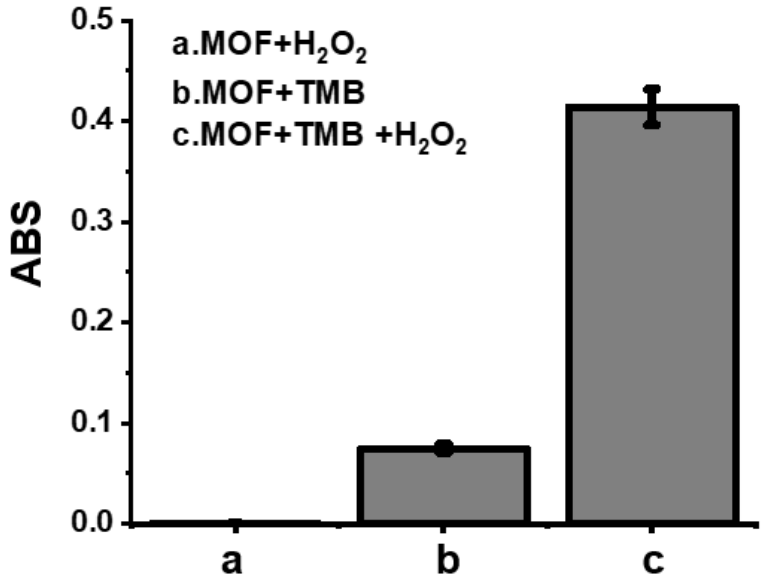

Figure S4.5 *Absorption of the 200-µL mixture of 1.0 mM TMB and 1.0 mM H_2O_2 with 50 ug/ml MOF, and the two control reactions of mixing the MOF with TMB or H_2O_2 only. All reactions measured at 15 min.*

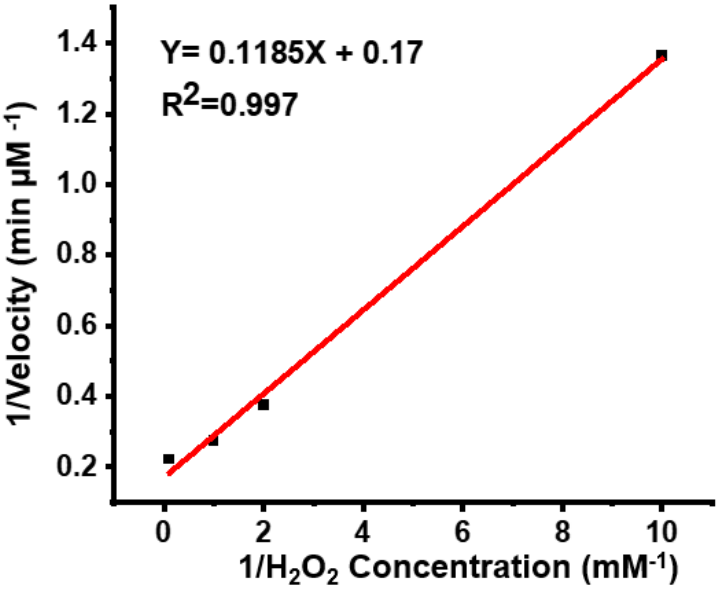

Figure S4.6 *The double reciprocal of Michaelis–Menten fitting curve plotting the initial velocities within the first 15 min against H_2O_2 concentrations, TMB =1 mM, Fe/Co-TPY-MIL-88(NH_2) = 50 μg/ml in 200 mM NaAc-HAc buffer at pH 4.1.*

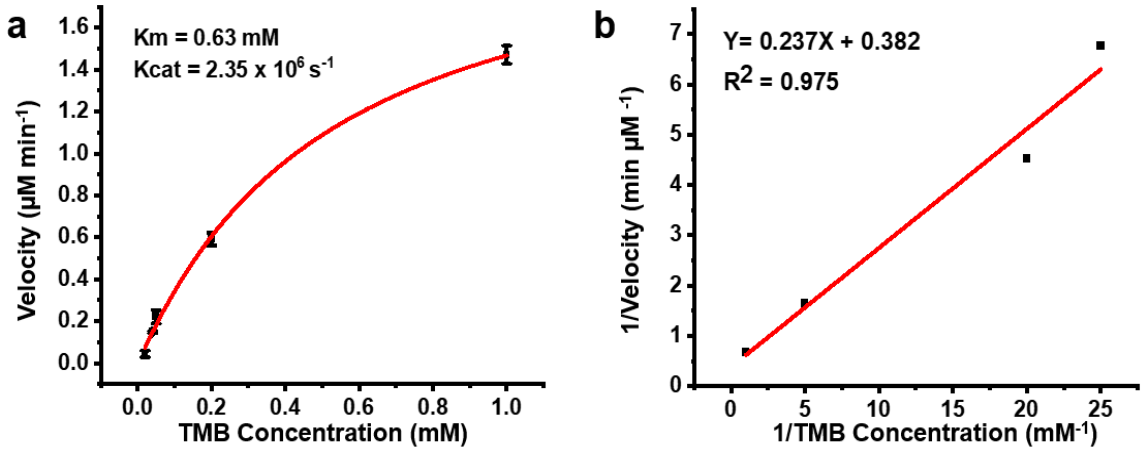

Figure S4.7 *Steady-state kinetics study of Fe/Co-TPY-MIL-88(NH_2). a) The Michaelis–Menten curve that plots the initial •OH generation velocities within the first 15 min against TMB concentrations. b) The double reciprocal of Michaelis–Menten fitting curve using data shown in a), H_2O_2 =0.2 mM, Fe/Co-TPY-MIL-88(NH_2) = 50 μg/ml in 200 mM NaAc-HAc buffer at pH 4.1.*

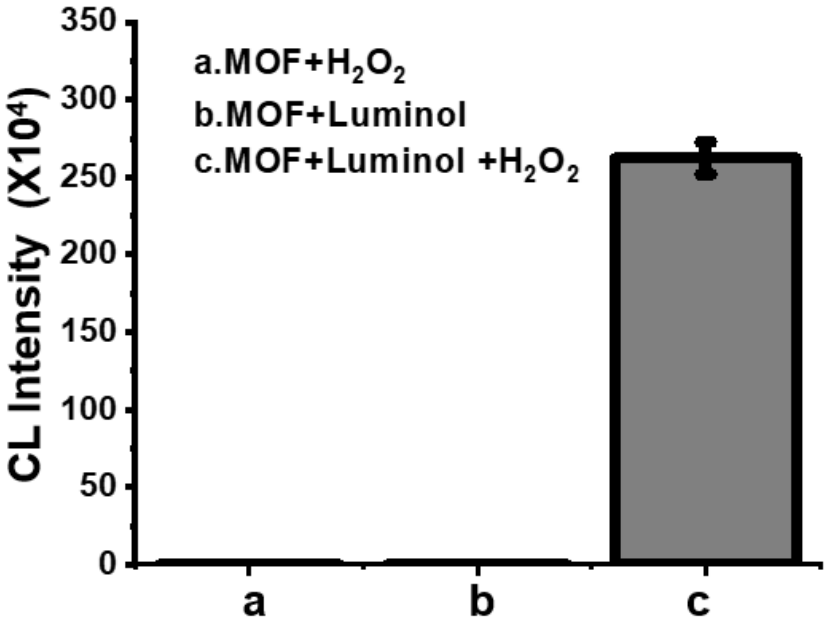

Figure S4.8 *Chemiluminescence of the 100-µL mixture of H_2O_2 =1mM, Luminol= 0.002mM, MOF= 50µg /ml in borate buffer (pH 10.0, 10mM) and the two control reactions of mixing the MOF with TMB or H_2O_2 only.*

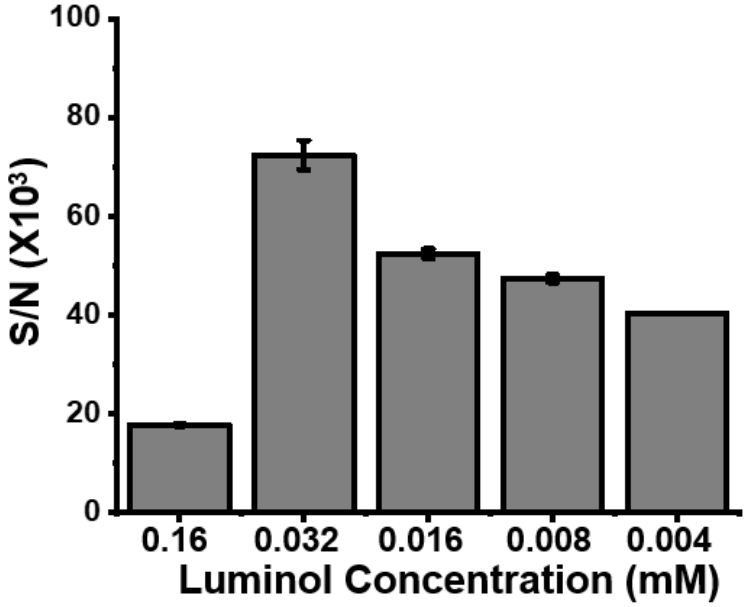

Figure S4.9 *Effects of the luminol concentrations on the luminol/H_2O_2/MOF chemiluminescence system,1 mM H_2O_2, 50 μg/mL MOF in borate buffer (pH 10.0, 10mM).*

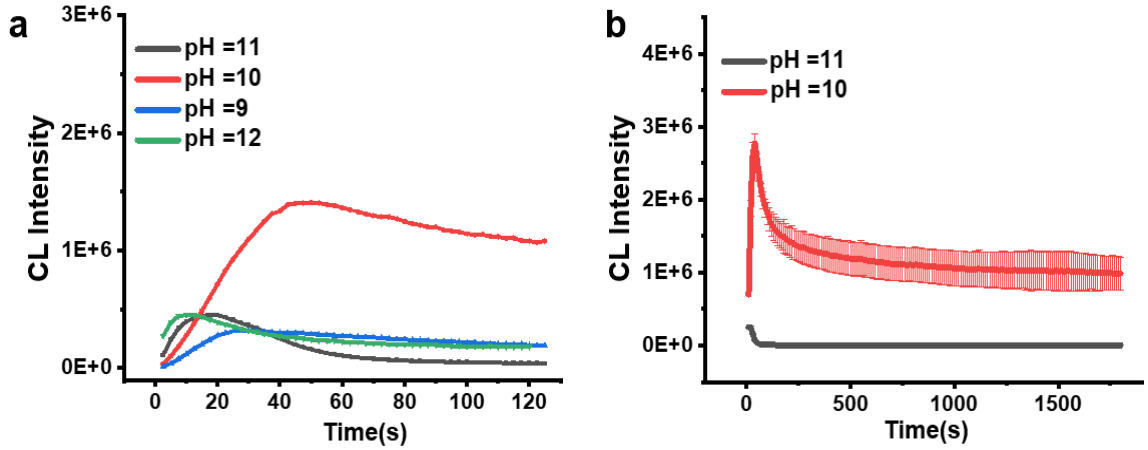

Figure S4.10 *Kinetic curves of MOF/GOx/luminol/glucose chemiluminescence systems at different pH, glucose=1mM, Luminol= 0.032mM, MOF= 50µg /ml in borate buffer (pH 10.0, 10mM) a) within 120 seconds; b) within 1800 seconds.*

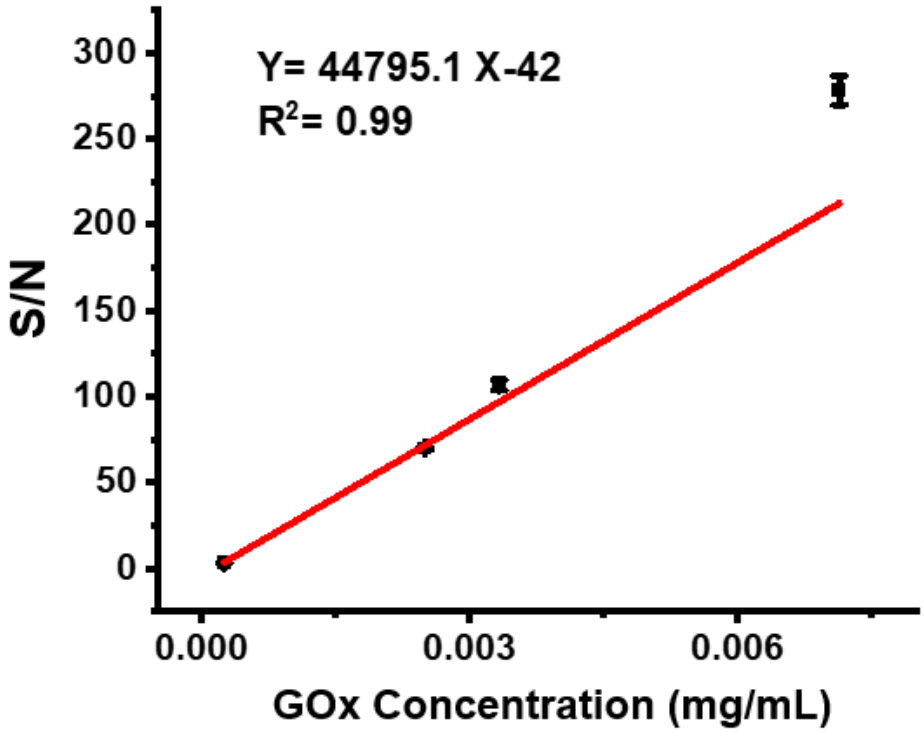

Figure S4.11 *GOx determination based on the MOF/GOx/luminol/glucose CL system. Detection conditions: Glucose=1mM, Luminol= 0.032mM, MOF= 25µg /ml, GOx=0.25mg /mL-0.25µg /mL in borate buffer (pH 10.0, 10mM).*

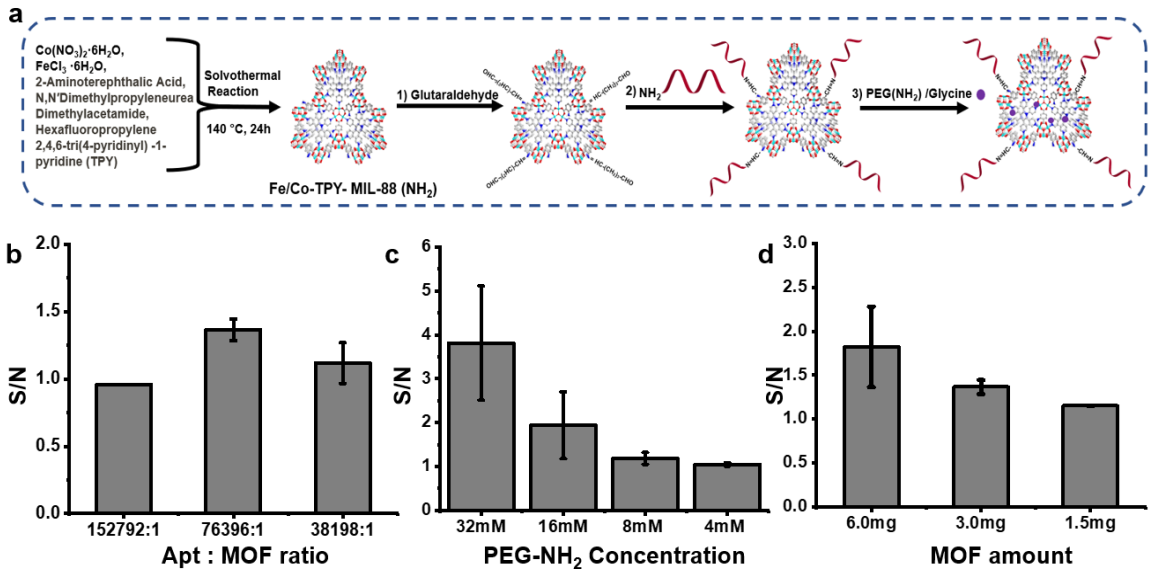

Figure S4.12 *a) Diagram of preparation of Fe/Co-TPY-MIL88(NH2)/ CD63/ PEG (NH2) bioconjugates, Optimization of conjugation conditions; b) Apt:MOF ratio; c) PEG-NH2 concentration; d) optimization of MOF amount for EV detection.*

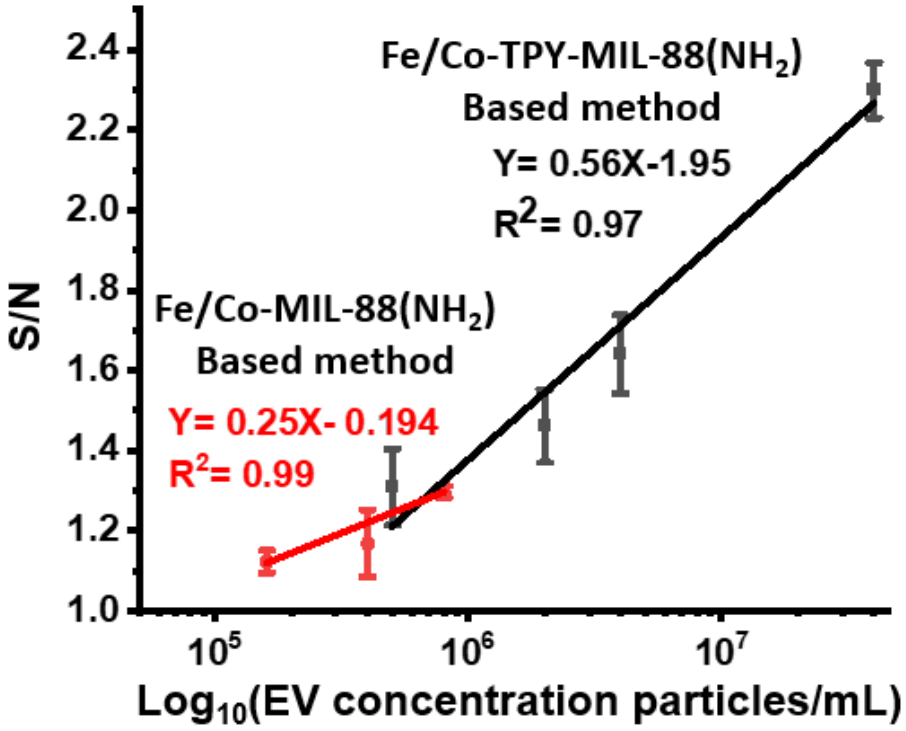

Figure S4.13 *Comparison of TPY MOF based platform and non-TPY MOF based platform.*

Supporting table

Treatment	Cobalt (% releasing)	Iron (% releasing)
Incubate TPY MOF with serum	0.51	0.09
Incubate non-TPY MOF with serum	1.93	1.68

Table S4.1 *ICP-OES of ion releasing after treat MOF with different conditions.*

Reference

1. Kucherenko, I., Soldatkin, O., Dzyadevych, S. & Soldatkin, A.J.A.c.a. Electrochemical biosensors based on multienzyme systems: main groups, advantages and limitations–a review. **1111**, 114-131 (2020).

2. Cai, X. et al. Nanozyme-involved biomimetic cascade catalysis for biomedical applications. *Materials Today* **44**, 211-228 (2021).

3. Vázquez-González, M., Wang, C. & Willner, I. Biocatalytic cascades operating on macromolecular scaffolds and in confined environments. *Nature Catalysis* **3**, 256-273 (2020).

4. Liu, Y., Zheng, Y., Chen, Z., Qin, Y. & Guo, R. High-Performance Integrated Enzyme Cascade Bioplatform Based on Protein–BiPt Nanochain@ Graphene Oxide Hybrid Guided One-Pot Self-Assembly Strategy. *Small* **15**, 1804987 (2019).

5. Sengupta, P., Pramanik, K., Datta, P. & Sarkar, P. Chemically modified carbon nitride-chitin-acetic acid hybrid as a metal-free bifunctional nanozyme cascade of glucose oxidase-peroxidase for "click off" colorimetric detection of peroxide and glucose. *Biosensors and Bioelectronics* **154**, 112072 (2020).

6. Jiao, L. et al. A dopamine-induced Au hydrogel nanozyme for enhanced biomimetic catalysis. *Chemical Communications* **55**, 9865-9868 (2019).

7. Wu, Y. et al. Cascade reaction system integrating single-atom nanozymes with abundant Cu sites for enhanced biosensing. *Analytical chemistry* **92**, 3373-3379 (2020).

8. Xianyu, Y., Chen, Y. & Jiang, X. Horseradish peroxidase-mediated, iodide-catalyzed cascade reaction for plasmonic immunoassays. *Analytical chemistry* **87**, 10688-10692 (2015).

9. Xu, W. et al. Metal–organic frameworks enhance biomimetic cascade catalysis for biosensing. *Advanced Materials* **33**, 2005172 (2021).

10. Liang, J. & Liang, K. Multi-enzyme Cascade Reactions in Metal-organic Frameworks. *The Chemical Record* **20**, 1100-1116 (2020).

11. Feng, Y. et al. Recent advances in enzyme immobilization based on novel porous framework materials and its applications in biosensing. *Coordination Chemistry Reviews* **459**, 214414 (2022).

12. Peng, S. et al. Efficient Separation of Nucleic Acids with Different Secondary Structures by Metal–Organic Frameworks. **142**, 5049-5059 (2020).
13. Yang, S.-S. et al. Enrichment of phosphorylated peptides with metal–organic framework nanosheets for serum profiling of diabetes and phosphoproteomics analysis. **90**, 13796-13805 (2018).

14. Zhang, L. et al. Anti-Tim4 Grafting Strongly Hydrophilic Metal–Organic Frameworks Immunoaffinity Flake for High-Efficiency Capture and Separation of Exosomes. **93**, 6534-6543 (2021).

15. Zhang, C. et al. Design and application of hydrophilic bimetallic metal-organic framework magnetic nanoparticles for rapid capture of exosomes. **1186**, 339099 (2021).

16. Zhao, X., Bu, X., Zhai, Q.-G., Tran, H. & Feng, P. Pore space partition by symmetry-matching regulated ligand insertion and dramatic tuning on carbon dioxide uptake. *Journal of the American Chemical Society* **137**, 1396-1399 (2015).

17. Yang, H. et al. Pore-space-partition-enabled exceptional ethane uptake and ethane-selective ethane–ethylene separation. *Journal of the American Chemical Society* **142**, 2222-2227 (2020).

18. Jiang, B. et al. Standardized assays for determining the catalytic activity and kinetics of peroxidase-like nanozymes. **13**, 1506-1520 (2018).

19. Fan, W. et al. Expanded Porous Metal–Organic Frameworks by SCSC: Organic Building Units Modifying and Enhanced Gas-Adsorption Properties. *Inorganic Chemistry* **55**, 6420-6425 (2016).

20. Zhang, X., Frey, B.L., Chen, Y.-S. & Zhang, J. Topology-guided stepwise insertion of three secondary linkers in zirconium metal–organic frameworks. *Journal of the American Chemical Society* **140**, 7710-7715 (2018).

21. Fan, W., Zhang, X., Kang, Z., Liu, X. & Sun, D. Isoreticular chemistry within metal–organic frameworks for gas storage and separation. *Coordination Chemistry Reviews* **443**, 213968 (2021).

22. Zhao, X., Bu, X., Zhai, Q.-G., Tran, H. & Feng, P.J.J.o.t.A.C.S. Pore space partition by symmetry-matching regulated ligand insertion and dramatic tuning on carbon dioxide uptake. **137**, 1396-1399 (2015).

23. Yang, H. et al. A bimetallic (Co/2Fe) metal-organic framework with oxidase and peroxidase mimicking activity for colorimetric detection of hydrogen peroxide. **184**, 4629-4635 (2017).

24. Xiao, Z. et al. An Integrated Chemiluminescence Microreactor for Ultrastrong and Long-Lasting Light Emission. **7**, 2000065 (2020).
25. Moldovan, Z., Popa, D.E., David, I.G., Buleandra, M. & Badea, I.A.J.J.o.S. A derivative spectrometric method for hydroquinone determination in the presence of kojic acid, glycolic acid, and ascorbic acid. **2017** (2017).

26. Ciucu, A. & Patroescu, C.J.A.l. Fast spectrometric method of determining the activity of glucose oxidase. **17**, 1417-1427 (1984).

27. Yuan, S., Qin, J.-S., Lollar, C.T. & Zhou, H.-C. Stable metal–organic frameworks with group 4 metals: current status and trends. *ACS central science* **4**, 440-450 (2018).

28. Sun, X., Lei, J., Jin, Y. & Li, B. Long-lasting and intense chemiluminescence of luminol triggered by oxidized g-C3N4 nanosheets. *Analytical Chemistry* **92**, 11860-11868 (2020).
29. Chen, X. et al. Long-Lasting Chemiluminescence-Based POCT for Portable and Visual Pathogenic Detection and In Situ Inactivation. *Analytical Chemistry* (2022).

30. Doldán, X., Fagúndez, P., Cayota, A., Laíz, J. & Tosar, J.P.J.A.c. Electrochemical sandwich immunosensor for determination of exosomes based on surface marker-mediated signal amplification. **88**, 10466-10473 (2016).

31. Zarovni, N. et al. Integrated isolation and quantitative analysis of exosome shuttled proteins and nucleic acids using immunocapture approaches. **87**, 46-58 (2015).

32. Currie, L. CAS: 528: DyaK1MXjsFKnt7s% 3D: Nomenclature in evaluation of analytical methods including detection and quantification capabilities:(IUPAC recommendations 1995). vol. 391, issue 2. *Anal Chim Acta*, 105-126 (1999).

33. Clinical & Institute, L.S. (Wayne PA, 2004).

34. Borysiak, M.D., Thompson, M.J. & Posner, J.D. Translating diagnostic assays from the laboratory to the clinic: analytical and clinical metrics for device development and evaluation. *Lab on a Chip* **16**, 1293-1313 (2016).

Chapter V. Conclusion and Implications

5.1 Conclusion

Extracellular vesicles (EVs) have been considered promising biomarkers for disease diagnosis. An increasing number of studies have proved the superiority of EVs as a disease biomarker for better specificity and selectivity.[1-4] Although current methods for EVs analysis are effective and robust, they still have numerous tradeoffs and drawbacks. The main obstacles to EV analysis are requiring labor-intensive EV extraction steps and limited detection sensitivity of the methods. Additionally, laboratory diagnostic methods are complex, require a dedicated laboratory, high technical skills, costly equipment, and are time-consuming. Unfortunately, these requirements make these methods impractical for diagnostics use. Thus, simple but sensitive techniques for rapid EV detection are in demand to speed up the discovery and clinical applications of EV-based disease markers. Overall, this dissertation developed rapid and sensitive methods for EV detection and tested the feasibility of these methods for breast cancer diagnosis. Novel porous nanomaterial containing numerous transition metal ions was developed for efficient EVs enrichment and detection signal amplification.

In chapter 2, a CuS Microgel and filter membrane-based method was developed for rapid and sensitive detection of EVs. The assay was applied to directly and highly efficiently quantify EVs in serum or cell culture medium. The advantages of the assay include 1. The assay offers high sensitivity. As low as 10^4 particles/mL EVs were detected with our method targeting two different EV surface proteins. 2. Through the filtration process, our method can accurately quantify EVs by removing influence from

contaminants and matrix components. 3. The assay is simple, fast, and practical. The assay only requires simple filtration and 2 minutes low-speed centrifugation. The only drawback of the method is the difficulty of collecting antibody conjugated microgel.

Chapter 3 developed a bimetallic Fe/Co-MIL-88(NH2) with superior peroxidase catalytic activities and good stability for EV detection. Because of the abundant active site and synergistic effect between Fe and Co, the Fe/Co-MIL-88(NH2) exhibits superior catalytic activity to HRP and the monometallic Fe-MIL-88(NH2). It can also enable sensitive EVs detection while forming a cascade reaction with GOx, demonstrating great potential to be signaling labels in bioassays for the detection of biomarkers. The Fe/Co-MIL-88(NH2) was also used as a labeling tag for sandwich Elisa-based assay for EVs detection. The Fe/Co-MIL-88(NH2) based cascade reaction detection platform in this chapter has advantages and disadvantages. The benefits include: The platform's sensitivity was great and could be seen by the naked eye. Also, only 1μl serum was needed for cancer diagnosis. Some improvements are still required to proceed with clinical applications of this peroxidase-like MOF material. For example, the dynamic range is relatively narrow in the current format. First, the intrinsic oxidase activity towards TMB of the bimetallic MOF produces a high background at low target concentrations. On the other hand, the decomposition of MOF structure prevents further signal increase at high EVs concentration. Different signaling strategies and MOF designs could be adopted to improve the detection range in future studies.

In chapter 4, the cascade reaction platform for EV detection was improved by developing Fe/Co-TPY-MIL-88(NH_2) MOF, which showed high peroxidase-like activity

and superior stability in aqueous solutions. The peroxidase-mimic work with glucose oxidase (GOx) in the cascade enzymatic reactions to generate chemiluminescence. The reaction system can be used for sensitive exosome detection in biological samples and acquire the detection limit three orders of magnitude lower than that obtained with Fe/Co-MIL-88(NH_2).

In summary, three different methods were developed for EV detections including a CuS microgel and filter membrane-based strategy, a bimetallic Metal–Organic Framework (MOF) based method, and a TPY Metal–Organic Framework (MOF) based method. (Table S5.1) The CuS microgel and filter membrane-based strategy is the most sensitive one. The detection range is 10 - 10^5 particles/μL. And the limit of detection is 0.827particles/ μL. In addition, the filter membrane-based strategy is fastest one. Since the EV extraction is enabled by simple filtration. Its' main disadvantages are requirement of acid digestion and the hardness of collecting modified CuS Microgel. The detection range of the bimetallic Metal–Organic Framework (MOF) based method is 160 – 1600 particles/μL. And the limit of detection is 78 particles/ μL. The sensitivity of this method was great. Also, the detection is visible by eyes. However, the drawbacks of this method are narrow detection range and long signal generation time. The TPY MOF based method was designed to overcome those drawbacks. The detection range is 2×10^4 - 2×10^5 particles/μL and the LOD is 10 particles/μL. The sensitivity was great. The detection range was improved at the same time. Those methods were rapid by saving the time-consuming EVs extraction steps. Each of the methods was simple, inexpensive and suitable for use by minimally-trained personnel in the field, laboratory, or point-of-care location. These methods showed great sensitivity.

The detection limit is between 10 ~ 827 particles/μL, which is lower than Elisa and NTA (10^4 Particles/μL), which are gold standard methods.

Method	Detection range (particles/μL)	LOD (particles/ μL)	Advantage	Disadvantage
A CuS Microgel and Filter Membrane Based Strategy for Extracellular vesicles detection	$10\text{-}10^5$	0.827	• Rapid • Excellent sensitivity • Wide detection range	• Require acid digestion • Hard to recovery modified CuS Microgel
Application of Metal–Organic Framework (MOF) in Detection of Extracellular Vesicles	1.6×10^2 - 1.6×10^3	78	• Good sensitivity • Visible detection	• Narrow detection range • Need 45 minutes for signal generation
Improvement the detection performance of MOF-based method for sensing Extracellular Vesicle	5×10^2 -4 $\times10^4$	0.01	• Good sensitivity • Wide detection range	• High background
ELISA	2×10^4 -2×10^5	10^4	• Robust • Widely used	• Limited sensitivity • Time-consuming

Table 5.1 *Summary of the detection methods in this dissertation and Elisa.*

5.2 Future Outlook

Each method presented in this work offers a fast, sensitive, and affordable way to detect EVs. But there are some potential ways to improve the current detection platform. Firstly, some other enzyme-mimicking nanomaterial to mediating size exclusion detection. In addition, the size exclusion detection method could be integrated with other filter membrane equipment.

The platform in chapter 4 could be further improved by applying other MOF designs. Although the sensitivity of the detection platform was great, it still requires 3mg per reaction to generate the signal. And the MOF to EV particle ratio was 1000:1, meaning excess MOF particles were used to ensure the activity to create the signal. To solve this PROBLEM, other MOF designs with improved peroxidase mimicking could be applied. For example, Pacs MOF with the other metal ions and ligands can potentially try.[5] The methods in chapters 3 and 4 need centrifugation to enrich EVs. We can design magnetic field-responsive MOF by tuning the MOF components. For example, some studies proved that MOF with Mn^{2+} trimer could respond to the magnetic field.[6]

Reference

1. Hinestrosa, J.P. et al. Early-stage multi-cancer detection using an extracellular vesicle protein-based blood test. *Communications medicine* **2**, 1-9 (2022).

2. Yu, Z.L. et al. Untouched isolation enables targeted functional analysis of tumour-cell-derived extracellular vesicles from tumour tissues. *Journal of extracellular vesicles* **11**, e12214 (2022).

3. Liu, C. et al. Low-cost thermophoretic profiling of extracellular-vesicle surface proteins for the early detection and classification of cancers. *Nature biomedical engineering* **3**, 183-193 (2019).

4. Wei, P. et al. Plasma extracellular vesicles detected by single molecule array technology as a liquid biopsy for colorectal cancer. *Journal of extracellular vesicles* **9**, 1809765 (2020).

5. Zhao, X. et al. Multivariable modular design of pore space partition. *Journal of the American Chemical Society* **138**, 15102-15105 (2016).

6. Akbar, M.U., Badar, M. & Zaheer, M. Programmable Drug Release from a Dual-Stimuli Responsive Magnetic Metal–Organic Framework. *ACS omega* (2022).